Combination of the H1 and ZEUS inclusive cross-section measurements at proton beam energies of 460 GeV and 575 GeV and tests of low Bjorken-x phenomenological models

Dissertation
zur Erlangung des Doktorgrades
des Department Physik
der Universität Hamburg

vorgelegt von

Pavel Belov
aus Leningrad / Sankt Petersburg

Hamburg
2013

Gutachter der Dissertation:	Dr. Alexandre Glazov PD Dr. Thomas Schörner-Sadenius
Gutachter der Disputation:	Dr. Alexandre Glazov Prof. Dr. Peter Schleper
Datum der Disputation:	31. Mai 2013
Vorsitzender des Prüfungsausschusses:	Prof. Dr. Dieter Horns
Vorsitzender des Promotionsausschusses:	Prof. Dr. Peter Hauschildt
Dekan der MIN Fakultät:	Prof. Dr. Heinrich Graener

Abstract

A combination is presented of the inclusive neutral current $e^{\pm}p$ scattering cross section data collected by the H1 and ZEUS collaborations during the last months of the HERA II operation period with proton beam energies E_p of 460 and 575 GeV. The kinematic range of the cross section data covers low absolute four-momentum transfers squared, $1.5\ \mathrm{GeV}^2 \leq Q^2 \leq 110\ \mathrm{GeV}^2$, small values of Bjorken-x, $2.8 \cdot 10^{-5} \leq x \leq 1.5 \cdot 10^{-2}$, and high inelasticity $y \leq 0.85$. The combination algorithm is based on the method of least squares and takes into account correlations of the systematic uncertainties. The combined data are used in the QCD fits to extract the parton distribution functions. The phenomenological low-x dipole models are tested and parameters of the models are obtained. A good description of the data by the dipole model taking into account the evolution of the gluon distribution is observed. The longitudinal structure function F_L is extracted from the combination of the currently used H1 and ZEUS reduced proton beam energy data with previously published H1 nominal proton beam energy data of 920 GeV. A precision of the obtained values of F_L is improved at medium Q^2 compared to the published results of the H1 collaboration.

Kurzfassung

Es wird eine Kombination der Messungen des inklusiven Wirkungsquerschnitts für $e^{\pm}p$ Streuung mit neutralem Strom der H1 und ZEUS Kollaborationen, basierend auf Daten in den letzten Monaten der HERA II Messperiode mit Protonstrahlenergie E_p von 460 beziehungsweise 575 GeV, präsentiert. Der kinematische Bereich der Messungen ist gegeben durch einen kleinen quadratischen Betrag des Vierimpulsübertrags Q^2, $1,5\ \text{GeV}^2 \leq Q^2 \leq 110\ \text{GeV}^2$, kleinen Werten von Bjorken-x, $2,8 \cdot 10^{-5} \leq x \leq 1,5 \cdot 10^{-2}$ und einer hohen Inelasitzität y von $y \leq 0,85$. Der Kombinationsalgorithmus basiert auf der Methode der kleinsten Quadrate und berücksichtigt die Korrelationen der systematischen Fehler. Die kombinierten Daten werden für QCD-Fits benutzt zur Extraktion der Parton Verteilungsfunktionen. Die phänomenologischen low-x Dipolmodelle werden getestet und daraus deren Parameter bestimmt. Eine gute Beschreibung der Daten durch das Dipolmodell unter Berücksichtigung der Evolution der Gluonverteilung wird beobachtet. Die longitudinale Strukturfunktion F_L wird extrahiert aus der Kombination der aktuellen H1 und ZEUS Daten mit reduzierter Protonstrahlenergie und der zuvor veröffentlichten H1 Daten mit nomineller Protonstrahlenergie von 920 GeV. Die Präzision der so gewonnenen Werte von F_L ist bei mittlerem Q^2 deutlich verbessert im Vergleich zu den zuvor veröffentlichten Resultaten der H1 Kollaboration.

Contents

1 Introduction

The main goal of physics is to describe the natural phenomena using a minimal number of the most general fundamental principles. Among the variety of the open problems, one of the crucially important questions of the modern physics is a question about the structure of matter and the fundamental interactions. The matter is described in terms of the elementary particles and their interactions, and in spite of a diversity of the natural phenomena, all observed interactions between these particles are reduced to four fundamental types: the strong, electromagnetic (EM), weak, and gravitational. Only three of these fundamental types of interactions are described by a general theory. It is the *Standard Model* (SM) [1] of particle physics which provides a unified picture of the strong, EM, and weak interaction. Although the gravitation is not described by the SM, for experimentally achieved energies the relative strength of gravitation interaction is more than 10^{38} times smaller than the strength of the EM interaction and its effect can be neglected. Therefore, it is possible to state that up to date the SM is the most general theory and satisfies the Albert Einstein's criteria for the simplicity of a theory: "It can scarcely be denied that the supreme goal of all theory is to make the irreducible basic elements as simple and as few as possible without having to surrender the adequate representation of a single datum of experience" [1].

According to the SM, the fundamental constituents of the matter are the elementary fermions, namely quarks and leptons, which are particles with a half-integer spin. Quarks are subject to all four types of fundamental interactions and exist only in bound states, forming the composite particles called hadrons. Although hadrons are not described by the SM, they are basic components of the surroundings and categorized into two families: baryons, which consist of three quarks (e.g. protons, neutrons) and mesons which are made of one quark and one antiquark (e.g. kaons, pions). There are six quarks grouped into three generations: up u and down d, charm c and strange s, top t and bottom b. Unlike quarks, the leptons are free particles, which are not subject to the strong interaction. They are classified into three generations as follows: the electron e and electron neutrino ν_e, the muon μ and muon neutrino ν_μ, the tau τ and tau neutrino ν_τ.

Within a framework of the SM, the interaction of fermions is described by exchange of the gauge bosons. They are the integer-spin elementary particles mediating the fundamental interactions. For each type of the fundamental interaction corresponds some kind of the gauge boson: the photon γ mediates the electromagnetic interaction; the heavy gauge bosons, Z^0, W^+, and W^-, carry the weak interaction; and the eight gluons g mediate the strong interaction. The Higgs boson [4] is also predicted by the SM as an important component of the theory, which is responsible for the acquisition of mass by elementary particles. The up to date properties of the

[1] "On the Method of Theoretical Physics" The Herbert Spencer Lecture, delivered at Oxford (10 June 1933); also published in Philosophy of Science, Vol. 1, No. 2 (April 1934), pp. 163-169.

mentioned elementary particles are summarized in Table 1.

From a theoretical point of view, the interaction between elementary particles is described by the theories with a so-called local gauge symmetry. The property of local gauge symmetry implies that the function describing the dynamics of the interacting particles is invariant under a continuous group of local transformations. The local transformation is a transformation which differs for different points of space-time, thereby depends on the coordinates. These theories are the generalization of the Quantum Electrodynamics (QED) [2] which is a U(1)-gauge theory of interaction of charged leptons. Using of the gauge group $SU(2) \otimes U(1)$ together with the spontaneous symmetry breaking made it possible to unify the electromagnetic and weak interaction. Introducing the theory of strong interaction, Quantum Chromodynamics (QCD) [3], based on the gauge symmetry group SU(3) led to creation of the SM.

During the twentieth century, the elementary particles, their interactions and properties have been the subject of a comprehensive investigation in various experiments. Although a whole ensemble of carried out experiments confirms the predictions of the SM, nowadays the intensive testing of the SM is being continued. In this context, it is worth noting the experiments at the modern proton-proton collider LHC and the recent experimental observation of the Higgs-like boson [5]. The latter has become a pivotal moment in the history of modern particle physics.

Since the famous experiments of Ernest Rutherford [6] which have revealed the structure of atom, the scattering of particles off a some target has been established as a basic type of experiment in nuclear physics. The transition from nuclear to particle physics inferred probing the internal structure of atomic nuclei and the separate nucleons and required the particles accelerated to higher energies. The fiftieth years marked the beginning of the accelerator physics era, when Robert Hofstadter with colleagues probed the structure of atomic nuclei and obtained radius and the charge density of the proton by the electron scattering [7].

A detailed study of the internal structure of the proton became possible in the experiments on the Deep Inelastic Scattering (DIS) in which the nucleon target is dissociated to large invariant mass state. The first DIS experiments on the electron-proton scattering have been carried out at SLAC [8] and revealed that the proton is a composite particle consisting of smaller particles which have been called *partons*. The electron has been and still remains a perfect candidate for investigation of the nucleons and, in particular, proton inner structure. It is a stable point-like object, lepton, and its electroweak interactions are well understood. Moreover, it can be easily produced and accelerated. The wavelength of the accelerated to high energies electron is comparable with a typical quark length scale and consequently it can be successfully used for probing the proton structure.

The obtained DIS data from SLAC incited Richard Feynman to develop the quark-parton model [9] and provided more information on the behavior and interactions of the quarks in the nucleons. These theoretical-experimental achievements have led to the dramatic development of QCD which validity has been confirmed, in particular, by the discovery of the gluon at DESY

in 1979 [10].

An investigation of the electron-proton scattering process with a much higher resolution power became possible at the nineties due to beginning of the HERA collider operation. The much larger electron-proton center-of-mass energy, $\sqrt{s} = 225 - 319$ GeV, as compared to previous fixed target experiments, opened up a wider kinematic range for precision measurements of the proton structure. It made it possible to extend the measurements of the inclusive electron-proton scattering cross section to the kinematic region of low Bjorken-x variable and low absolute four momentum transfer squared, Q^2. From the cross section measurements the proton structure function F_2 and the longitudinal structure function F_L have been extracted. Therefore, HERA colliding experiments, H1 and ZEUS, allowed us to obtain more detailed information on the distribution of the partons in nucleons at the conditions have never studied before. The combination of the cross section data measured by the H1 and ZEUS collaborations made it possible to obtain more accurate values of the measured quantities.

The present thesis is devoted to the combination of the H1 and ZEUS inclusive cross section data and tests of the phenomenological low Bjorken-x models using these combined data. The data used for combination have been obtained during the reduced and nominal proton beam energy runs. The combination procedure is based on the minimization of the positive χ^2-function, assuming the uncorrelated measured data points within one experiment. The correlations of the systematic sources for different experiments are properly taken into account in the combination procedure. The DGLAP based QCD fits together with the phenomenological dipole model fits to the combined data have been performed and parameters of the models have been obtained. The longitudinal proton structure function is also extracted and compared with the results of previous analyses.

The combination method has been implemented as an independent averaging package. It can be successfully used for a combination of data from modern proton-proton experiments.

The plan of the thesis is as follows.

The second chapter contains a brief theoretical overview of DIS. The quark parton model, structure functions and QCD are introduced. The special attention is paid to some peculiar properties of the QCD. The low-x region is discussed in detail and relevant phenomenological models are described. Additionally, the QCD fits are discussed.

The third chapter is devoted to description of the HERA collider. The H1 detector is briefly described and a more detailed specification of some relevant submodules is given. Then, similar to H1 detector, the description of the ZEUS detector and its submodules related to analysed data is presented. In conclusion, the methods of kinematic reconstruction and the formula for determination of the cross section are given.

The fourth chapter describes the analysed H1 and ZEUS data. The parameters of the data and some aspects of the analyses are briefly described. The systematic error sources for the H1 and ZEUS cross sections are discussed.

The combination procedure is described in the fifth chapter. The minimization scheme leading to a system of linear equations is presented. A different treatment of the systematic uncertainties is discussed and the iterative procedure for minimization is presented.

The sixth chapter contains results of the combination of the H1 and ZEUS cross section data. The common bin grid for the combination is presented. The combination of the reduced proton beam energy, $E_p = 460, 575$ GeV, data are described and the averaged cross sections are given. The results of the QCD and low-x dipole model fits to HERA data and obtained combined data are shown and discussed in detail. The longitudinal structure function is also extracted from the reduced and nominal proton beam energy data and compared to published H1 results.

The summary of the work is given in the conclusion.

The appendix includes a description of the averaging program as well as tables of the combined cross sections and values of F_L.

Elementary particle	Mass, GeV	Charge, e	Spin, $\hbar$	I_3
Quarks				
u	0.0023	$+2/3$	$1/2$	$+1/2$
d	0.0048	$-1/3$	$1/2$	$-1/2$
c	1.275	$+2/3$	$1/2$	$+1/2$
s	0.095	$-1/3$	$1/2$	$-1/2$
t	173.5	$+2/3$	$1/2$	$+1/2$
b	4.18	$-1/3$	$1/2$	$-1/2$
Leptons				
e	0.000511	-1	$1/2$	$-1/2$
ν_e	$< 22 \cdot 10^{-9}$	0	$1/2$	$+1/2$
μ	0.1057	-1	$1/2$	$-1/2$
ν_μ	< 0.00017	0	$1/2$	$+1/2$
τ	1.777	-1	$1/2$	$-1/2$
ν_τ	< 0.015	0	$1/2$	$+1/2$
Bosons				
γ	0	0	1	0
g	0	0	1	0
Z^0	91.2	0	1	0
$W^\pm$	80.4	± 1	1	± 1

Table 1: The elementary particles and their properties according to PDG data [12]. The quarks and leptons are grouped into the generations. The electric charge is given in units of positron charge. I_3 is the third component of the weak isospin.

2 Theoretical overview

A brief theoretical overview of the Deep Inelastic Scattering is presented. Some general aspects of the quantum chromodynamics like asymptotic freedom, confinement and factorization are overviewed. The QCD corrections to the quark parton model resulted in the establishment of the nonzero longitudinal proton structure function are discussed. The physics at the low Bjorken-x region is considered and the relevant phenomenological dipole models are described. The QCD fits based on the DGLAP evolution equations and dipole models are presented.

2.1 Deep Inelastic Scattering

Deep Inelastic Scattering (DIS) at HERA is presented by the process of high energy electron[2] scattering off the charged constituents of the proton, i.e. quarks. The fundamental quark-lepton interaction in this DIS process is mediated by exchange of gauge bosons. There are two types of processes which can be probed at HERA:

- Neutral Current process (NC DIS), $ep \to eX$, which is mediated by the exchange of neutral gauge bosons (photon γ or Z^0 boson);
- Charged Current process (CC DIS), $ep \to \nu_e X$ which is mediated by exchange of the charged W^+ or W^- boson.

The two processes are characterized by the final state electron or neutrino, respectively. In this thesis, we consider inclusive scattering cross section which integrates over all possible final states of the hadronic system.

A schematic diagram of the inclusive DIS process at HERA is presented in Figure 1. Here k, k' denote the four-momenta of the incoming and outgoing electron, respectively. In a similar way, P and P' are the four-momenta of the initial proton and the hadronic final state X. The four-momentum of the exchanged boson is given by

$$q = k - k'. \tag{1}$$

The commonly used Lorentz invariants for definition of the kinematics of this inclusive DIS process at a given proton-electron center-of-mass energy squared, $s = (P + k)^2$, are [13]

1. the absolute four-momentum squared

$$Q^2 = -q^2 = -(k - k')^2, \quad Q^2 \in [0, s), \tag{2}$$

which is carried by the virtual photon.

[2] In the following, the generic name electron is used for electrons and positrons.

2. the inelasticity

$$y = \frac{P \cdot q}{P \cdot k}, \quad y \in [0, 1], \tag{3}$$

which in the proton rest frame corresponds to the fractional electron energy transfer by the exchanged boson to the proton. It also quantifies the ep scattering angle measured with respect to the electron direction in the center-of-mass frame.

3. the Bjorken scaling variable

$$x = \frac{Q^2}{2P \cdot q}, \quad x \in [0, 1], \tag{4}$$

which is interpreted as the longitudinal proton momentum fraction carried by the struck quark in the infinite momentum frame where the quark has zero transverse momentum.

The introduced variables are related by the formula

$$Q^2 = (s - M_P^2)xy, \tag{5}$$

where M_P is the proton mass. It defines that there are only two independent Lorentz invariant variables for description of the DIS kinematics at fixed ep center-of-mass energy $\sqrt{s}$.

The invariant mass squared W^2 of the hadronic final state is given by

$$W^2 = (q + P)^2 = M_P^2 + Q^2 \frac{1 - x}{x}. \tag{6}$$

This relation shows that low-x reactions correspond, at fixed Q^2, to large values of the invariant mass squared W^2. It also formally defines the terms *deep* and *inelastic* by requiring $Q^2 \gg M_P^2$ and $W^2 \gg M_P^2$, respectively. Therefore, the proton mass M_P may be neglected in the last two equations.

2.2 General definitions of DIS

2.2.1 Structure functions

For $Q^2 \ll M_Z^2$, where M_Z is the mass of the Z^0 boson, the inclusive process $e(k) + p(P) \to e(k') + X(P')$ can be described with a good approximation using the assumption of domination of the one-photon exchange. In the proton rest frame, the differential cross section for this process is factorized into the contraction of the leptonic tensor $L_{\mu\nu}$ and the hadronic tensor $W^{\mu\nu}$. It can be written as (see, for example, [14],[15])

$$d\sigma = \frac{2}{\mathcal{F}} \frac{d^3k'}{|k'|} \frac{\alpha^2}{Q^4} L_{\mu\nu} W^{\mu\nu}, \tag{7}$$

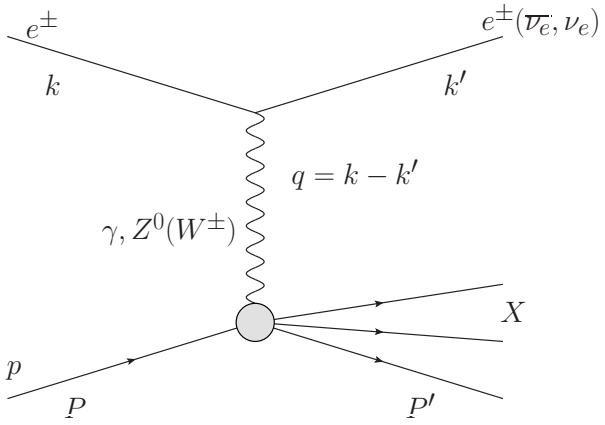

Figure 1: A schematic diagram of the Deep Inelastic Scattering process. k, k' denote the four-momenta of the incoming and outgoing electrons, P and P' are the four-momenta of the incoming proton and the hadronic final state X, respectively.

where $\mathcal{F} = 4|k|M_P$ is the flux factor, $\alpha = e^2/(4\pi)$ is the QED fine structure constant. Here the electron mass is neglected and the energy of outgoing electron is $E' = |k'|$. The leptonic tensor $L_{\mu\nu}$ is well known in QED and has the form [2]

$$L_{\mu\nu} = 2[k'_\mu k_\nu + k'_\nu k_\mu - (k \cdot k')g_{\mu\nu}]. \tag{8}$$

The conventional definition of the hadronic tensor $W^{\mu\nu}$ in terms of the Lorentz scalar functions W_i which are functions of two variables, usually taken to be x and Q^2, is

$$W^{\mu\nu} = W_1(x, Q^2)\left(-g_{\mu\nu} + \frac{q_\mu q_\nu}{q^2}\right) + W_2(x, Q^2)\left(P_\mu - \frac{P \cdot q}{q^2}q_\mu\right)\left(P_\nu - \frac{P \cdot q}{q^2}q_\nu\right). \tag{9}$$

The tensors $L_{\mu\nu}$ and $W_{\mu\nu}$ are symmetric under the interchange $\mu \leftrightarrow \nu$ and satisfy the gauge invariance constraints. These constraints reduce the contraction $L_{\mu\nu}W^{\mu\nu}$ to

$$L_{\mu\nu}W^{\mu\nu} = 8(k \cdot k')W_1 + 4\left[2(P \cdot k)(P \cdot k') - (k \cdot k')M_P^2\right]W_2. \tag{10}$$

Taking into account that due to the electron massless approximation $(k \cdot k') = -q^2/2$ and together with $(P \cdot k) = M_P E$, $(P \cdot k') = M_P E'$, in the $M_P^2/Q^2 \to 0$ limit the previous equation takes the form

$$L_{\mu\nu}W^{\mu\nu} = 8EM_P\left[xyW_1 + \frac{1-y}{y}\nu W_2\right], \tag{11}$$

where $\nu = (P \cdot q)$ and the dimensionless variables x, y have been introduced above. Writing $d^3k' = \pi E'\, dQ^2\, dy = 2\pi E'\nu\, dx\, dy$, one can obtain from (7) that at large $s = (k + P)^2 \approx 2EM_P$

the double differential cross section is given by

$$\frac{d^2\sigma}{dxdy} = \frac{4\pi\alpha^2 s}{Q^4}\left[xy^2F_1(x,Q^2) + (1-y)F_2(x,Q^2)\right]. \tag{12}$$

Here the Lorentz scalar functions W_i have been replaced by commonly used equivalents $F_1 = W_1, F_2 = \nu W_2$, which are dimensionless, frame invariant *structure functions* of the proton.

A closely related form, derived from (12) using (5) and a definition of *the longitudinal structure function* [16]

$$F_L(x,Q^2) = \left(1 + \frac{4M_p^2x^2}{Q^2}\right)F_2(x,Q^2) - 2xF_1(x,Q^2), \tag{13}$$

in our case reducing to

$$F_L = F_2 - 2xF_1 \tag{14}$$

as $M_P^2/Q^2 \to 0$, is

$$\frac{d^2\sigma}{dxdQ^2} = \frac{2\pi\alpha^2}{xQ^4}\left[Y\,F_2(x,Q^2) - y^2F_L(x,Q^2)\right], \tag{15}$$

where $Y = 1 + (1-y)^2$.

The dependence of the structure functions $F_1(x,Q^2)$ and $F_2(x,Q^2)$ on x and Q^2 has been extensively studied experimentally. The ep scattering experiment at SLAC showed [8] that the structure functions had little or no variation with Q^2 (see, for example, Figure 2) and appeared to depend only on the dimensionless variable $x = Q^2/(2\nu)$. This fact is a clear evidence of *the scaling hypothesis* [17] proposed by James Bjorken from a consideration based on the quark model current algebra. He predicted that in the deep inelastic region $Q^2 \to \infty$ (and also $\nu \to \infty$) with the fixed $x = Q^2/(2\nu)$ the structure functions are finite and scale as

$$\begin{aligned} F_1(x,Q^2) &\to F_1(x) \\ F_2(x,Q^2) &\to F_2(x). \end{aligned} \tag{16}$$

2.2.2 Quark Parton Model

The approximate Q^2-independence of the structure functions at large Q^2 has led Richard Feynman to the conclusion [9] that the virtual photon scatters off point-like constituents in the nucleon. He considered that at high Q^2 the virtual photon probes very short distances and time scales within proton and, consequently, it has to interact with one of the massless quark constituents (partons) within the proton. It is assumed that the parton carries only a certain fraction ξ of the proton's energy and momentum. Over the short time scales involved in the transfer of a large amount of energy, the struck constituent can be treated as effectively free. Therefore,

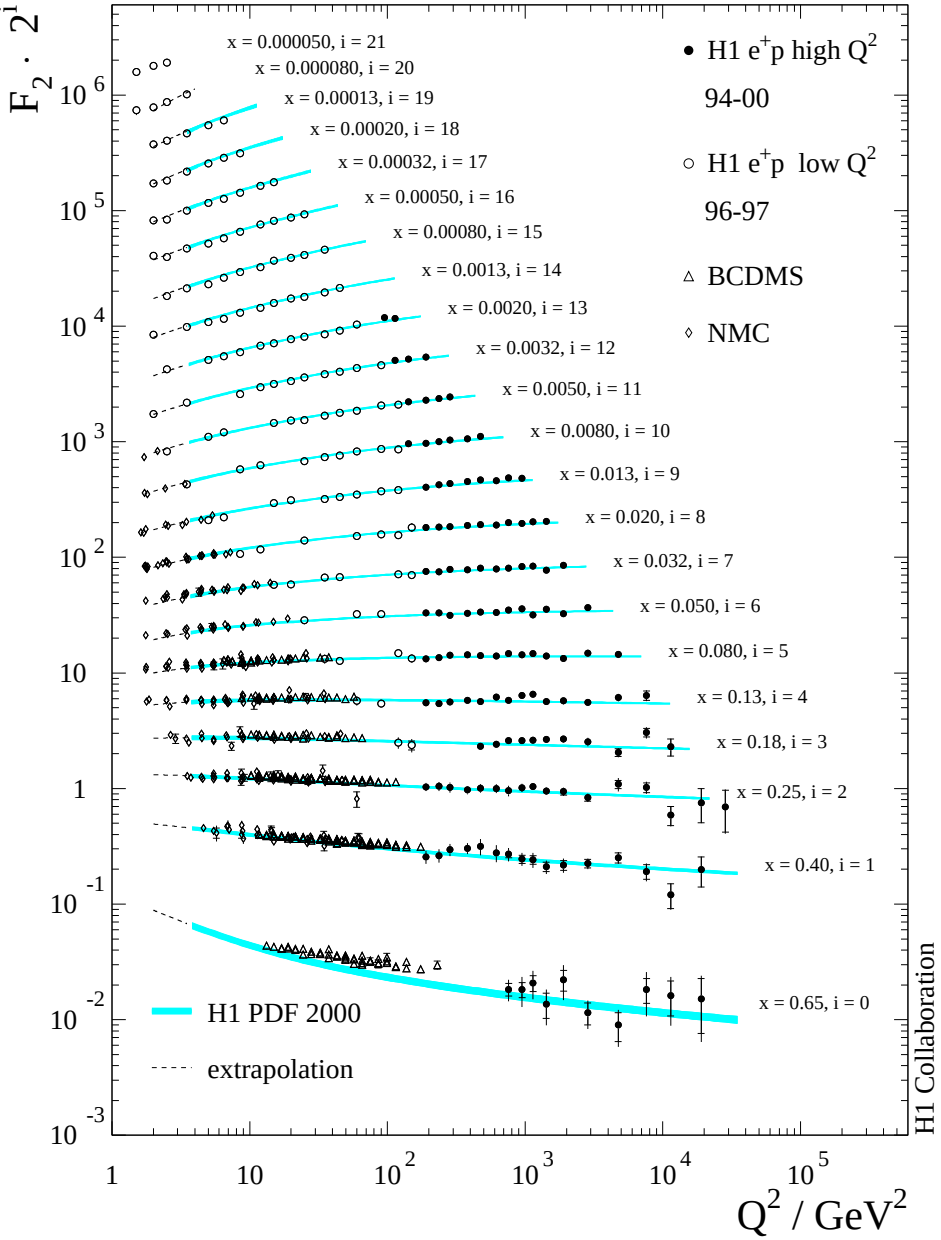

Figure 2: The proton structure function $F_2(x, Q^2)$ measured by the H1 collaboration [18] together with BCDMS [19] and NMC [20] fixed target results. The theoretical predictions obtained from the H1 PDF 2000 fit are also shown.

in the quark parton model (QPM) the deep inelastic electron-proton scattering is an incoherent sum of single elastic electron-quark scattering processes. As a result, the cross section is given by the sum over all relevant types of quarks and antiquarks

$$\frac{d^2\sigma}{dxdQ^2} = \sum_{q,\bar{q}} \int_0^1 \left[\frac{d^2\hat{\sigma}_{eq}}{dxdQ^2} \right] f_q(\xi)\, d\xi. \tag{17}$$

Here $f_q(\xi)$ is the probability of finding a quark q (or also an antiquark $\bar{q}$) with a fraction ξ of the proton's energy and longitudinal momentum. This probability $f_q(\xi)$ is called *the parton distribution function* (PDF).

Considering the elastic electron-quark scattering subprocess one can obtain [21] that the double differential cross section for the ep scattering process is

$$\frac{d^2\sigma}{dxdQ^2} = \frac{2\pi\alpha^2}{xQ^4} \sum_{q,\bar{q}} e_q^2 \, x \int_0^1 Y \, \delta(x-\xi) \, f_q(\xi) \, d\xi, \tag{18}$$

where e_q denote a fractional electric charge and $\delta(x-\xi)$ is the Dirac delta function. A comparison of the general structure function formula (15), assuming only γ exchange, with the obtained cross section (18) implies that

$$F_2(x, Q^2) = 2xF_1(x, Q^2) = \sum_{q,\bar{q}} e_q^2 x f_q(x). \tag{19}$$

Hence, in QPM the structure functions F_1 and F_2 depend only on the dimensionless variable x as it has been predicted by James Bjorken. The structure function F_1 is defined by the parton densities, whereas F_2 describes the momentum densities. The longitudinal structure function

$$F_L = F_2 - 2xF_1 = 0. \tag{20}$$

It is useful to introduce here the transversely and longitudinally polarized virtual photon scattering cross sections by formulas

$$\sigma_T = \frac{4\pi^2\alpha}{Q^2(1-x)} 2xF_1, \quad \sigma_L = \frac{4\pi^2\alpha}{Q^2(1-x)} F_L. \tag{21}$$

The ratio R defined as

$$R = \frac{\sigma_L}{\sigma_T} = \frac{F_L}{(F_2 - F_L)} \tag{22}$$

is often used instead of F_L to describe the scattering cross section. The QPM assumes that longitudinally polarized virtual photon scattering is forbidden due to helicity conservation [22] and F_L as well as R is zero. The equation (20) connecting F_1 and F_2 is called the Callan-Gross relation [22] and reflects the spin$-\frac{1}{2}$ nature of the quarks.

Taking advantage of the formula (19) it is clearly seen that the proton structure function is given by

$$F_2(x) = x\left(\frac{4}{9}[u(x) + \bar{u}(x)] + \frac{1}{9}[d(x) + \bar{d}(x) + s(x) + \bar{s}(x)] + \dots\right) \tag{23}$$

where $u(x)$ ($d(x)$, $s(x)$) is the PDF for u (d, s) quark in the proton, $\bar{u}(x)$ ($\bar{d}(x)$, $\bar{s}(x)$) for u (d, s) antiquark. The full power of the QPM formalism lies in the fact that same parton distribution

functions appear, in various combinations, for different target particles. For example, the neutron structure function arised in the electron-neutron scattering may be written in a similar way as follows:

$$F_2^n(x) = x\left(\frac{4}{9}[d(x) + \bar{d}(x)] + \frac{1}{9}[u(x) + \bar{u}(x) + s(x) + \bar{s}(x)] + \dots\right). \tag{24}$$

2.2.3 Sum rules

The quark distributions inside the proton satisfy some constraints. Since the proton has strangeness zero, we have a sum rule (treating only u, d and s flavours) [15]

$$\int_0^1 [s(x) - \overline{s}(x)]\, dx = 0 \tag{25}$$

It is customary to introduce the *valence* quarks

$$u_v = u - \overline{u} \tag{26}$$

$$d_v = d - \overline{d} \tag{27}$$

which are non-singlet combinations of the quark-antiquark distributions and the *sea* quarks

$$S = 2(\overline{u} + \overline{d} + \overline{s}). \tag{28}$$

The anti-quark and strange quark distributions are taken to be pure sea

$$s = \overline{s}, \tag{29}$$

where we have assumed that the sea is flavour-independent. Such approach replaces the six unknown functions now by three, and is consequently more predictive. Therefore, the sum rule (25) is satisfied automatically and the following relations are also hold: the Gross-Llewellyn Smith sum rule [23]

$$\int_0^1 [u_v(x) + d_v(x)]\, dx = 3 \tag{30}$$

and Adler sum rule [24]

$$\int_0^1 [u_v(x) - d_v(x)]\, dx = 1. \tag{31}$$

The last two equations define the conservation of the number of valence quarks.

Another crucially important sum rule is the momentum sum rule

$$\int_0^1 x\left[u_v(x) + d_v(x) + S(x)\right] dx = \int_0^1 x\left[u(x) + \overline{u}(x) + d(x) + \overline{d}(x) + s(x) + \overline{s}(x)\right] dx = 1 - \varepsilon. \quad (32)$$

Here ϵ is interpreted as the fraction of the proton momentum that is not carried by quarks. The integral in equation (32) is directly related to the cross section and its evaluation implies [25] $\varepsilon \simeq 0.4$. This clearly suggests that there is more momentum in proton than that carried by quarks and antiquarks. This fact provided the first indirect evidence of the gluonic component of the proton and served to development of QCD which interprets this phenomena.

2.3 Quantum Chromodynamics (QCD)

Quantum Chromodynamics is the non-Abelian gauge theory of strong interaction [3]. The theory postulates the existence of quarks and gluons which are the constituents of the hadronic matter and describes interactions between them. Based on the group of transformation SU(3), QCD introduces the colour degree of freedom which has three possible values (red, green, blue) and is carried by quarks and gluons. The interaction between quarks is mediated by the exchange of massless spin-1 gluons. Hadrons are considered to be colourless or colour singlets of the group SU(3) constructed from the fundamental colour triplet of quarks. The *colour confinement* property demands that quarks exist only in colour singlet states: quark-antiquark pairs $q\bar{q}$ corresponding to mesons and three-quark states qqq corresponding to baryons. The non-Abelian property of QCD leads to *asymptotic freedom* which predicts that the coupling of quarks and gluons is strong at large distances so as to confine quarks. At the same time, the coupling is predicted to be small at short distances so that quarks are almost free in high-energy reactions. This makes it possible to use the methods of perturbation theory [31] at such energies.

2.3.1 Asymptotic freedom

The perturbative methods of QCD consider some dimensionless observable[3] F by expanding it into a perturbation series in the QCD coupling $\alpha_s = g^2/4\pi$. The perturbation series needs to be renormalized in order to remove ultraviolet divergences which are the logarithmic divergences from the high order diagrams. For example, at leading order (LO) these diagrams are a quark loop and a gluon loop (see Figure 3). For renormalization the arbitrary mass parameter μ is introduced. It is called the renormalization scale and defines the point where removing of ultraviolet divergences is performed. Since F is dimensionless it can only depend on the dimensionless ratio Q^2/μ^2 and the coupling α_s which is in turn also renormalized and depends on μ. Hence, the dimensionless observable F has the functional dependence $F(Q^2/\mu^2, \alpha_s(\mu^2))$. Since

[3] for example, a structure function

the renormalization scale μ is an arbitrary parameter, F has to be independent of the choice of renormalization scale to be a physical observable. This fact is expressed by the renormalization group equation (RGE) [26]

$$\frac{d}{d\ln\mu^2}F = \mu^2\frac{d}{d\mu^2}F = \left(\mu^2\frac{\partial}{\partial\mu^2} + \mu^2\frac{\partial\alpha_s}{\partial\mu^2}\frac{\partial}{\partial\alpha_s}\right)F = 0. \tag{33}$$

It is possible to show that the solution of (33) is $F(1, \alpha_s(Q^2))$ and, as a result, the running of QCD coupling α_s exclusively determines the Q^2-dependence of F.

The running of QCD coupling $\alpha_s(Q^2)$ is generally expressed in terms of a β function by RGE which is given by the formula

$$\frac{\partial}{\partial\ln Q^2}\alpha_s(Q^2) = \beta\left(\alpha_s(Q^2)\right). \tag{34}$$

The β function has a perturbative expansion

$$\beta(\alpha_s) = -\alpha_s\sum_{n=0}^{\infty}\beta_n\left(\frac{\alpha_s}{4\pi}\right)^{(n+1)}, \tag{35}$$

where the coefficients β_n of the perturbative series depend on the number of active quark flavours n_q and are extracted from the high-order corrections to the bare vertices of the theory. Taking into account only the diagrams which contribute to the β function of QCD in the one-loop approximation, the only term β_0 in the series (35) is retained. These one-loop diagrams are presented in Figure 3. The two-term expansion of the perturbative series sums up the next-to-leading (NLO) contributions arising from the two-loop diagram shown in Figure 4. The two first coefficients of the perturbative series (35) are given by relations

$$\beta_0 = \frac{33 - 2n_q}{3}, \quad \beta_1 = \frac{306 - 38n_q}{3}. \tag{36}$$

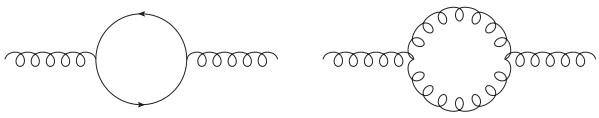

Figure 3: Graphs which contribute to the β function of QCD in the one-loop approximation.

It is possible to obtain the simplest LO relation between $\alpha_s(\mu^2)$ and $\alpha_s(Q^2)$ if both are in the perturbative region by truncating the series (35) to the first term only. This relation is given by

formula

$$\alpha_s(Q^2) = \frac{\alpha_s(\mu^2)}{1 + \alpha_s(\mu^2)\left(\frac{\beta_0}{4\pi}\right)\ln(Q^2/\mu^2)}. \tag{37}$$

Evidently as $\ln(Q^2/\mu^2)$ becomes large and since $n_q \leq 16$, the running coupling $\alpha_s(Q^2)$, generally speaking, decreases to zero, making perturbative methods to be valid. This property of *asymptotic freedom* explains how QCD compounds confined quarks at the small (mass) scales and almost free quarks in scattering processes at large Q^2. Perturbative QCD defines how the QCD coupling varies with the scale, but the absolute value of $\alpha_s(\mu^2)$ at specific, reference scale $\mu = Q_0$ has to be obtained from experiment. This reference scale is conventionally chosen to be the mass of the Z-boson M_Z which is large enough to be in perturbative region.

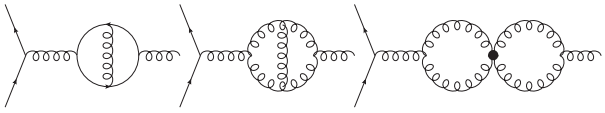

Figure 4: Graphs which contribute to the β function of QCD in the two-loop approximation.

The QCD coupling at a reference scale is a fundamental parameter of QCD and its measurements at the different scales are of crucial importance. The measured values of $\alpha_s(Q^2)$ as well as the two loop solution of RGE obtained by evolving the $\alpha_s(M_Z)$ are presented in Figure 5. The current world average value of QCD coupling is [12]

$$\alpha_s(M_Z) = 0.1184 \pm 0.0007. \tag{38}$$

2.3.2 Confinement

The coupling becomes large for effectively low Q^2. The parameter Λ defining the energy scale at which the coupling diverges is determined directly from (34), which can be rewritten as

$$\ln\left(\frac{Q^2}{\Lambda^2}\right) = -\int_{\alpha_s(Q^2)}^{\infty} \frac{dx}{\beta(x)}. \tag{39}$$

The $\alpha_s(Q^2)$ can be expressed in terms of introduced parameter Λ by integrating the right part of (39), taking into account some first terms of the β function. At NLO, following the β function expansion (35), the approximate expression for $\alpha_s(Q^2)$, is [28]

$$\alpha_s(Q^2) = \frac{4\pi}{\beta_0 \ln(Q^2/\Lambda^2)}\left(1 - \frac{\beta_1}{\beta_0^2}\frac{\ln[\ln(Q^2/\Lambda^2)]}{\ln(Q^2/\Lambda^2)}\right). \tag{40}$$

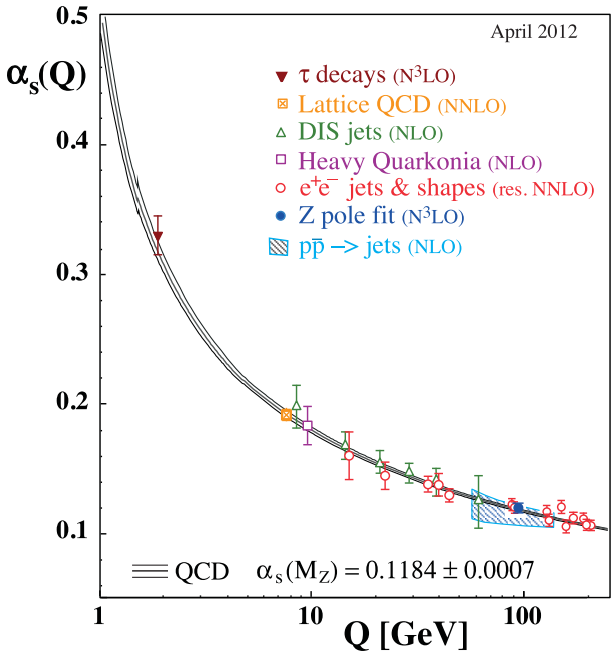

Figure 5: Up to date measurements [12] of α_s as a function of Q^2. The degree of QCD perturbation theory used for the extraction of α_s is indicated. The perturbative QCD prediction is also shown.

Hence Λ indicates the boundary at which $\alpha_s(Q^2)$ becomes infinite and coupling becomes strong. Depending on the exact definition, its value is about 0.3 GeV. Thus $\alpha_s(Q^2)$ becomes large and perturbative theory breaks down for scale comparable with the masses of the light hadrons, i.e. $Q^2 \simeq 1\text{GeV}$. This could be an indication that the *confinement* of quarks and gluons inside hadrons is actually a consequence of the growth of the coupling at low scales, which is a corollary of the decrease at high scales that leads to asymptotic freedom.

In conclusion, it is necessary to mention that the coefficients (36) depend on the number of active quark flavours n_q, usually considered to be 3, 4, or 5. As Q increases through the flavour threshold the values of β_n change, but $\alpha_s(Q^2)$ should be a continuous function of Q^2 at the threshold. From (40) it immediately follows that value of Λ also depends on n_q. Therefore, the energy scale parameter Λ depending on the renormalization scale and order of perturbation theory, should be also given with respect to n_q.

2.3.3 QCD-improved parton model

Withing a framework of the QCD perturbation theory, the QPM formula (19) may be regarded as the LO term in the expansion of F_2 as a power series in α_s. The inclusion of the NLO ($O(\alpha_s)$) terms requires the calculation of the photon-parton subprocess diagrams shown in Figure 6. The account of these subprocesses produces the Bjorken scaling violation which lies in the $\ln(Q^2)$-dependence of the structure functions. In the subprocess $\gamma q \to qg$ the emission of a gluon with

four-momentum k parallel to the outgoing quark gives a *collinear* divergence contribution to the structure function. This logarithmic divergence originates from the integration over the gluon transverse momentum k_t

$$\int_{\kappa^2}^{Q^2} \frac{1}{k_t^2}\, dk_t^2 = \ln\left(\frac{Q^2}{\kappa^2}\right), \tag{41}$$

where the upper limit is given by the virtuality of the photon. Here the arbitrary scale parameter κ is introduced in order to deal with the lower limit of integration which should be zero. The structure function is obtained by a convolution of the parton distribution $f_q(x)$ with the quark structure function deduced up to the $O(\alpha_s)$ order. The result is

$$F_2(x, Q^2) = \sum_{q,\bar{q}} x\, e_q^2 \int_x^1 \frac{d\xi}{\xi}\, f_q(\xi) \left[\delta(1 - \frac{x}{\xi}) + \frac{\alpha_s}{2\pi}\left(P\left(\frac{x}{\xi}\right) \ln\frac{Q^2}{\kappa^2} + C\left(\frac{x}{\xi}\right)\right)\right], \tag{42}$$

where P is the *universal parton splitting function* and C is a process dependent *coefficient function*. The collinear singularities can be absorbed into the parton distribution f_q at some factorization scale μ_F, therefore one can replace f_q by the nonperturbative running PDF

$$f_q(x, \mu_F^2) = f_q(x) + \frac{\alpha_s}{2\pi} \int_x^1 \frac{d\xi}{\xi}\, f_q(\xi) \left(P\left(\frac{x}{\xi}\right) \ln\frac{\mu_F^2}{\kappa^2} + C\left(\frac{x}{\xi}\right)\right). \tag{43}$$

As a result, the proton structure function is given by

$$F_2(x, Q^2) = \sum_{q,\bar{q}} x\, e_q^2 \int_x^1 \frac{d\xi}{\xi}\, f_q(\xi, \mu_F^2) \left[\delta(1 - \frac{x}{\xi}) + \frac{\alpha_s}{2\pi} P\left(\frac{x}{\xi}\right) \ln\frac{Q^2}{\mu_F^2}\right]. \tag{44}$$

The parton distribution $f_q(x, \mu_F^2)$ cannot be calculated by methods of perturbative theory, because it obtains contributions from the non-perturbative part of strong interactions. Nevertheless, its μ_F^2-dependence is calculable using the DGLAP evolution equations, which are described in detail in the next section. The PDFs are determined from the experimental data at some specific scale. Similarly to the renormalization scale, it is convenient to choose the factorization scale to be $\mu_F = Q$.

The complete description of the DIS structure functions in terms of parton distribution functions also demands consideration of the $\gamma g \to q\bar{q}$ contribution. This process is shown in Figure 6 (left). Taking into account the gluon distribution $f_g(\xi, Q^2)$, the structure function F_2 is given

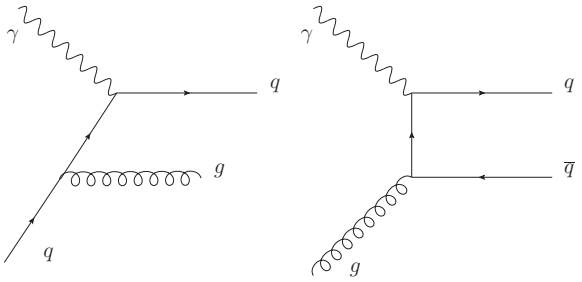

Figure 6: The diagrams of $\gamma q \to qg$ and $\gamma g \to q\bar{q}$ processes. The real gluon emission diagram (left) gives a collinear divergence.

by

$$F_2(x,Q^2) = \sum_{q,\bar{q}} x\, e_q^2 \int_x^1 \frac{d\xi}{\xi} \left\{ f_q(\xi,Q^2) \left[\delta(1-\frac{x}{\xi}) + \frac{\alpha_s}{2\pi} C_q\left(\frac{x}{\xi}\right) \right] + f_g(\xi,Q^2)\, C_g\left(\frac{x}{\xi}\right) \right\}. \qquad (45)$$

The functions $C_q(x)$ and $C_g(x)$ are the coefficient functions. They depend on the factorization and normalization schemes and are different for different structure functions F_a.

It is necessary to note that although all the collinear singularities are absorbed by the running of f_i, there is an ambiguity in the treatment of the finite contributions. The absorption of the finite contribution is defined by the factorization scheme. The two schemes are used: DIS scheme [29] which defines the coefficient functions equal to zero for all non-leading orders of perturbation theory; the minimal subtraction scheme $\overline{\text{MS}}$ [30] which is currently used and gives non-zero coefficients.

Factorization is a fundamental property of QCD and is general for all DIS processes. For the structure function F_a, describing the DIS process $ep \to eX$, the factorization formula has the generic form

$$F_a(x,Q^2) = \sum_{q,\bar{q},g} \int_x^1 \frac{d\xi}{\xi}\, f_q(\xi,Q^2)\, C_{a,q}\left(\frac{x}{\xi}, \alpha_s(Q^2)\right) + O\left(\frac{\Lambda^2}{Q^2}\right). \qquad (46)$$

For high Q^2 the last term, denoting the non-perturbative contributions, vanishes. The expression factorizes into universal parton distribution functions f_q, which absorb the long distance collinear singularities, and coefficient functions $C_{a,q}$, which describe the short distance subprocess. The coefficient functions are calculated in perturbative QCD as a power series in α_s and are unique for particular observable F_a.

2.3.4 DGLAP evolution equations

As it has been already mentioned, the parton distribution functions f_q are not calculable in the perturbative QCD, but the dependence of $f_q(x, \mu_F^2)$ on μ_F^2 can be treated. The structure function $F_2(x, Q)$ does not depend on factorization scale, therefore by analogy with (33) taking the logarithmic derivative of both sides of (44) one can obtain the equation which describes the variation of $f_q(x, \mu_F^2)$ with the scale μ_F^2. It is natural to define the factorization scale $\mu_F^2 = Q^2$ and proceed to the dependence of parton densities on Q^2. This Q^2-dependence of parton distributions is described by the Dokshitzer-Gribov-Lipatov-Altarelli-Parisi (DGLAP) evolution equations [31]. They are coupled equations for the change of the quark, antiquark and gluon densities as $\ln Q^2$ changes:

$$\frac{\partial}{\partial \ln Q^2}\begin{pmatrix} q_i(x,Q^2) \\ g(x,Q^2)\end{pmatrix} = \frac{\alpha_s(Q^2)}{2\pi}\sum_j \int_x^1 \frac{d\xi}{\xi}\begin{pmatrix} P_{q_iq_j}\left(\frac{x}{\xi},\alpha_s(Q^2)\right) & P_{q_ig}\left(\frac{x}{\xi},\alpha_s(Q^2)\right) \\ P_{gq_i}\left(\frac{x}{\xi},\alpha_s(Q^2)\right) & P_{gg}\left(\frac{x}{\xi},\alpha_s(Q^2)\right)\end{pmatrix}\begin{pmatrix} q_i(\xi,Q^2) \\ g(\xi,Q^2)\end{pmatrix}. \quad (47)$$

Here g corresponds to the gluon density and q_i, q_j denote both quark and antiquark distributions.

The splitting functions $P_{ba}(z, \alpha_s(Q^2))$ describe the probability of a parent parton a to produce a daughter parton b with momentum fraction z by the emission of a parton with momentum fraction $1 - z$. They are presented graphically in Figure 7. The splitting functions are expanded as power series in $\alpha_s(Q^2)$

$$P_{ba}(z, \alpha_s) = P_{ba}^{(0)}(z) + \frac{\alpha_s}{2\pi}P_{ba}^{(1)}(z) + \cdots \quad . \quad (48)$$

The LO expressions for splitting functions are given by

$$\begin{aligned} P_{qq}^{(0)}(z) &= \tfrac{4}{3}\left[\tfrac{1+z^2}{(1-z)_+} + \tfrac{3}{2}\delta(1-z)\right], \\ P_{qg}^{(0)}(z) &= \tfrac{1}{2}\left[z^2 + (1-z)^2\right], \\ P_{gq}^{(0)}(z) &= \tfrac{4}{3}\left[\tfrac{1+(1-z)^2}{z}\right], \\ P_{gg}^{(0)}(z) &= 6\left[\tfrac{1-z}{z} + \tfrac{z}{(1-z)_+} + z(1-z)\right] + \left[\tfrac{33-2n_q}{6}\right]\delta(1-z), \end{aligned} \quad (49)$$

where $[f(z)]_+ = f(z) - \delta(1-z)\int_0^1 f(t)\,dt$.

The efficient method to calculate the evolution of the individual quark distributions is to introduce a singlet and non-singlet quark distributions. Typical examples of non-singlet combinations are the difference of quark and antiquark distribution functions, valence quarks, or the difference of up and down quark distributions. For the flavor non-singlet quark distribution, q^{NS}, and the flavour-singlet quark and gluon distributions, $q^S = \sum_i (q_i + \bar{q}_i)$ and g, the DGLAP

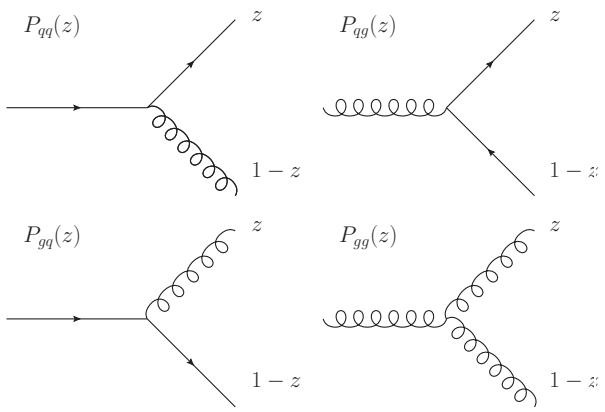

Figure 7: The splitting functions and the diagrams which correspond to them.

evolution equations read as follows:

$$\begin{gathered}\frac{\partial q^{NC}(x,Q^2)}{\partial \ln Q^2} = \frac{\alpha_s(Q^2)}{2\pi}\int_x^1 \frac{d\xi}{\xi} q^{NC}(\xi,Q^2) P_{qq}\left(\frac{x}{\xi},\alpha_s(Q^2)\right) \\ \frac{\partial}{\partial \ln Q^2}\begin{pmatrix} q^S(x,Q^2) \\ g(x,Q^2)\end{pmatrix} = \frac{\alpha_s(Q^2)}{2\pi}\int_x^1 \frac{d\xi}{\xi}\begin{pmatrix} P_{qq}\left(\frac{x}{\xi},\alpha_s(Q^2)\right) & 2n_q P_{qg}\left(\frac{x}{\xi},\alpha_s(Q^2)\right) \\ P_{gq}\left(\frac{x}{\xi},\alpha_s(Q^2)\right) & P_{gg}\left(\frac{x}{\xi},\alpha_s(Q^2)\right)\end{pmatrix}\begin{pmatrix} q^S(\xi,Q^2) \\ g(\xi,Q^2)\end{pmatrix}.\end{gathered} \tag{50}$$

The DGLAP equations provide a rigorous formalism for calculating the changes to the parton densities as Q^2 changes, but they do not allow a calculation of the distributions at the starting scale Q_0. This information has to come from non-perturbative methods or by parameterizing the x dependence of the parton density at the starting scale and determining the parameters by fitting to data. The latter is described in detail in the section devoted to QCD fits.

2.3.5 The longitudinal structure function in QCD

The LO description of the electron-parton scattering process assumes focusing on the electromagnetic exchange in which a photon couples to the quarks and antiquarks and the contribution of $\gamma q \to q$ process is only considered. For massless $\frac{1}{2}$-spin partons, the calculation gives that for this process the Callan-Gross relation (19)

$$F_L \equiv F_2 - 2xF_1 = 0 \tag{51}$$

holds.

The QCD NLO corrections ($O(\alpha_s)$) to the structure functions arising from the interaction of the virtual photon with a quark preceded by its emission of the gluon and with the gluon as a parton of the proton (see Figure 6) lead to their dependence on Q^2 and, consequently, to broken of the Bjorken scaling by logarithms of Q^2. It means that the Callan-Gross relation is no longer

satisfied and $F_L \neq 0$. The one-loop virtual correction to $\gamma q \to q$ process does not contribute to the longitudinal part of the partonic tensor [32] $\hat{W}^L_{\gamma q}$ and to order α_s the calculation of the longitudinal part of this tensor gives that

$$\hat{W}^L_{\gamma q} = \frac{1}{3}\frac{\alpha_s}{2\pi} e_q^2 \frac{Q^2}{\xi} + O(\epsilon) \tag{52}$$

and

$$\hat{W}^L_{\gamma g} = \frac{1}{2}\frac{\alpha_s}{2\pi} e_q^2 \frac{Q^2(1-\xi)}{\xi} + O(\epsilon) \tag{53}$$

for the $\gamma q \to qg$ and $\gamma g \to q\bar{q}$ contributing processes, respectively. The contributions of ϵ-order are defined by the factorization scheme. The structure functions of the gluon emission processes are, in turn, expressed by relations

$$F_1^{\gamma q}(x, Q^2) = \frac{1}{2x} F_2^{\gamma q}(x, Q^2) - \sum_{q,\bar{q}} e_q^2 \frac{\alpha_s}{2\pi} \int_x^1 \frac{d\xi}{\xi} \frac{4}{3} q(\xi, Q^2) \frac{x}{\xi} \tag{54}$$

and

$$F_1^{\gamma g}(x, Q^2) = \frac{1}{2x} F_2^{\gamma q}(x, Q^2) - \sum_{q,\bar{q}} e_q^2 \frac{1}{2}\frac{\alpha_s}{2\pi} \int_x^1 \frac{d\xi}{\xi} g(\xi, Q^2) 4 \frac{x}{\xi}\left(1 - \frac{x}{\xi}\right). \tag{55}$$

Combining the results, it is possible to obtain an expression for the longitudinal structure function F_L with $O(\alpha_s)$ leading terms

$$\begin{gathered} F_L(x, Q^2) \equiv F_2(x, Q^2) - 2xF_1(x, Q^2) = \\ = \frac{\alpha_s(Q^2)}{2\pi} \int_x^1 \frac{d\xi}{\xi} \left[\frac{8}{3} \left(\frac{x}{\xi}\right)^2 \left(\sum_{q,\bar{q}} e_q^2 \, \xi \, q(\xi, Q^2) \right) + 4\bar{e} \left(\frac{x}{\xi}\right)^2 \left(1 - \frac{x}{\xi}\right) \xi g(\xi, Q^2) \right] = \\ = \frac{\alpha_s(Q^2)}{2\pi} \int_x^1 \frac{d\xi}{\xi} \left[\frac{8}{3} \left(\frac{x}{\xi}\right)^2 F_2(\xi, Q^2) + 4\bar{e} \left(\frac{x}{\xi}\right)^2 \left(1 - \frac{x}{\xi}\right) \xi g(\xi, Q^2) \right]. \end{gathered} \tag{56}$$

where $\bar{e} = \sum_{q,\bar{q}} e_q^2$ and the sum runs over all active quark and antiquark flavours. For example, $\bar{e} = 10/9$ for four quark flavours.

It is necessary to note that the obtained expression (56) is independent of the factorization scheme. Equation (56) also shows that the ratio (22) $R \sim \alpha_s$ instead of being zero at the LO approximation. Running of the coupling as $Q^2 \to \infty$ leads, in turn, to the QPM prediction $R \to 0$.

Another similar approach to the deduction of the expression for the longitudinal structure function F_L is based on the consideration of the transversely and longitudinally polarized photon-parton cross sections [33]. For $\gamma q \to qg$ and $\gamma g \to q\bar{q}$ processes the cross sections of the longitudinally polarized photon scattering off the parton σ_L are nonzero. They have been calculated and used in the factorization formula (46).

An independent measurements of F_L and comparison with predictions obtained from the

gluon distribution according to (56) represent a crucial test on the validity of perturbative QCD at low x. The most recent F_L data measured at HERA together with different NLO and NNLO predictions [34] are shown in Figure 8.

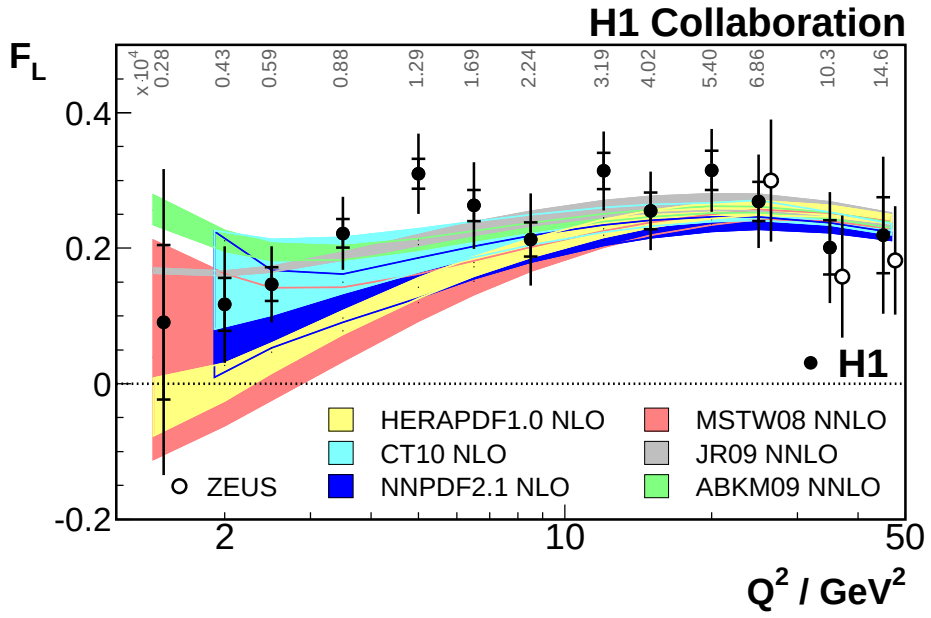

Figure 8: The longitudinal proton structure function F_L shown as a function of Q^2. The results from the H1 collaboration are shown by black solid symbols, whereas the ZEUS data are shown by white open points. The average x values for each Q^2 are indicated. The inner error bars represent statistical error, the full error bars include the statistical uncertainties added in quadrature. The bands represent predictions based on HERAPDF1.0, CTEQ6.6 and NNPDF2.1 NLO as well as MSTW08, JR09 and ABKM09 NNLO calculations [34].

2.4 Low-x physics

2.4.1 Introduction

The low-x region is crucially important for understanding of the proton structure. The region of small x, below 0.01, is characterized by domination of dense gluonic systems. In this region the gluons in the proton form a strongly correlated system of interacting particles. The gluon distribution shows a strong rise in x as $x \to 0$ for all values of Q^2. Through the coupling to the sea quarks $g \to q\bar{q}$, this strong rise leads to a rise of the proton structure function F_2. Interestingly enough, the increase of the gluon distribution with decreasing of x is not unlimited. If the gluon density becomes large the recombination and annihilation of gluons becomes important. This effect is called *parton saturation* and leads to a mitigation of the strong rise.

The low-x region is subject to the dedicated experimental exploration at HERA. As it is shown on the (x, Q^2) kinematic plane in Figure 9, only the HERA collider made it possible to

experimentally explore the low-x region. The discovery of a rising of the structure function F_2

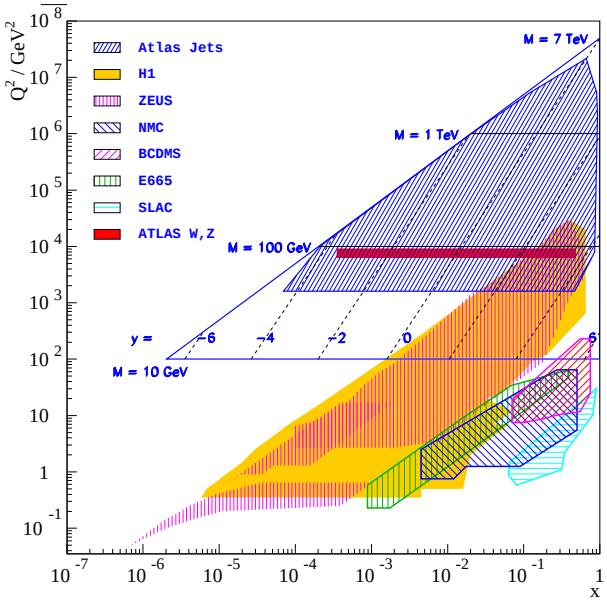

Figure 9: The (x, Q^2) kinematic plane with the different experimental coverings.

as x decreases at HERA was the remarkable starting point for further investigation of the proton structure at DESY.

The DGLAP evolution equations are unable to adequately describe the data at low values of x because at this region should be taken into account not only the leading $\alpha_S \ln Q^2$ terms but also the leading $\alpha_S \ln(1/x)$ contributions. As a result, different evolution techniques have been developed. One of the approaches for describing the evolution over x is the BFKL equation [35], which provides a mechanism for summing up the contributions of multiple gluon emission at small x. Another approach to treat the $\ln(1/x)$ terms is to include them into the coefficient and splitting functions [36]. The technique to calculate these $\ln(1/x)$ corrections is based on the so-called k_T factorization theorem [37].

At HERA, the low-x region corresponds to low Q^2. The non-perturbative contributions to the structure functions, which manifest themselves as power corrections (46) become significant at low Q^2. However, since $1/x$ is large, one can build perturbative QCD-inspired phenomenological models which are able to describe the data well. Some of these phenomenological models for description of the low-x deep inelastic scattering data at HERA are presented below. They are three dipole models which make it possible to describe the data for the transition from the perturbative ($Q^2 \gg M_P$) to the nonperturbative photoproduction ($Q^2 \approx 0$) region.

2.4.2 The rise of F_2

2.4.2.1 The rise of $F_2(x, Q^2)$ with respect to Q^2

The expression (19) for the structure function $F_2(x, Q^2)$ may be considered as plausible approximation for its description at $Q^2 > 10\ \mathrm{GeV}^2$. Using this formula in the first equation of DGLAP (50) it is possible to obtain [15] the following leading order equation for the coupled evolution of F_2 and gluon distribution $xg(x)$

$$\frac{\partial F_2(x,Q^2)}{\partial \ln Q^2} = \frac{\alpha_s(Q^2)}{2\pi}\int\limits_x^1 \frac{d\xi}{\xi}\left\{F_2(\xi,Q^2)P_{qq}\left(\frac{x}{\xi},\alpha_s(Q^2)\right) + xg(\xi,Q^2)2\overline{e}^2 P_{qg}\left(\frac{x}{\xi},\alpha_s(Q^2)\right)\right\}, \quad (57)$$

where $\overline{e}^2 = \sum_{q,\bar{q}} e_q^2$. Besides that, taking into account the LO behavior of the splitting functions as $x/\xi = z \to 0$

$$P_{qq}(z) \to \frac{4}{3}, \quad P_{qg}(z) \to \frac{1}{2}, \quad P_{gq}(z) \to \frac{8}{3z}, \quad P_{gg}(z) \to \frac{6}{z}, \quad (58)$$

one can show that the gluon distribution, governed by

$$\frac{\partial g(x,Q^2)}{\partial \ln Q^2} \approx \frac{\alpha_s(Q^2)}{2\pi}\int\limits_x^1 d\xi\,\frac{6}{x}\,g(\xi,Q^2), \quad (59)$$

becomes large as $x \to 0$ and its contribution to the evolution of F_2 becomes dominant. As a result, the gluon distribution determines the rise of $F_2(x, Q^2)$ as Q^2 increases and the contribution of the valence quarks is negligible [38].

2.4.2.2 The rise of $F_2(x, Q^2)$ with respect to x

If x is small and Q^2 is not large enough to reach the perturbative region the DGLAP approximation desist to be valid. At low x, terms in $\ln(1/x)$ become large and the conventional leading $\ln Q^2$ summation of the DGLAP equations may not be able to account for this. The summation of leading $\ln(1/x)$ terms can be performed by the BFKL equation. Thus, the region of DGLAP validity is defined by the relation

$$\alpha_s(Q^2)\ln 1/x \ll \alpha_s(Q^2)\ln Q^2/Q_0^2 \approx 1, \quad (60)$$

whereas for the BFKL equations the opposite relation

$$\alpha_s(Q^2)\ln Q^2/Q_0^2 \ll \alpha_s(Q^2)\ln 1/x \approx 1 \quad (61)$$

holds. To LO in $\ln(1/x)$ with fixed α_s, the BFKL approach predicts a steep power law behavior of the gluon density

$$xg(x,Q^2) \sim x^{-\lambda_g(Q^2)}, \quad (62)$$

where $\lambda_g(Q^2) = 3\alpha_s(Q^2)\pi^{-1}4\ln 2 \approx 0.5$ for $Q^2 \approx 4\ \mathrm{GeV}^2$. Therefore, the x-dependence of the structure function is $F_2 \sim x^{-\lambda_g(Q^2)}$.

2.4.3 GBW dipole model

The dipole models provide an fruitful approach for exploration of behavior of the structure functions at low-x region. They describe the processes in the saturation regime, in particular when the partons form a dense system in the proton. This state is characterized by the mutual interaction and recombination which also leads to the saturation [39] of the total cross section.

The original dipole model [40] proposed by K. Golec-Biernat and M. Wüsthoff (GBW) describes the γp scattering process and estimates corresponding cross section for $x \leq 0.01$. The model is based on the fact that the photon splits into quark-antiquark pair, dipole, far upstream the proton target, which then scatters on the proton. A schematic diagram of the process is presented in Figure 10. The scattering reaction is mediated by the single gluon exchange in the perturbative regime and changes into the multigluon exchange in the saturation region. At low x, the mechanism leading to the dissociation of the photon and subsequent scattering can be factorized and written in terms of the photon wave function, convoluted with the quark-antiquark cross section. It allows one to separate between the perturbative wave function of the photon which describes the dissociation of the photon into a quark-antiquark pair and the interaction of the pair with a proton target.

Within the described formalism, the transversely and longitudinally polarized virtual photon scattering cross sections (21) are given by

$$\sigma_{T,L}(x, Q^2) = \int d^2\mathbf{r} \int_0^1 dz\, |\Psi_{T,L}(z, \mathbf{r})|^2\, \sigma(x, r^2), \tag{63}$$

where $\mathbf{r}$ is the relative transverse separation between quark and antiquark, $\Psi_{T,L}(z, \mathbf{r})$ is the photon wave function, and $\sigma(x, r^2)$ is the quark-antiquark cross section. The latter is modeled by the simple approximation

$$\sigma(x, r^2) = \sigma_0 \left(1 - \exp\left[-\frac{r^2}{4R_0^2(x)}\right]\right), \tag{64}$$

which indicates two important features of the $q\bar{q}$ cross section: for small r it is proportional to r^2 that reflects the property of color transparency and for large r it becomes a constant that ensures saturation. Here $R_0^2(x) = (x/x_0)^\lambda$ is the x-dependent saturation scale which is a measure of the transverse separation of the gluons in the proton. Therefore, for small x and small Q^2 the dipole separation is large compared to the gluon separation ($r \gg R_0(x)$) and $\sigma(x, r^2) \sim \sigma_0$. Using the latter in (63), it is possible to obtain the Q^2-dependence of the structure function F_2 for small Q^2. Because of the x-dependence of R_0, $\sigma(x, r^2)$ saturates for smaller dipoles sizes

as x decreases. The boundary along which saturation approaches is defined by the *critical line* $Q^2_{sat}(x) = 1/R^2_0(x)$.

The three free parameters σ_0, x_0 and λ are obtained from the QCD fit to DIS data. The reasonable description of the inclusive DIS data for $x \leq 0.01$ has been observed by the authors.

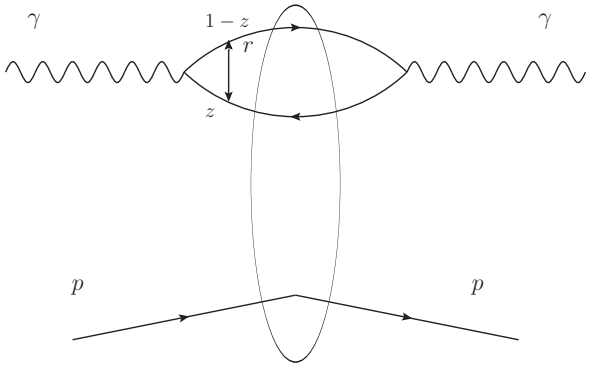

Figure 10: A schematic diagram of the quark-antiquark pair (dipole) scattering on the proton target.

2.4.4 IIM dipole model

The dipole model proposed by E. Iancu, K.Itakura, S. Munier (IIM) [41] is based on the Color Glass Condensate (CGC) [42] state of the low-x gluons at high energies. This state is characterized by the saturation momentum $Q_{sat}(x) \sim 1/x$ which is a measure of the gluon density in the impact parameter space.

Within the proposed approach, only the dipole scattering is treated and the corresponding cross section $\sigma(x, r^2)$ changes the form. The proton is considered as a homogeneous disk of radius R, therefore the dipole cross section is given by

$$\sigma(x, r^2) = \sigma_0 \mathcal{N}(x, r^2), \tag{65}$$

where $\sigma_0 = 2\pi R^2$ and $\mathcal{N}(x, r^2)$ is a known function. The latter is expressed by smooth interpolation of the approximate solution to the BFKL evolution equation for small dipole sizes ($r \ll R_0(x)$) and the Levin-Tuchin law [43] for large dipole sizes ($r \gg R_0(x)$). As a result, the dipole cross section is given by the formulas

$$\sigma(x, r^2) = \sigma_0 \begin{cases} \mathcal{N}_0 \quad \left(\tau^2\right)^{\gamma_s + \frac{\ln(\tau)}{\kappa\lambda\ln(x)}} & \text{if } \tau \leq 1 \\ \left(1 - \exp[-a \ln^2(2b\ \tau)]\right) & \text{if } \tau > 1 \end{cases} \tag{66}$$

where $\tau = r/2R_0(x) = r/\left(2(x/x_0)^{\lambda/2}\right)$. The constants $\gamma_s = 0.63$ and $\kappa = 9.9$ are determined by their LO BFKL values. The coefficients a and b are defined by continuity of the solution and

its first derivative at $\tau = 1$. The parameter N_0 is obtained from the fit to data and fixed to be 0.7 because of the small fit dependence on it. The free parameters σ_0, x_0 and λ which are subject to be found are same as for the previous dipole model.

2.4.5 BGK dipole model

The BGK dipole model (also known as B-SAT) [44] proposed by J.Bartels, K. Golec-Biernat and H. Kowalski modifies the original GBW dipole model [40] by including the DGLAP evolution. The evolution is introduced by the modification of the small r behavior of the dipole cross section by incorporating the properly evolved gluon distribution. The small size r of the dipole corresponds to large values of Q^2. As a result, the saturation for low Q^2 and for the transition region is remained as it was modeled by the original GBW.

In the BGK model, the dipole cross section is given by the modified formula (64)

$$\sigma(x, r^2) = \sigma_0 \left(1 - \exp\left[-\frac{\pi^2 r^2 \alpha_s(\mu_F^2) x g(x, \mu_F^2)}{3\sigma_0}\right]\right), \tag{67}$$

where the factorization scale μ_F^2 has the form

$$\mu_F^2 = \frac{C_{BGK}}{r^2} + \mu_0^2. \tag{68}$$

The gluon distribution $g(x, \mu_F^2)$ is evolved according to the DGLAP evolution assuming the gluon dominance and neglecting quarks in the evolution equations. At some starting scale μ_0^2 the gluon density is parametrized as

$$x g(x, \mu_0^2) = A_g x^{B_g} (1 - x)^{C_g}. \tag{69}$$

The fitted parameters for this model are divided into two parts. The parameters of the gluon distribution, A_g, B_g, C_g, are firstly fitted for obtaining a proper gluon distribution. Then the parameters of the dipole model itself, σ_0, C_{BGK}, μ_0^2 are fitted taken the gluon density to be fixed.

2.5 DGLAP fits

The PDFs are determined from perturbative QCD fits to different experimental data, in particular to the DIS cross section data. The fits are based on the DGLAP evolution equations which allow a comparison of the theory predictions, calculated at different values of invariant mass squared Q^2, to data. The PDFs as functions of x are parametrized at some starting scale and then evolved according to the DGLAP evolution equations. The evolved PDFs are used for calculation of the structure function by convoluting the PDFs with the coefficient functions. The obtained structure functions and consequently the DIS cross sections are fitted to data by minimizing a

χ^2-function. The fit procedure is implemented in the HERAFitter program [45], which performs the minimization of the χ^2-function using MINUIT package [46].

In the following, the HERAPDF QCD fit [47] based on the inclusive DIS data is under consideration.

2.5.1 HERAPDF fits

The initial conditions for the HERAPDF QCD fit are as follows. The starting scale is chosen to be below the charm mass threshold $m_c^2 > Q_0^2 = 1.9$ GeV^2. The fitted PDFs $xf(x)$ are $xu_v(x)$, $xd_v(x)$, $xg(x)$, $x\overline{U}(x)$, $x\overline{D}(x)$, where at the starting scale $x\overline{U}(x) = x\bar{u}(x)$, $x\overline{D}(x) = x\bar{d}(x) + x\bar{s}(x)$ and (29) $xs(x) = x\bar{s}(x)$ is assumed. The parton distributions are parametrized at the starting scale Q_0^2 using the following generic form:

$$xf(x) = A_q\, x^{B_q}\,(1-x)^{C_q}\,(1 + D_q x + E_q x^2). \tag{70}$$

The certain number of parameters depends on the physical sense, fit quality, and the applied additional constrains.

The HERAPDF1.0 fit [47] has 10 parameters corresponding to the following parametrization choices:

$$\begin{aligned}
xg(x) &= A_g\, x^{B_g}\,(1-x)^{C_g}, \\
xu_v(x) &= A_{u_v}\, x^{B_{u_v}}\,(1-x)^{C_{u_v}}(1 + E_{u_v} x^2), \\
xd_v(x) &= A_{d_v}\, x^{B_{d_v}}\,(1-x)^{C_{d_v}}, \\
x\overline{U}(x) &= A_{\overline{U}}\, x^{B_{\overline{U}}}\,(1-x)^{C_{\overline{U}}}, \\
x\overline{D}(x) &= A_{\overline{D}}\, x^{B_{\overline{D}}}\,(1-x)^{C_{\overline{D}}}.
\end{aligned} \tag{71}$$

The normalization parameters A_{u_v}, A_{d_v}, A_g are constrained by the quark number and momentum sum rules (30-32). The condition $x\bar{u} \to x\bar{d}$ as $x \to 0$ is satisfied by the requirement $B_{\overline{U}} = B_{\overline{D}}$ and constraint $A_{\overline{U}} = (1 - f_s)A_{\overline{D}}$, where $f_s = 0.31$ is a fraction of the strange contribution. The latter is expressed as x independent fraction of $x\overline{D}$: $x\bar{s} = f_s x\overline{D}$, because the HERA data have no sensitivity to constrain the strange density. The condition $B_{u_v} = B_{d_v}$ is also applied. The following published HERAPDF1.5 QCD fits [48] have increased number of parameters, which originate from the modified flexible gluon parametrization [49]

$$xg(x) = A_g\, x^{B_g}\,(1-x)^{C_g} - A'_g\, x^{B'_g}\,(1-x)^{25} \tag{72}$$

and are presented in the Table 2.

The PDFs are evolved using DGLAP evolution equations (50) at NLO [50] and NNLO [51] in the $\overline{\text{MS}}$ scheme [30]. The renormalization and factorization scales are chosen equal to Q^2, and the strong coupling $\alpha_s(M_Z) = 0.1176$ is taken to be constant, though it can also be a fitted parameter. The QCD predictions for the structure functions are obtained by convoluting the

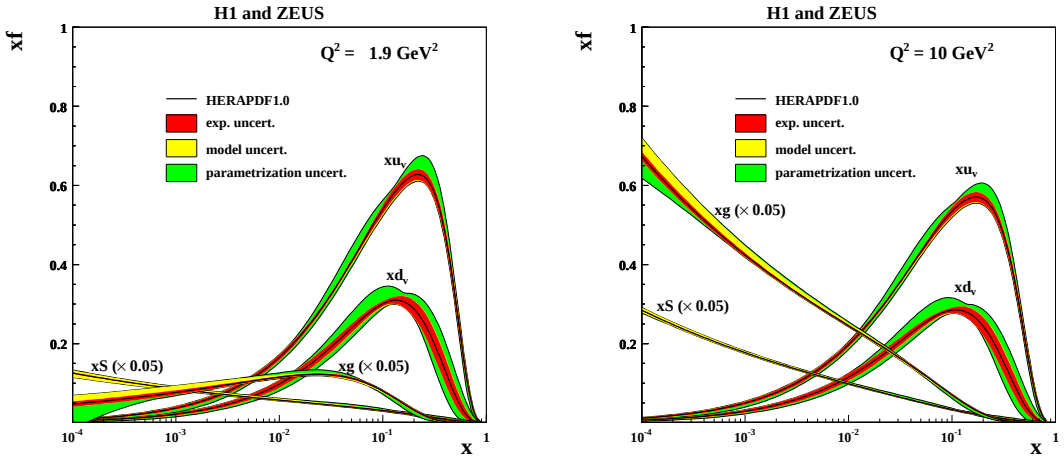

Figure 11: The parton distributions as determined by the HERAPDF1.0 QCD fit [47] at $Q^2 = 1.9\text{GeV}^2$ and $Q^2 = 10.0\text{GeV}^2$. The gluon and sea distributions are scaled down by a factor of 20. The experimental, model and parametrization uncertainties are shown separately.

PDFs with the coefficient functions, which are calculated using the ACOT [52] and RT [53] heavy flavour schemes.

In the fit, the correlations induced by systematic uncertainties are properly taken into account. Besides the experimental uncertainties, model and parametrization uncertainties are determined by varying model inputs and parameters of (70). The model uncertainties are obtained by a variation of the minimum cut Q^2_{min}, the charm and beauty mass parameters, and the strangeness fraction. The parametrization uncertainties are estimated by including additional parameters into the functional form (70) and by varying the starting scale Q^2_0.

HERAPDF	D_{u_v}	E_{u_v}	A'_g	B'_g	B_{u_v}	Number of parameters
1.0	0	free	0	0	$B_{u_v} = B_{d_v}$	10
1.5	0	free	0	0	$B_{u_v} = B_{d_v}$	10
1.6	free	free	free	free	free	14
1.7	0	free	free	free	free	13

Table 2: Parametrization choices for each version of the NLO HERAPDF QCD fit [48]. Mark *free* means that the parameter is fitted in the corresponding version of the QCD fit.

2.5.2 Fit results

The fitted PDFs as determined by the HERAPDF1.0 fit are shown in Figure 11. The distributions $xu_v(x)$, $xd_v(x)$, $xg(x)$, $xS(x)$, where $xS(x) = 2x(\overline{U}(x) + x\overline{D}(x))$, are presented at $Q^2 = 1.9\,\text{GeV}^2$ and $Q^2 = 10\,\text{GeV}^2$. The gluon and sea distributions are scaled down by the factor 20. The experimental, parametrization and model uncertainties are shown separately.

The fit results illustrate the crucial influence of the DGLAP evolution on the gluon and sea

densities. At $Q_0^2 = 1.9\,\mathrm{GeV}^2$ the sea density $xS(x)$ rises towards low x, whereas the gluon distribution which has a valence quark-like shape. The Q^2 evolution dramatically changes the low-x behavior of the gluon distribution $xg(x)$, which starts to rise similar to the sea quark distribution towards low x.

It is clearly seen in Figure 11 that the gluon and sea distributions dominate in the region $x < 0.01$. Nevertheless, the valence quark distributions are also nonzero in this region. For example, at $Q^2 = 10\,\mathrm{GeV}^2$ and $x = 0.01$ the valence contribution is about 5% and exceeds the magnitude of the PDFs uncertainties. Therefore, the valence quark distributions provide a sizable contribution to the scattering cross section and should be properly taken into account in the fits to low-x data.

2.6 Dipole fits

The dipole models are fitted to low-x inclusive NC cross section data from HERA and the fitted models provide predictions for the structure functions according to (21). In this low-x region, $x < 0.01$, the valence quark contribution had been assumed to be negligible. Now, the recent HERA data make it possible to estimate the valence PDFs in this region (see Figure 11).

The account of the valence contribution to the DIS cross section is performed using the HERAFitter program [45]. The GBW, IIM and BGK dipole models have been implemented in this package and can be used for fitting the data.

In the HERAFitter, the predictions for the DIS cross sections obtained using GBW and IIM dipole models can be directly compared to data. The package also allows to improve the dipole model predictions by adding the valence quark contributions which are estimated using the DGLAP formalism.

For the BGK dipole model, the DGLAP evolution of the gluon distribution which originally considered the gluon density only (69), has been improved by taking into account the coupled DGLAP evolution of the gluon and sea quark densities. The DGLAP evolution within the HERAFitter framework is performed using QCDNUM [54] package. The obtained gluon distribution is used in the BGK dipole model (67). The valence contribution obtained from PDF fits can be also added to the dipole model prediction for the cross section.

3 The HERA collider

The *Hadron-Elektron Ring Anlage* (HERA) at *Deutsches Elektronen-Synchrotron* (DESY) in Hamburg was the first and the only electron-proton high-energy particle collider in the world. It was situated underground in approximately a circular tunnel of 6.3 km circumference.

The HERA collider started the operation in October 1991 and the last beam was launched in June 2007. The collider was equipped with four detectors. Two of them, multipurpose H1 and ZEUS detectors operated from 1991 and were measuring the interaction between colliding beams to probe the structure of the proton, study the fundamental interactions between particles and search for new physics beyond the Standard Model. The first ep collision has been registered by the H1 detector on October 19, 1991 [55], while the first candidate for the DIS event has been obtained only in June 1992. The data taking started in 1992 and continued until the end of HERA operation in 2007 with a break for the upgrade in 2000–2002. Two other fix-target detectors, HERMES and HERA-B operated from 1995 and from 1998, respectively. The HERMES experiment was devoted to investigation of the spin structure of nucleus and used the polarized lepton beam with a polarized gas as a target, whereas at HERA-B the proton beam collided with a stationary wire target to study the CP violation in the decay of B-mesons.

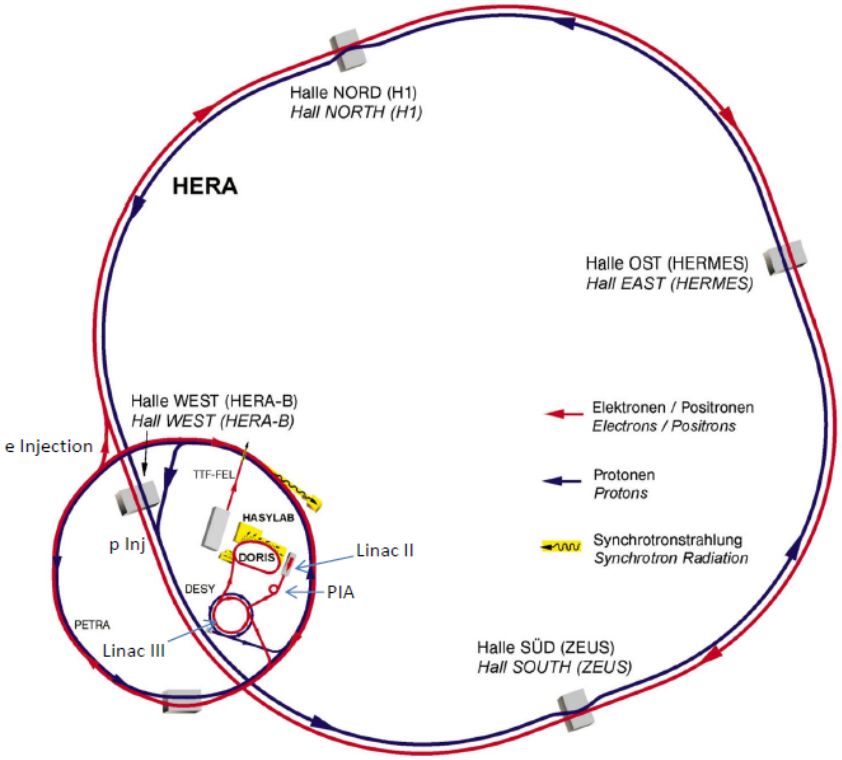

Figure 12: A schematic view of the HERA ring and the preaccelerator facilities [56].

The most important design parameters of a particle accelerator are the maximum energy and luminosity that can be achieved. The high energy of colliding particles is reached by a

composite system of accelerators. A schematic view of the HERA ring [56] and the preaccelerator facilities is presented in Figure 12. Before injection into HERA, the electrons and protons were preaccelerated by a system of accelerators. Separate linear accelerators and synchrotrons of 100 m diameter have been used for acceleration of particles of each type. Next, electrons and protons proceeded to the storage ring *Positron-Elektron-Ring-Anlage* (PETRA), which has been used to accelerate the particles to their injection energies of 14 GeV and 40 GeV, respectively. After injection into HERA, the beam particles were stored in bunches separated by a distance of 28.8 m, corresponding to a bunch crossing time of 96 ns. In HERA ring, electrons have been accelerated to a final energy of $E_e = 27.6$ GeV and protons — to a final energy of $E_p = 820$ GeV. In 1999 the proton energy has been increased up to $E_p = 920$ GeV, resulting in a center of mass energy $\sqrt{s} = \sqrt{4E_eE_p} \approx 319$ GeV. To keep the protons at such energies on the circular orbit superconducting magnets with a magnetic field of 4.65 T were used, whereas the electrons were controlled by conventional magnets with a magnetic field of 0.165 T.

Along with the reached high energies of accelerated particles, the performance of a collider considerably depends on the instantaneous luminosity L. It is defined as the number of reaction events produced per unit reaction cross section per unit of time. For the storage ring ep collider with the Gaussian bunches colliding periodically the instantaneous luminosity is given as [57]:

$$L = \frac{fN_eN_p}{4\pi\sigma_x\sigma_y} \ [\mathrm{cm}^{-2}\ \mathrm{s}^{-1}], \tag{73}$$

where N_e, N_p are numbers of electrons and protons in each bunch, σ_x and σ_y denote the Gaussian transverse beam profiles in horizontal and vertical directions and f is the revolution frequency. The maximum instantaneous luminosity achieved at HERA was about [58] 5×10^{31} cm^{-2} s^{-1}. The integrated luminosity is defined as

$$\mathcal{L} = \int L\ dt = \frac{N}{\sigma}, \tag{74}$$

where N is a number of detected events and σ is an interaction cross section for a given process. The integrated luminosity as collected by the H1 detector during HERA I and HERA II operation periods is presented in Figure 13. The total integrated luminosity of HERA I data taking period as collected by H1 detector is about 130 pb^{-1}. The HERA upgrade made it possible to increase the luminosity by a factor of five by introducing new superconducting focusing magnets immediately inside the H1 and ZEUS detectors and thus compressing the spot size of the proton beam at the interaction point (HERA II period). In last months of operation the proton beam was accelerated to the reduced energies of $E_p = 460$ GeV and $E_p = 575$ GeV to perform measurements of the longitudinal proton structure function F_L. The integrated luminosity obtained for these periods by H1 detector is [84] 12.2 pb^{-1} and 5.9 pb^{-1}, respectively. These periods are shown by the green line in Figure 13. The total integrated luminosity delivered during HERA I

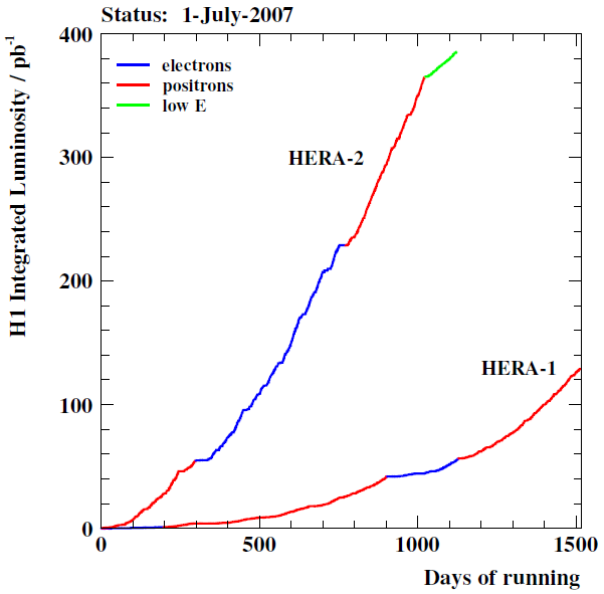

Figure 13: The integrated luminosity as collected by the H1 detector during HERA I (1993–2000) and HERA II (2003–2007) operation periods. The green line indicates the period of operation with the reduced proton energy of E_p = 460 GeV and E_p = 575 GeV.

and HERA II operation periods is approximately [58] 800 pb^{-1}.

3.1 H1 detector

The H1 detector is a multipurpose detector with almost 4π hermetic coverage. It has been located in the experimental Hall NORD and had roughly the dimensions 12 m × 10 m × 15 m (length×width×height) with a weight of approximately 2800 tons. A schematic view of the H1 detector is shown in Figure 14.

In H1 a right-handed orthogonal coordinate system with the origin in the nominal interaction point is used. The positive z-axis direction is chosen along the proton beam direction and the positive x-axis direction points to the center of the HERA ring. The detector is cylindrically symmetrical around the beam pipe and the natural spherical coordinate system (r, θ, ϕ) is also used. In this system the polar angle θ of the proton beam, measured with respect to the z-axis, is 0° (forward direction) and of the electron beam is 180° (backward direction). The azimuthal angle ϕ is measured with respect to the x-axis. Due to the asymmetric beam energies the center-of-mass is boosted along the forward direction. As a result, the H1 detector is significantly more massive and segmented there.

The H1 detector consists of multiple subdetectors which are installed around the interaction point in several layers. The innermost detectors are the Central and Forward Tracking Detectors (CTD, FTD), measuring tracks and consisting of silicon tracking detectors, drift and proportional chambers. The CTD and FTD are shown in Figure 15. In the central and forward

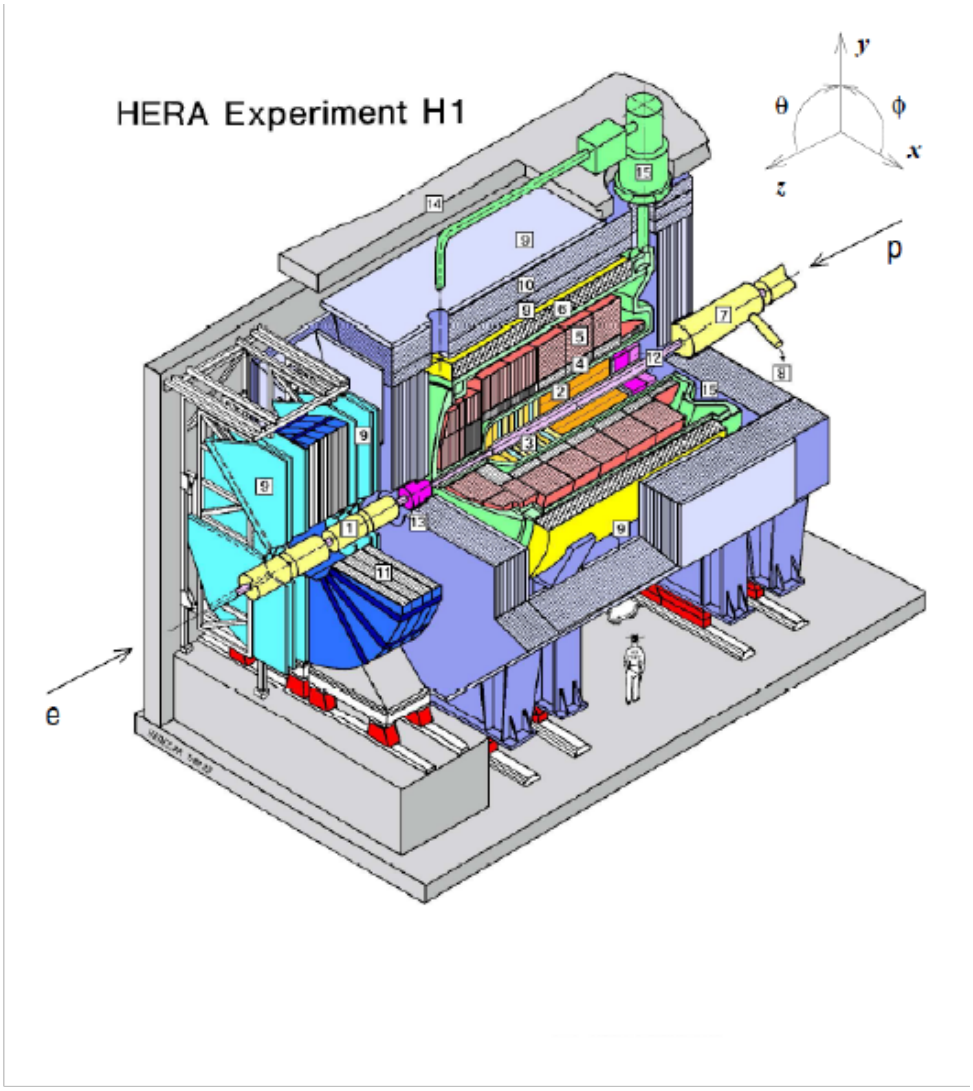

Figure 14: A schematic view of the H1 detector. The noted components are Beam pipe and beam magnets (1); Central tracking chambers (2); Forward tracking and transition radiators (3); Liquid Argon: Electromagnetic calorimeter (lead) (4), Hadronic Calorimeter (stainless steel) (5); Superconducting coil (6); Compensating magnet (7); Helium cryogenics (8); Muon chambers (9); Instrumented Iron (10); Muon forward magnet (11); SpaCal (12); PLUG calorimeter (13); Concrete shielding (14); Liquid Argon cryostat (15).

region the tracking detectors are enclosed by a cryostat vessel containing the finely segmented Liquid-Argon Calorimeter (LAr) [61]. The cryostat vessel is surrounded by a superconducting coil, providing an axial magnetic field of 1.15 T. The Backward Proportional Chamber (BPC) and Spaghetti Calorimeter (SpaCal) [62] are located in the backward region. The LAr calorimeter and SpaCal comprise of the electromagnetic and hadronic sections. The instrumented iron return yoke of the magnet is used to measure muons and small fractions of hadronic showers leaking out of the LAr calorimeter. Additional chambers inside and outside of the iron yoke are installed to improve muon identification. The Forward Muon Detector (FMD) is used for

an independent measurement of highly energetic muons in the forward direction. The PLUG scintillation detector surrounds the forward beam pipe hole of the LAr calorimeter. Further in the electron direction the Photon Detector (PD) is installed to measure photons from the Bethe-Heitler process to determine the luminosity. In the same direction the Electron Tagger (ET) is used to detect scattered electrons under very small angles.

In the following, a brief overview of the main subdetectors for the HERA II configuration is given. A detailed description of the H1 detector and its subsystems can be found in [59,60].

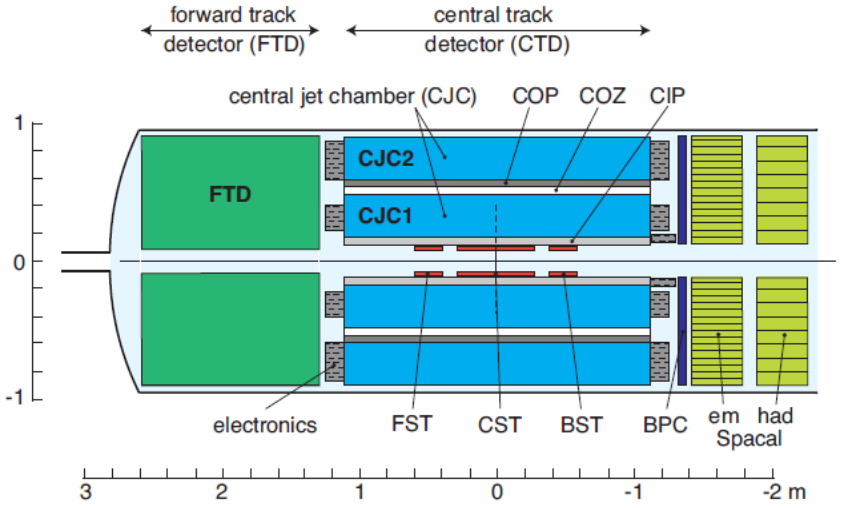

Figure 15: Schematic cross-sectional view of the H1 tracking system.

3.1.1 Tracking detectors

3.1.1.1 The Central Tracking Detector

The Central Tracking Detector (CTD) consists of two Central Jet drift Chambers (CJC1 and CJC2), the z drift chamber [63], the Central Inner Proportional chamber (CIP) [64], the Central Outer Proportional chamber (COP), and three Silicon Trackers (Forward (FST), Central (CST) [65] and Backward (BST) [66]). The $r\phi$ (radial) view of the CTD is shown in Figure 16. The drift chambers and the silicon trackers are used for measurement of tracks from the hadronic final state and to determine the interaction vertex. The COP and CIP are used mainly for triggering purposes.

The Central Jet Chambers (CJC) are two concentric drift chambers which cover an angular range $15^\circ < \theta < 165^\circ$ in the polar angle with full coverage in the azimuth. The CJC1 consists of 30 drift cells with 24 anode sense wires each, while the CJC2 comprises 60 drift cells with 32 sense wires each. The sense wires strung parallel to the beam axis and magnetic field direction. The drift cells are inclined at about 30° with respect to the radial direction, such that

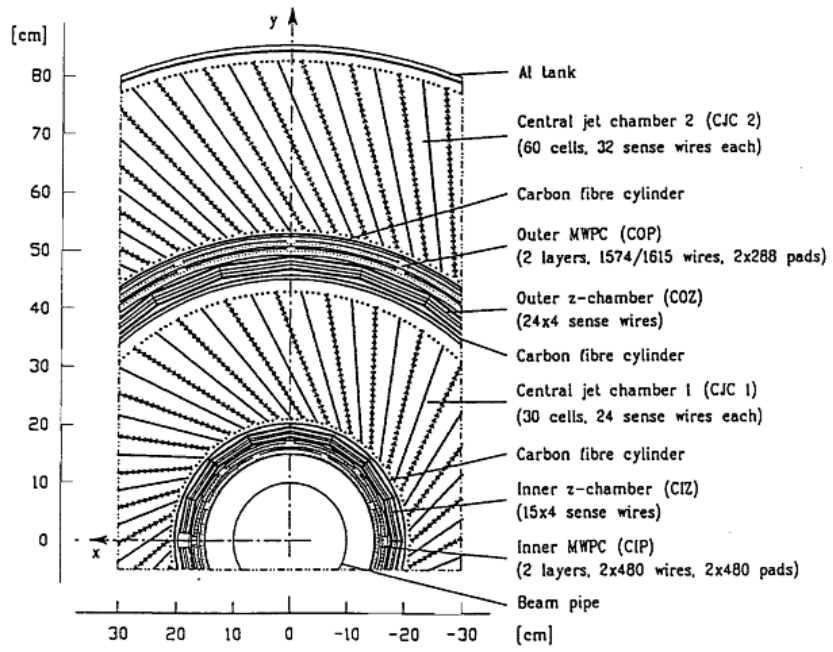

Figure 16: The $r\phi$ view of the H1 Central Tracking Detector.

the drift direction of ionization electrons from a stiff high momentum tracks is approximately perpendicular to the wire plane. This makes it possible to obtain optimum track resolution and to resolve usual drift chamber ambiguity by connecting track segments of different cells. A high p_T track crosses the sense wire plane at least once in the CJC1 and CJC2. From the match at the crossing, the passing time of a particle can be determined to a precision of 0.5 ns. This allows an easy separation of tracks from different bunch crossings. The charge deposits are read out from both ends of each wire, providing particle identification via ionization loss and an approximate determination of the z-coordinate via the charged asymmetry between two wire end signals. The drift time and wire signal propagation time measurements impose the spatial resolution of $\sigma_{r\phi} \approx 170\ \mu$m and $\sigma_z \approx 22$ mm.

The Central Outer z-Chamber (COZ) surrounds externally the CJC1 and is used to measure the z-coordinate and additionally the ϕ-coordinate. The chamber has a polar angle coverage of $25^\circ < \theta < 156^\circ$. Its sense wires are strung perpendicular to the beam resulting in a drift direction along the beam axis. This allows measurement of the z-coordinate with a better accuracy than using the charge division. The spatial resolution of the COZ is $\sigma_{r\phi} \approx 58$ mm and $\sigma_z \approx 300\ \mu$m.

The Central Inner Proportional chamber (CIP) is a five layer multiwire proportional chamber installed inside of the CJC1. It covers the largest angular range $5^\circ < \theta < 175^\circ$ in the polar angle. The Central Outer Proportional chamber (COP) is a two layer multiwire proportional chamber which is located between the CJC1 and CJC2. The chambers are used together to identify tracks pointing to the interaction vertex and thus to reduce background at the trigger level. The noise

level in COP is slightly higher due to more difficult grounding comparing with the CIP. Because of this, the efficiencies of the chambers are about 99% and 92% for CIP and COP, respectively. During the HERA upgrade the CIP performance has been increased and the COP became less important.

The Silicon Tracking Detector [65] consists of three individual components. The Central Silicon Tracker (CST) is the closest to the interaction point tracking detector. It provides vertex information from precision measurements of charged particles. It surrounds directly the beam and consists of two concentric cylindrical layers of silicon sensors with two-coordinate readout allowing the identification of heavy-flavour particles with decay lengths of a few hundred micrometers. A point resolutions of 12 μm for the radial direction and 22 μm for the z-direction is achieved by the CST. That produces an impact parameter resolution of 37 μm for high momentum tracks with an angular coverage of $30^\circ < \theta < 150^\circ$.

The Backward Silicon Tracker (BST) [66] and Forward Silicon Tracker (FST) [68] are used to extend the angular coverage of the CST into the backward and forward direction, respectively. The BST polar angle acceptance is from 165° to 176°, whereas the FST covers the angular region of $7^\circ < \theta < 19^\circ$. The BST in the configuration installed in 1999 [66] is schematically shown in Figure 17. It consists of eight planes (disks) and 16 azimuthal sectors. The planes are mounted perpendicularly to the beam axis and arranged in two modules, BST1 and BST2, of four planes each. A first version of the BST with four planes is described in [67]. Each BST plane is equipped with 16 wedge shaped, single sided, double metal, silicon strip sensors of 250 μm thickness. Each sensor contains 640 sensitive p strips which are concentric around the beam axis with a pitch of 96 μm. The signals are amplified and temporarily stored by five on-detector front-end chips until a readout instruction is received. Using these *r sensors* the track polar angle can be determined. In addition to the r sensors, each plane contains one single sided, single metal, silicon strip sensor in the azimuthal sector $45^\circ < \phi < 67.5^\circ$ mounted behind the r sensor. This u sensor has 640 sensitive strips parallel to the reference edge of the sensor with a pitch of 75 μm. It thus measures hits in u coordinate space defined by $u = r \sin \phi_u$, where ϕ_u is the azimuthal angle with respect to the reference edge of the sensor. Combining the information from r and u sensors, it is possible to measure the transverse momentum and determine the charge of a track in the BST. This feature is used in some analyses [69] to cross check the simulation of the photoproduction background. During data taking an online hit finding is performed. This takes into account individual pedestals of each channel, which are dynamically updated. Coherent shifts in the amplitude of groups of strips, so called *common mode*, are also corrected for. For reconstructed tracks, the most probable signal-to-noise values for the hits are about 15 for the r sensors and 30 for the u sensors. The single hit resolution is 20 (15) μm for the r (u) coordinate.

The Backward Proportional Chamber is installed in front of the SpaCal and covers polar angles of $155.5^\circ < \theta < 174.5^\circ$. The chamber consists of the four differently oriented anode

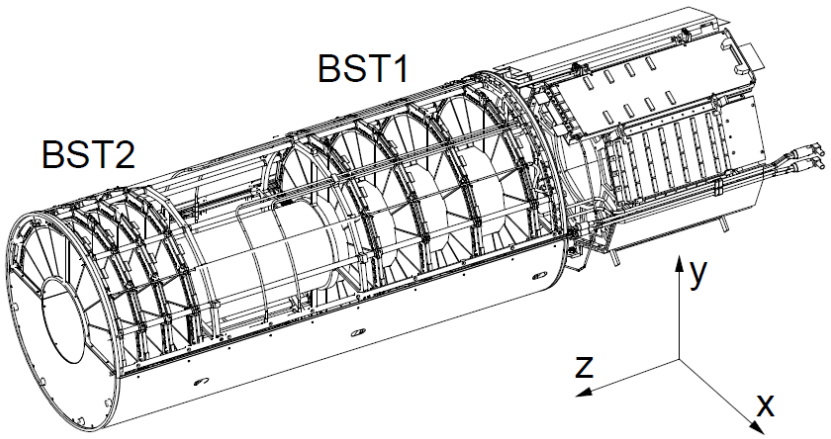

Figure 17: A schematic layout of the H1 Backward Silicon Tracker [66]. The active area consists of eight wheels subdivided into two modules, BST1 and BST2, of four wheel each. One wheel is made of 16 *r* sensors and one *u* sensor which is on the back side and not shown here.

wire planes of the backward chamber and is used to improve the position measurement of the scattered electrons in the backward direction.

3.1.1.2 The Forward Tracking Detector

The Forward Tracking Detector (FTD) is installed in front of the CTD and provides an accurate measurement of tracks in the forward direction, covering the angular region of $7^\circ < \theta < 25^\circ$. The FTD consists of three supermodules, each containing three planar drift chambers and one or two radial. Each planar one has four parallel wires, whereas the radial one has eight wires radiating outwards from the beam pipe. Nevertheless, all wires are strung perpendicular to the beam direction. The momentum resolution σ_p/p^2 is below than 0.003 GeV^{-1} and track angular resolution is $\sigma_{\theta,\phi} < 1$ mrad. The achieved single hit resolution is about $\sigma_{x,y} \sim 210$ μm with radial resolution of approximately $\sigma_r \sim 30$ mm. The track finding efficiency is about 70% in each supermodule.

3.1.2 Calorimeters

3.1.2.1 The Liquid Argon Calorimeter

The Liquid Argon calorimeter (LAr) [60] is designed to provide a clear identification and measurement of electron's energy as well as a good hadronic energy measurement. The liquid argon technique is chosen because of a good stability and facile calibration, fine granularity for energy flow measurements and a homogeneity of response. It has an angular coverage

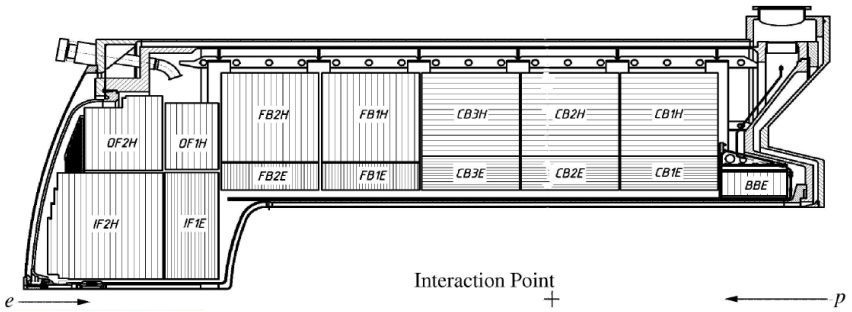

Figure 18: Schematic view of eight calorimeter wheels of the Liquid Argon calorimeter [60].

of $4^\circ < \theta < 154^\circ$ in the polar angle and full coverage in the azimuth. The calorimeter is installed inside a single cryostat and, to keep the amount of dead material as small as possible, the superconducting solenoid surrounds the LAr vessel. The calorimeter is segmented along the z-direction into eight calorimeter wheels as shown in Figure 18: the Inner Forward (IF), Outer Forward (OF), Forward Barrel (FB) 1 and 2, Central Barrel (CB) 1,2 and 3 and the Backward Barrel(BBE). Each wheel is divided in azimuth into 8 modules (octants) in the barrel and into 2 modules in the forward region. The modules are divided into inner, electromagnetic stack with lead absorber plates (20–30 radiation lengths) and an outer, hadronic stack made of stainless steel absorber plates. They are denoted by letters E or H behind the name of the electromagnetic or hadronic stack in the Figure 18. The LAr calorimeter is highly segmented in both the electromagnetic and hadronic sections of the modules with a total amount of around 45000 geometric cells. The electromagnetic stack has 3 or 4 fold longitudinal segments while hadronic one has 4 to 6 longitudinal ones. The hadronic energy resolution, as determined in test beam measurements [71], is

$$\frac{\sigma_E}{E} \approx \frac{50\%}{\sqrt{E/(\mathrm{GeV})}} \oplus 2\%, \tag{75}$$

where the symbol $\oplus$ indicates that the terms are added in quadrature.

3.1.2.2 The Spaghetti Calorimeter

The so-called Spaghetti Calorimeter (SpaCal) [62] is a lead/scintillating-fibre calorimeter which is located in the backward direction behind the CTD (see Figure 19). It is designed for a precise measurement of the energy and polar angle of electrons scattered into the backward region, covering the polar angular range of $153^\circ < \theta < 177.5^\circ$.

The SpaCal consists of two separate sections, an inner electromagnetic and an outer hadronic section. Both sections have lead as absorber and plastic scintillating fibres as active material. The calorimeter has got his name from the long and thin fibres ('spaghettis') which are aligned parallel to the beam direction and embedded in a lead matrix. The unit cell with fibers is shown

in Figure 20.

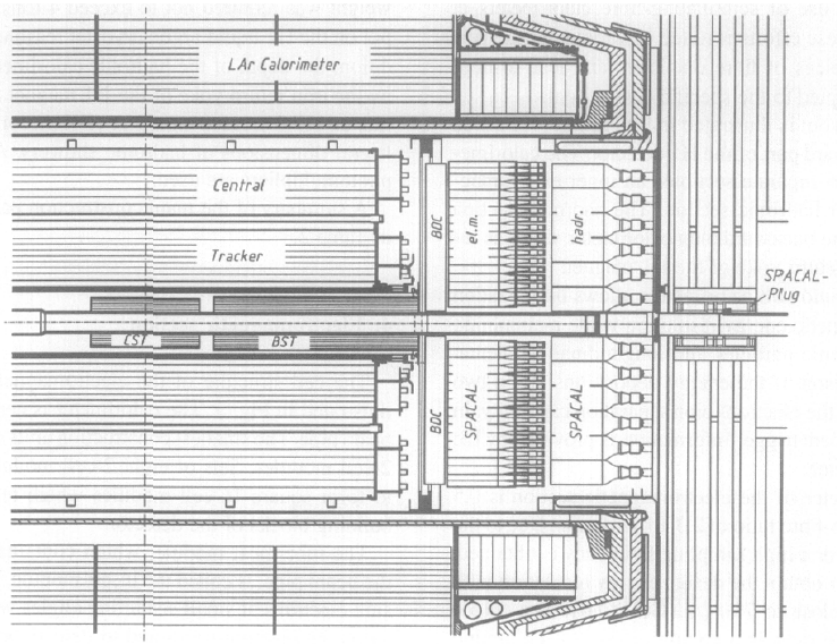

Figure 19: Partial view of the H1 detector showing the position of the lead/scintillating-fibre calorimeter (SpaCal) [62]. The Backward Silicon Tracker (BST) [66] is also shown.

The scintillations in the plastic fibres are produced by particles, interacting with the lead absorber. The scintillation light is conducted by the fibres and collected by photomultiplier tubes which convert the light into electric signals. The fibres of the electromagnetic section have a diameter of 0.5 mm and a lead-to-fibre ratio of 2.3 : 1 by volume. A small fibre diameter makes it possible to obtain a high sampling frequency which is resulted in design electromagnetic energy resolution of

$$\frac{\sigma_{em}}{E} \approx \frac{7\%}{\sqrt{E/(\mathrm{GeV})}} \oplus 1\%. \tag{76}$$

The angular resolution of 2 mrad and a position resolution of a few millimeters are achieved by the high granularity of the calorimeter. The photomultiplier tubes provide a time resolution of about 1 ns allowing to reduce the non-ep background on the trigger level. The active volume is 250 mm long, corresponding to 28 radiation lengths. The hadronic section of the SpaCal consists of fibres with a diameter of 1 mm and lead-to-fibre ratio of 3.4 : 1. The hadronic calorimeter section adds one interaction length of material to the electromagnetic section, which is one interaction lengths deep. The hadronic energy response is investigated in the energy range of $1 - 7$ GeV [72]. It is obtained that an energy resolution is $\sigma_{had}/E \sim 38\%$ within a depth of one interaction length and $\sigma_{had}/E \sim 29\%$ for a total depth of two interaction lengths.

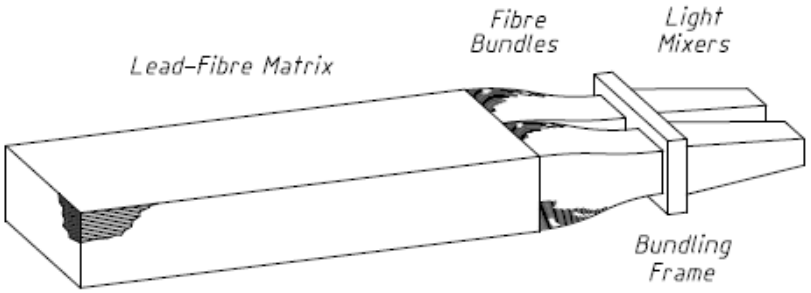

Figure 20: Schematic view of the lead/fibre matrix of the lead/scintillating-fibre calorimeter (SpaCal) [62].

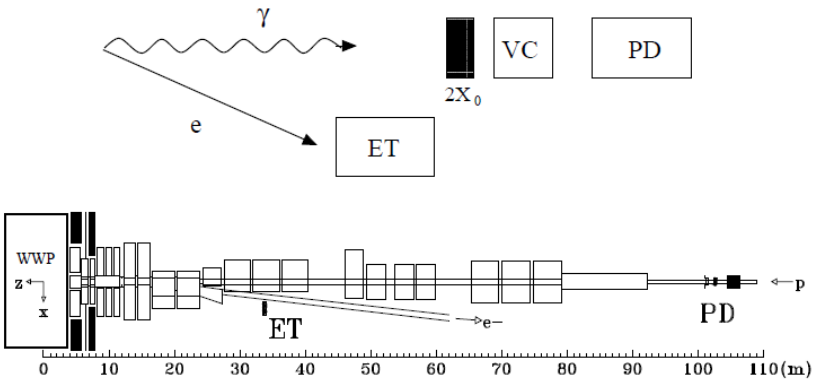

Figure 21: A schematic view of the luminosity system.

3.1.3 The Luminosity system

At HERA I, the instantaneous luminosity is measured from the rate of bremsstrahlung (Bethe-Heitler) events [73] $ep \to ep\gamma$ in virtue of large and precisely known total cross section for this process. The moderate background from the residual gas in the beam pipe, $eA \to eA\gamma$, is also easily subtracted by the data from electron pilot bunches. The luminosity is calculated as

$$L = \frac{R_{tot} - (I_{tot}/I_0)R_0}{\sigma_{vis}}. \tag{77}$$

where R_{tot} is the total rate of bremsstrahlung events, R_0 is the rate in the electron pilot bunches, I_{tot} and I_0 are the corresponding electron beam currents. σ_{vis} is the visible part of the bremsstrahlung cross section, taking the detector acceptance and trigger efficiency into account.

The luminosity is determined using a detection of scattered electrons by the Electron Tagger (ET) and outgoing photons by the Photon Detector (PD). Since the angular distributions for both the electrons and photons are strongly peaked in the direction of primary electron beam – at 27.6 GeV planar angle are of the order of $\theta \sim O(m/E) \sim 17$ μrad – the detectors have to be placed close to the beamline and far away from the interaction point in order to cover these

Parameter	Electron Tagger	Photon Detector
Energy interval $E_\gamma/E_e = 1 - E_{e'}/E_e$	0.2 – 0.8	0.004 – 1.0
Polar angle acceptance (mrad)	0 – 5	0 – 0.45
Average acceptance for $ep \to ep\gamma$ (%)	48	98
Average acceptance for photoproduction (%)	36	–
σ_{vis} (mb)	28	174
Aperture $x \times y$ (mm^2)	154×154	100×100
Expected values for designed luminosity		
$ep \to ep\gamma$ rate for $E > E_{thr} = 4$ GeV (MHz)	0.4	1.3
Photoproduction event rate (Hz)	20 – 30	–
Reached values at HERA		
Energy resolution σ_E/E (%)	$1 \oplus 10/\sqrt{E/(\mathrm{GeV})}$	
Position resolution $\sigma_{x,y}$ (mm)	0.3 – 1.2	
Time resolution σ_t (ns)	< 3	

Table 3: Some parameters of the luminosity system.

small angles.

The general view of the luminosity system is presented in Figure 21. Scattered electrons are deflected by a set of low-beta quadrupoles and a bending magnet located in the region 5.8 m $< -z <$ 23.8 m, pass an exit window at $-z = 27.3$ m and hit the ET at $-z = 33.4$ m. The photons leave the proton beam pipe through a window at $-z = 92.3$ m, where the beam pipe bends upward, and hit the PD at $-z = 102.9$ m. A Pb filter (two radiation lengths) followed by a water Cherenkov (one radiation length) Veto Counter (VC) protects the detector from the high synchrotron radiation flux. From the p-beam side the PD is shielded by an iron wall of 2 m thickness. The VC eliminates events with photons interacting in the filter. Both the ET and PD can be remotely moved from the median plane of the e-beam during injection. This operation can be reversed within 1–2 min with a position accuracy of 100 μm.

The acceptance of the luminosity system for nominal electron beam conditions (E_e = 27.6 GeV, zero tilt) and the expected rates at the design luminosity of $1.5 \times 10^{31}\mathrm{cm}^{-2}\mathrm{s}^{-1}$ are given in Table 3. One of the main contributions to the systematic error in the absolute luminosity measurement comes from the dependence of the system acceptance on possible variations of the electron beam angle in the interaction region. This tilt, typically of the order of 100 μrad, is controlled by the position of the beam profile at the PD with high precision, of the order of 10 μrad. The corresponding corrections to σ_{vis} are taken into account already online and can be further improved during the offline analysis.

Despite the very large cross section of the bremsstrahlung process which makes it possible to achieve negligible statistical uncertainties for small amounts of measured integrated luminosity, there are various sources of possibly large systematic uncertainties. For example, they can originate from the synchrotron radiation emitted by the electron beam as it passes the focusing

magnets surrounding the interaction region. Also, there may be inevitable acceptance limitations for the small angle detectors, caused by elements of the beam transport system which separates the bremsstrahlung photons and electrons from the circulating proton and electron beams. Therefore, at HERA II the integrated luminosity is determined using QED Compton events which are measured in the H1 main detector. In this method the luminosity is calculated using the relation [74]

$$\mathcal{L}^{\mathrm{QEDC}} = \frac{N - N_{\mathrm{bgr}}}{\epsilon N_{\mathrm{MC}}} \mathcal{L}_{\mathrm{MC}}. \tag{78}$$

Here N is a number of selected QEDC candidate events, N_{bgr} is a number of selected background events, N_{MC} is a number of Monte Carlo simulated events passing the same event criteria as the detected events, ϵ is the efficiency of selection, and $\mathcal{L}_{\mathrm{MC}}$ is the luminosity corresponding to the simulated events.

3.1.4 Trigger system

The trigger system is designed to select out the signals from the desired physics events and to suppress ones from background events as efficiently as possible. The usual rate of all events produced in the H1 detector reaches the order of tens kHz and the most of them are background which mainly originates from electron- and proton-gas collisions. The requirement to the trigger system is to efficiently reject background events in a such way that *ep* collisions can be recorded with a frequency of $\sim$ 50 Hz, which is the limit of the output bandwidth. Moreover, since the readout time is much longer than the bunch crossing interval, 96 ns, the *dead-time* of the trigger system should be also reduced. To achieve these requirements, the four level (L1-L4) trigger system is used in H1. Each of these levels has an independent delay from 2.3 μs for L1 up to 100 ms for L4. These levels are shown in Figure 22.

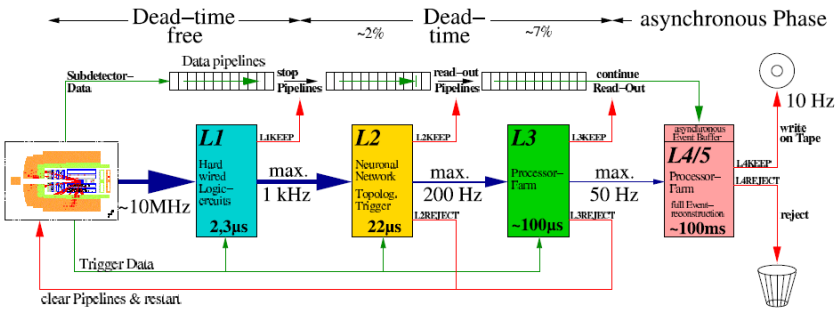

Figure 22: The H1 four-level trigger system.

The First Trigger Level (L1) decision is based on the information from 128 subtriggers. These subtriggers collect the reconstruction information from the subdetector trigger systems. Not every subdetector can provide a prompt reconstruction of the event, so subtrigger decisions are stored in a cyclic buffer, or *pipe-line*. The central trigger logic decides to keep an event,

if the event fulfills conditions of at least one subtrigger. The decision is available in 24 bunch crossings (2.3 μs) after the real ep interaction. The output rate of the first level trigger is about 1 kHz.

The Second Trigger Level (L2) consists of two independent trigger systems: the topological trigger (L2TT) and the neutral network trigger (L2NN). The latency time for this level is 20 μs. The L2TT trigger decision is based on topological event signatures derived from subdetector signals. The L2NN trigger is a set of 13 neural networks on parallel computers. The training samples of charged current, neutral current and multi-lepton events have been used to check this trigger.

The Third Trigger Level (L3) was placed into operation in 2005 and is mainly used for heavy quark decays identification. The relatively small latency time of the L3, about 100 μm, makes it possible to use time-optimized routines to reconstruct decay particle resonances and event properties.

A full event reconstruction and classification is performed on the last Trigger Level (L4/5). The input rate is approximately 50 Hz, and a full reconstruction starts when the complete event information from all subdetectors is received. The reconstruction is accomplished by a dedicated PC farm, allowing an asynchronous processing which is necessary since complicated events require more computer time. The events which satisfy all requirements are written to tapes at a rate of approximately 10 Hz. The reconstructed events with the whole raw detector information form Production Output Tapes (POTs), whereas the reconstructed quantities only are written as the Data Summary Tapes (DSTs).

3.2 ZEUS detector

Similar to H1, the ZEUS detector is also a multipurpose detector, centered in the interaction point, with an almost hermetic coverage. It has been installed in the Hall SOUTH, where the correspondent beam-beam interaction point was designed. The detector measured approximately 12 m $\times$ 11 m $\times$ 20 m and weighted about 3600 tons. The detector and its components are shown in Figure 23. A complete description of the ZEUS detector can be found elsewhere [75]. Below a brief overview is given.

In the ZEUS detector the interaction point is enclosed by the Central Tracking Detector (CTD) which is a cylindrical wire drift chamber. A super-conducting solenoid magnet surrounds the CTD allowing to measure the charge and momentum of the charged particles. In the forward direction the track reconstruction is performed using the Forward Tracking Detector (FTD) which consists of three planar drift chambers. In the backward (rear) direction, tracks are measured with the Rear Tracking Detector (RTD), which is made of one planar drift chamber.

The ZEUS compensating high resolution Uranium Calorimeter (CAL) surrounds the solenoid

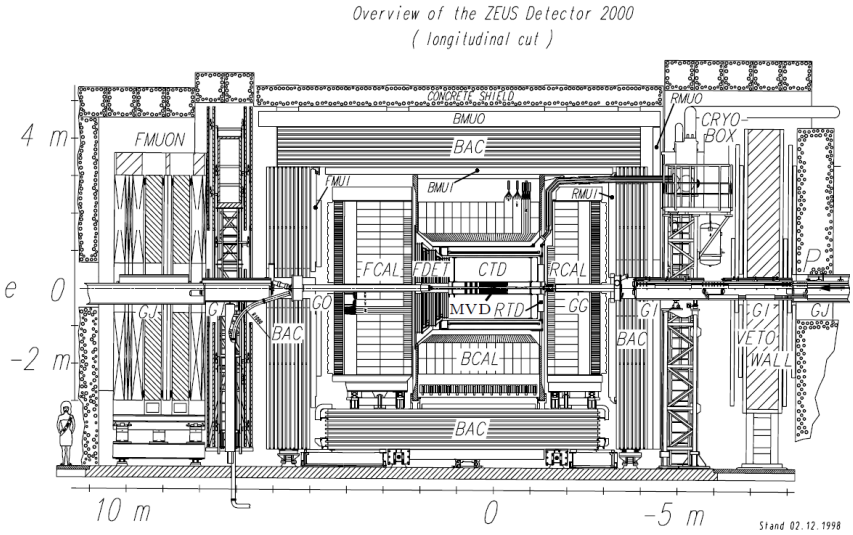

Figure 23: A schematic view of the ZEUS detector in a vertical plane parallel to the beamline.

magnet and the tracking detectors. The solid angle coverage of CAL is more than 99.5% in both hemispheres. It comprises three components: the Forward (FCAL), Barrel (BCAL), and Rear (RCAL) Calorimeters. Each of them has the inner electromagnetic section and the outer hadronic one. The Hadron Electron Separator (HES) covers the electromagnetic sections of RCAL and BCAL by one layer of diodes and FCAL by two layers. The CAL is surrounded by an iron yoke, which provides a return path for the magnetic flux and serves as an absorber for the BAcking Calorimeter (BAC). The BAC is used to measure the energy leakage from the CAL and to determine muon tracks.

The detection of muons is performed by the dedicated detectors: some of them (FMUI, BMUI, RMUI) are installed inside the iron yoke, and some (FMUON, BMUON, RMUON) are outside.

The background from the proton beam-gas interactions is rejected by Veto Wall detector which is placed in the rear direction. The main part of this detector is the iron wall which plays role of a passive absorber.

The luminosity is measured by the luminosity monitor (LUMI) and spectrometer (SPEC) which are also located in the backward (rear) direction.

3.2.1 Uranium calorimeter

The ZEUS calorimeter (CAL) [76] is a high resolution compensating uranium-scintillator calorimeter, which is used to measure the energy of the final state particles. It is the most essential detector to reconstruct the products in the final state after ep collision.

The CAL is primary designed for an optimal jet measurements. It has an angle coverage of 99.5% in the backward hemisphere and 99.8% in the forward hemisphere. The CAL

is a sampling calorimeter consisting of alternating layers of depleted-uranium plates (3.3 mm thick), which serves as absorber medium, and an organic scintillator which is an active material (2.6 mm thick). The thickness of uranium and scintillator layers is tuned in a such way that the response to electromagnetic and hadronic particles of equal energy is the same. The CAL ratio of the responses to electrons and hadrons is very close to 1. This property of calorimeters is called *compensation* and results in an optimal energy resolution for jets.

The CAL is subdivided into three components, FCAL, BCAL and RCAL, which are schematically shown in Figure 24. The FCAL covers the polar angular range $2° < \theta < 40°$, the BCAL $37° < \theta < 129°$ and the RCAL $128° < \theta < 177°$. Each component consists of two sections: inner electromagnetic (EMC) and one or two outer hadronic ones (HAC). Both sections are subdivided into cells, which are the smallest parts of the CAL. The cells of EMC and HAC have different thickness such that electromagnetic or hadronic showers are fully absorbed by the corresponding section. Sections are formed into towers, from which the calorimeter modules are made. The depth in the units of radiation length for the EMC is 22-26 X_0 and in the units of absorption length for HAC is 4-7 λ.

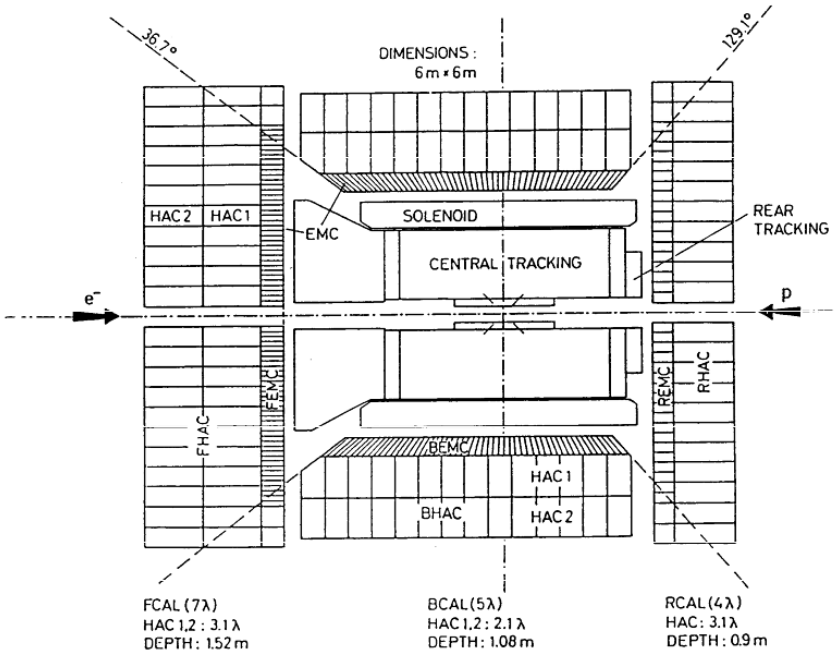

Figure 24: A schematic view of the ZEUS calorimeter together with tracking facilities.

The readout is performed by photomultiplier tubes (PMTs) on two opposite sides of the cell. The PMT signals are digitized by the readout electronics. The CAL has an excellent time resolution of about 2 ns.

The energy resolution of the CAL determined using a test beam is for electrons

$$\frac{\sigma_e}{E} = \frac{18\%}{\sqrt{E/(GeV)}} \oplus 2\%, \tag{79}$$

and for hadrons

$$\frac{\sigma_{had}}{E} = \frac{35\%}{\sqrt{E/(GeV)}} \oplus 1\%, \tag{80}$$

where σ_e and σ_{had} are the RMS spread of the resolution.

3.2.2 Micro Vertex Detector

The Micro Vertex Detector (MVD) [77] has been installed during HERA II upgrade period instead of the HERA I Vertex Detector (VXD). The MVD is designed to improve the space resolution of tracks and determination of the vertex in particular to allow identification of the secondary vertices. The MVD polar angle coverage is $30^\circ < \theta < 150^\circ$.

The MVD consists of two independent components, the barrel (BMVD) and forward (FMVD) detectors. The BMVD is installed close to the interaction point. The FMDV is located next to the barrel region and and extended in the forward direction. A cross section view of the MVD is shown in Figure 25.

The barrel detector consists of 64×64 mm^2 single sided silicon sensors. The sensors are arranged in modules which are mounted in three cylindrical layers around the beamline. These modules are double sided and strips on the opposite-side sensors are perpendicular. It allows measuring $r\phi$ as well as rz position of a hit. A single hit resolution as determined using the test beam condition is 120 μm.

The FMVD consists of four *wheels* of silicon sensors placed perpendicular to the beam pipe. They extend the polar angle coverage down to $\theta > 7^\circ$. Each wheel has two layers of 14 sensors each, mounted back-to-back and shifted by approximately 8 mm in the z direction. Unlike the BMVD sensors, the FMVD ones have trapezoidal shape. There are 480 readout strips in the FMVD sensors.

3.2.3 Central Tracking Detector

The Central Tracking Detector (CTD) [78] is the most essential detector for measuring the three-momenta of charged particles, measuring the energy losses and reconstructing the primary vertex. It is the second closest component to the interaction point. The CTD is a cylindrical drift chamber with active volume ranged from $z = -100$ cm to $z = 104$ cm. The inner radius of 18.2 cm and an outer radius of 79.4 cm. Its polar angle coverage is $15^\circ < \theta < 164^\circ$. The drift chamber is filled with a mixture of argon (82%), ethane (13%) and carbon dioxide (5%). The positive ions produced in gas drift towards the field wires where they are discharged. The electrons drift towards the positively charged sense wires, and, being accelerated by the potential,

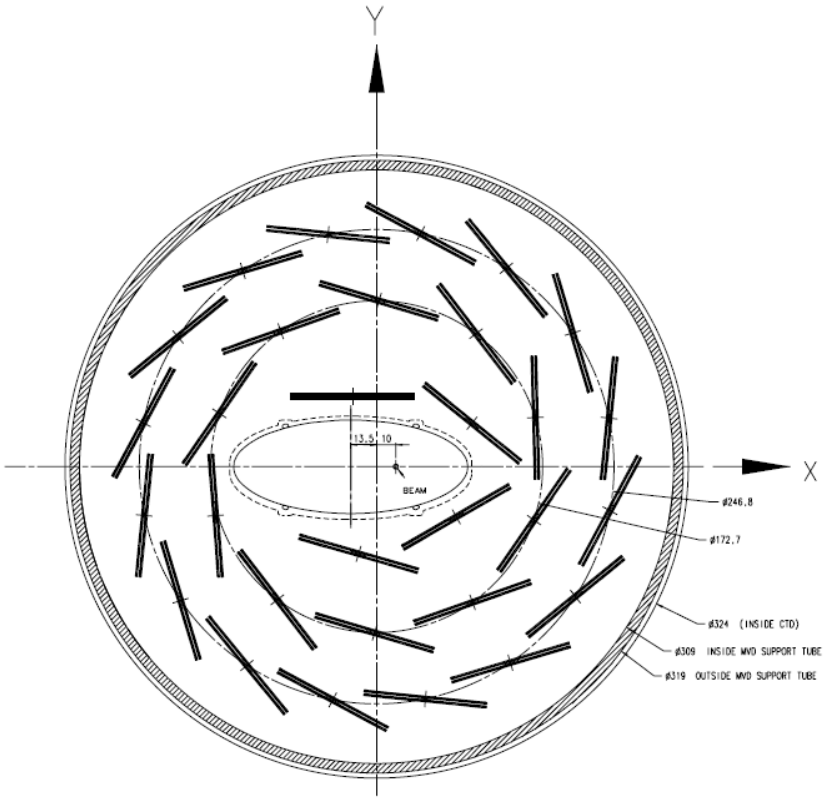

Figure 25: The *xy* cross section of the Micro Vertex Detector.

cause a cascade effect of further ionization. This leads to a shower of electrons impinging upon the sense wire, which is referred as a *hit*.

The CTD sense wires are grouped into cells, which are arranged into 9 circular concentric superlayers. Wires in the odd numbered superlayers are placed parallel to the beam axis, whereas wires in the even numbered ones (*stereo*) have an angle of about $\pm 5^\circ$ with respect to the beam axis (see Figure 26). This allows a determination of the $r\phi$ and z-position with a space resolution of 200 μm and 2 mm, respectively. In addition, the first three superlayers are equipped with a z-by-timing system which determine the z-position by the time difference of the signals arriving to the opposite ends of the wires. This method is mainly used for trigger purpose.

The combined transverse momentum resolution obtained with the CTD+MVD in HERA II is

$$\frac{\sigma(p_T)}{p_T} = 0.0029 \cdot p_T \oplus 0.0081 \oplus 0.0012/p_T, \tag{81}$$

where p_T is given in GeV.

3.2.3.1 Small-angle Rear Tracking Detector The Small-angle Rear Tracking Detector (SRTD) is a tracking detector attached to the front of the RCAL, covering the area of 68×68 cm^2. The

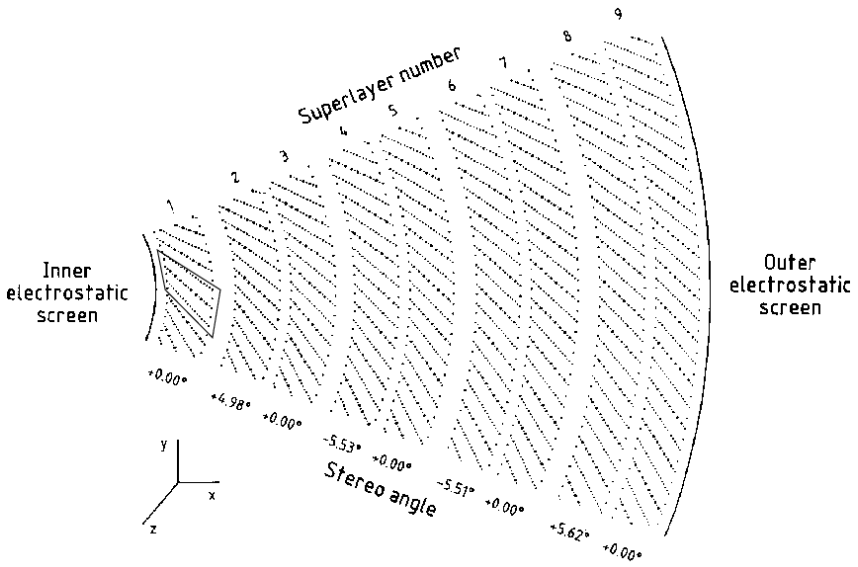

Figure 26: The *xy* cross section of the CTD segment. The sensitive wires in the superlayers are indicated by dots.

SRTD is designed to improve the position and energy measurements of electrons and other charged particles around the beam pipe in the RCAL region. It consists of two planes of scintillator strips, each with four quadrants of 24×44 cm^2. The strips are oriented in the x-direction in one of the planes and in the y direction in the other. The position measurement resolution of SRTD is of 3 mm and the timing resolution is about 2 ns. In addition, the SRTD is also used to correct the energy of electrons for their energy loss in inactive material in front of the CAL.

3.2.3.2 Hadron-Electron Separator The Hadron-Electron Separator (HES) detector is designed to allow a separation between electromagnetic-like and hadronic-like particles based on their shower profiles which differ for electromagnetic-like particles (electrons, photons) and hadrons. The HES detector consists of a layer of silicon diodes (*pads*), 400 μm thick. It is installed inside the RCAL (RHES) and FCAL(FHES) at a longitudinal depth of 3.3 radiation length which corresponds to an approximate position of the electromagnetic shower maximum in the CAL. The fact that the absorption length is in 20 times larger than the electromagnetic radiation length, makes it possible to separate hadrons and electrons. The HES provides a space resolution of about 9 mm for single hits and, in case of multiple hits, clusters are formed and the resolution of position reconstruction improves up to 5 mm.

3.2.4 Luminosity measurement system

Similar to H1, at ZEUS the luminosity is determined by measuring the rate of bremsstrahlung events produced by the Bethe-Heitler process, $ep \rightarrow e\gamma p$. The luminosity measurement at

ZEUS in HERA II running period is performed by two independent systems: the Luminosity Monitor (LUMI) and the Spectrometer (SPEC).

The luminosity measurement in LUMI is based on direct counting the rate of bremsstrahlung photons, leaving the beam pipe at $z = -92.5$ m, by a sampling lead-scintillator calorimeter located downstream of the lepton beam at $z = -107$ m.

The SPEC system [79] has been installed for the luminosity measurement during the HERA II running period. Although the measurement of luminosity by the SPEC detector is also based on counting the rate of bremsstrahlung photons, in contrast to the LUMI system, they are detected through a pair conversation, $\gamma \rightarrow e^+e^-$, in the material of the exit window. The fraction of converted photons is about 10%. The electron-positron pairs are separated by the magnetic field of a dipole magnet and detected by two segmented tungsten-scintillator sampling calorimeters.

The precision of the luminosity measurement at ZEUS is 2.6%.

3.2.5 Trigger system

As it has been already mentioned, the bunch crossing interval at HERA is 96 ns, that corresponds to the bunch crossing rate of about 10 MHz. In order to select interesting physics events a three-level pipe-lined trigger system is used at ZEUS, which makes it possible to achieve the necessary background rate reduction together with a high efficiency for the physics event rates. A schematic view of the ZEUS trigger system is shown in Figure 27.

The First Level Trigger (FLT) is a hardware trigger which reduces the output rate from $\sim$ 10 MHz to $\sim$ 1 kHz. Different components of the ZEUS detector have their own FLTs and the decision on whether the event is passed on Global First Level Trigger (GFLT) or rejected is taken within $\sim 2\mu$s. In the GFLT a decision whether the event should be passed to the next trigger level is made within $\sim 4\mu$s.

The Second Level Trigger (SLT) is a software trigger which reduces the event rate down to $50 - 100$ Hz. Similar to the FLT, the different components has their own SLTs, which pass the information to the Global Second Lavel Trigger (GSLT). The total time for the GSLT to make a decision is about 8 ms. It is longer than for GFLT due to more complex algorithms of selection and running on a larger data set. The GSLT uses more complex quantities, such as calorimeter clusters, tracks and vertex are defined, allowing to take a trigger decision based on an event topology.

If an event is accepted, the complete information about it is sent to the Event Builder (EVB) which creates the final data in the format ready to be used for the last trigger level.

The Third Level Trigger (TLT) is a software trigger running on a computer farm. At this level, the events can be fully reconstructed with algorithms used for the offline analysis, including the calculation of the kinematic variables, muon, electron and jet finding. Events are accepted and classified using different filters which are designed based on the interest of study.

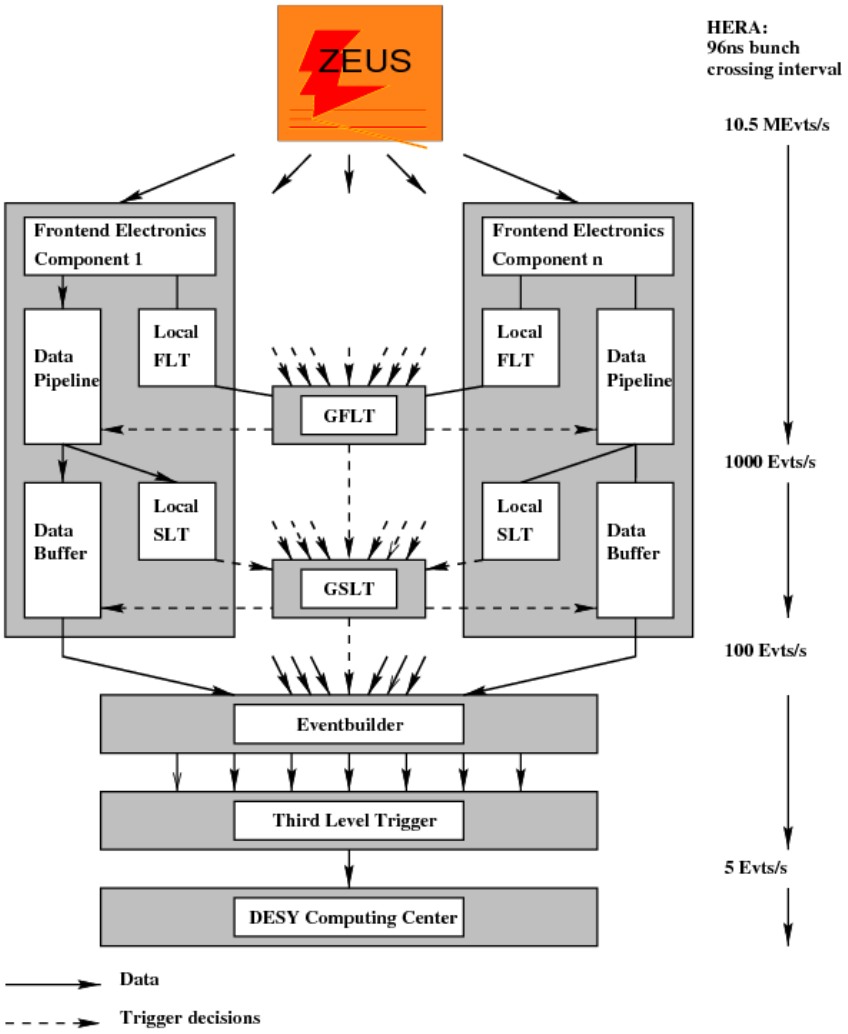

Figure 27: A schematic view of the ZEUS Trigger system.

The final output rate at the TLT is $1-5$ Hz. Finally, like in the case of H1, the events are written on a tape at the DESY computer center and are available for further offline reconstruction and analysis.

3.3 Kinematic reconstruction

At fixed center-of-mass energy $\sqrt{s}$ the event kinematics of the DIS ep scattering processes is defined by three Lorentz invariant variables: x, y, and Q^2 (see Chapter 2). Since they are related by the equation

$$Q^2 = sxy, \tag{82}$$

only two invariant variables are independent. These Lorenz invariant variables cannot be directly measured by the detector components. They are reconstructed from the electron and hadron final state scattering data, namely using the energy and the scattering angle detected by

the subdetector systems. A certain reconstruction method takes into account the measurements of at least two mentioned quantities to determine two independent invariant variables. Several different methods are available for reconstruction of the NC event kinematic due to a redundancy arising from the simultaneous reconstruction of the scattered electron and hadronic final state. Otherwise, in the CC channel the kinematics can be reconstructed using only the method based on the measurement of the hadronic final state since the neutrino is not registered by the detector. The reconstruction methods differ in the resolution and their sensitivity to QED radiative corrections. Typically, the quantities Q^2 and y are reconstructed and x is calculated using the equation (82). Several reconstruction methods are considered in the following.

3.3.1 The electron method

In the electron method [80] the kinematic variables are calculated using the energy E'_e and the polar scattering angle θ_e of the outgoing electron according to the following formulas:

$$\begin{aligned} y_e &= 1 - \frac{E'_e}{E_e}\sin^2\frac{\theta_e}{2}, \\ Q^2_e &= 2E_eE'_e\cos^2\frac{\theta_e}{2} = \frac{P^2_{T,e}}{1-y_e}, \\ x_e &= \frac{Q^2_e}{sy_e}. \end{aligned} \tag{83}$$

Here E_e is the energy of initial electron, $P_{T,e} = E'_e \sin\theta_e$ is the transverse momentum of the electron. This method is the most precise for $y > 0.1$ and it is useful to give here uncertainties for the variables (83). The relative uncertainties of these variables are written as

$$\begin{aligned} \frac{\delta y_e}{y_e} &= \frac{y-1}{y}\frac{E'_e}{E'_e} \otimes \frac{y-1}{y}\cot\frac{\theta_e}{2}\delta\theta_e, \\ \frac{\delta Q^2_e}{Q^2_e} &= \frac{\delta E'_e}{E'_e} \otimes \tan\frac{\theta_e}{2}\delta\theta_e, \\ \frac{\delta x_e}{x_e} &= \frac{1}{y}\frac{\delta E'_e}{E'_e} \otimes \tan\frac{\theta_e}{2}(x\frac{E_p}{E_e} - 1)\delta\theta_e, \end{aligned} \tag{84}$$

where $\otimes$ denotes the squared sum. The method has an excellent resolution in Q^2 over the full kinematic range, whereas the resolution of x and y degrades at low y due to the inverse y-dependencies of the corresponding uncertainties. It also worth noting that since the incident electron energy E_e takes place in y_e and in Q^2_e, this method is sensitive to the initial state radiation.

3.3.2 The hadron method

The hadronic final state (HFS) is characterized using the quantity Σ, the transverse momentum $P_{T,e}$, and the inclusive hadronic polar angle γ_h defined as:

$$\begin{aligned} P_{T,h} &= \sqrt{\left(\sum_i P_{x,i}\right)^2 + \left(\sum_i P_{y,i}\right)^2}, \\ \Sigma &= \sum_i (E_i - P_{z,i}), \\ \tan\frac{\gamma_h}{2} &= \frac{\Sigma}{P_{T,h}}. \end{aligned} \tag{85}$$

Here E_i and $P_{z,i}$ are the energy and the longitudinal momentum component of i-th HFS particle. $P_{x,i}$ and $P_{y,i}$ are the transverse components of the particle momentum. The summation goes over all HFS particles, whose rest masses are neglected. Due to large momentum of the incident proton, the HFS particles are often forward going and lead to losses in the forward beam pipe. The quantities Σ and $P_{T,h}$ are chosen to their relative insensitivity to these losses. Using (85), in the hadron method [81] the kinematic variables are calculated as follows:

$$\begin{aligned} y_h &= \frac{\Sigma}{2E_e}, \\ Q_h^2 &= \frac{P_{T,h}^2}{1 - y_h}, \\ x_h &= \frac{Q_h^2}{s y_h}. \end{aligned} \tag{86}$$

This method is mainly used for reconstruction of the CC DIS kinematics. Due to the low energy resolution of the hadronic energy measurements and decreasing Q^2 resolution as y increasing, the method is almost not used for NC DIS processes.

3.3.3 The sigma method

In the sigma method [82] the kinematic variable y is reconstructed taking advantage of the energy-momentum conservation law. The latter implies that the measured $E - P_z$ equals to two incident electron energies

$$E - P_z \equiv \Sigma + E'_e(1 - \cos\theta_e) = 2E_e. \tag{87}$$

As a result, one can obtain new expression for the kinematic variables from (86):

$$\begin{aligned} y_\Sigma &= \frac{\Sigma}{\Sigma + E'_e(1-\cos\theta_e)}, \\ Q^2_\Sigma &= \frac{P^2_{T,e}}{1-y_\Sigma}, \\ x_\Sigma &= \frac{Q^2_\Sigma}{s y_\Sigma}. \end{aligned} \tag{88}$$

In this method y is less sensitive to the initial state radiation of the electron because the variable y is independent of the scattered electron energy. The method has a high precision at high y and allows crosschecking the electron method in this kinematic range.

3.3.4 The electron-sigma method

The electron-sigma method [83] is an optimal combination of the electron method and the sigma method. It provides a good resolution throughout the kinematic range of the NC measurement with acceptably small QED radiative corrections. In this method the variable Q^2 is calculated according to the electron method and x from the sigma method. The kinematic variables are reconstructed by the formulas:

$$\begin{aligned} y_{e\Sigma} &= 2E_e \frac{\Sigma}{[\Sigma + E'_e(1-\cos\theta_e)]^2}, \\ Q^2_{e\Sigma} = Q^2_e &= \frac{P^2_{T,e}}{1-y_e}, \\ x_{e\Sigma} &= \frac{Q^2_{e\Sigma}}{s y_{e\Sigma}}. \end{aligned} \tag{89}$$

3.3.5 The double angle method

The double angle method [80] is mainly used for calibrating the electromagnetic and hadronic calorimeters, but can be also used for reconstructing the kinematic variables of the NC DIS events. In this method the electron polar angle θ_e and the inclusive hadronic polar angle γ_h are used for determining the kinematics by the following formulas:

$$\begin{aligned} y_{DA} &= \frac{\sin\theta_e(1-\cos\gamma_h)}{\sin\gamma_h + \sin\theta_e - \sin(\theta_e+\gamma_h)}, \\ Q^2_{DA} &= \frac{4E_e^2 \sin\gamma_h(1+\cos\theta_e)}{\sin\gamma_h + \sin\theta_e - \sin(\theta_e+\gamma_h)}, \\ x_{DA} &= \frac{Q^2_{DA}}{s y_{DA}}. \end{aligned} \tag{90}$$

The method has a good resolution at medium y when all particles are well contained within the detector.

It is necessary to note that the double angle method is to the first order independent of the calorimeter energy scales and therefore suitable for calibration of the calorimeters. The energy of the scattered electron used for calibration is given by the formula:

$$E_{DA} = \frac{2E_e \sin\gamma_h}{\sin\gamma_h + \sin\theta_e - \sin(\theta_e + \gamma_h)}. \tag{91}$$

3.4 Cross-section determination

The measurement of the DIS cross section is performed by counting the number of signal events normalized to the integrated luminosity (74). The obtained total cross section corresponds to the entire kinematic region. For each (x, Q^2) bin, the double differential cross section is determined in a similar way by the explicit formula

$$\frac{d^2\sigma(x,Q^2)}{dxdQ^2} = \frac{N_{sig}}{A\mathcal{L}}\frac{1}{\varepsilon}\frac{1}{1+\delta}C_{bin}. \tag{92}$$

Here

- N_{sig} is the difference between the number of selected events and the number of background events estimated from the Monte Carlo (MC) simulation;
- A is the detector acceptance calculated using the MC simulation as the ratio of reconstructed N_{rec} and generated N_{gen} events for a given bin;
- $\mathcal{L}$ denotes the integrated luminosity for the beam runs taken into account;
- ε is the detector efficiency which is defined by the data not included or not properly described by the MC;
- δ denotes the radiative corrections estimated by the MC simulation according to the formula

  $$\delta = \frac{\sigma_{rad}}{\sigma_{Born}} - 1, \tag{93}$$

  where σ_{rad} and σ_{Born} are the bin integrated full and Born-level cross sections, respectively;
- C_{bin} is the bin center correction which is determined as

  $$C_{bin} = \frac{1}{\sigma_{Born}}\frac{d^2\sigma_{Born}}{dxdQ^2}, \tag{94}$$

where the double differential Born-level cross section for the bin center is calculated using the formula (15).

If the radiative corrections are included in the MC simulation, then one can simplify the formula (92) by using the definition of the integrated luminosity for MC $\mathcal{L}_{MC} = N_{gen}/\sigma_{rad}$. In this case, the double differential cross section can be written as

$$\frac{d^2\sigma(x,Q^2)}{dxdQ^2} = \frac{N_{sig}}{N_{rec}}\frac{1}{\varepsilon}\frac{\mathcal{L}_{MC}}{\mathcal{L}}\frac{d^2\sigma_{Born}}{dxdQ^2}. \tag{95}$$

This formula defines the Monte Carlo method for the cross section determination.

4 Analysed data

The data to be combined and the uncertainties due to the systematic error sources are described in this chapter. The systematic uncertainties correspond to cross section measurements for the reduced proton beam energy $E_p = 460, 575$ GeV and nominal proton beam energy $E_p = 920$ GeV data. It starts with the description of the H1 data, some details of the analysis and the systematic sources and follows with the specification of the ZEUS data, brief overview of the analysis and the systematic uncertainties.

4.1 H1 data

The studied datasets represent published measurements [84] of the DIS cross sections at low Q^2 and high y values, using the data collected by the H1 collaboration in the years from 2003 until 2007. The data samples are taken with dedicated high y and low Q^2 triggers. Methods relying on data are used to determine the hadronic background contribution. Four data samples of the $e^{\pm}p$ scattering cross section measurements are under consideration. Two data samples consist of new cross section measurements at the reduced proton energy, $E_p = 460$ GeV and $E_p = 575$ GeV, covering the kinematic domain of $1.5 \leq Q^2 \leq 90$ GeV^2 with integrated luminosities of 12.2 pb^{-1} and 5.9 pb^{-1}, respectively. Other data samples correspond to the cross section measurements for the nominal proton beam energy of $E_p = 920$ GeV. One data sample contains the measurements for $8.5 \leq Q^2 \leq 90$ GeV^2 with the integrated luminosity of 97.6 pb^{-1}. Another data sample at $E_p = 920$ GeV covers the region $2.5 \leq Q^2 \leq 12$ GeV^2 using a dedicated silicon tracker for measurement of the charge of backward scattered particles. These data correspond to an integrated luminosity of 5.9 pb^{-1}.

4.1.1 Some aspects of the analysis

4.1.1.1 Event selection

The analysis is based on several data samples collected during the years 2003 – 2007 which are given in Table 4.

The two high y data samples for the nominal proton beam energy $E_p = 920$ GeV are collected with dedicated low energy SpaCal triggers which require a compact energy deposit in the SpaCal with energy $E > 2$ GeV at L1. To suppress non-ep colliding background, a CIP track segment pointing to the nominal interaction vertex position is required. Several additional veto conditions, which are based on scintillator counters up- and downstream with respect to the nominal interaction position as well as on the hadronic section of the SpaCal, are also used to suppress non-ep background.

The medium Q^2 CJC $E_p = 920$ GeV analysis uses L2 trigger condition which requires that

Data sample	Years	L_{e^-p} pb^{-1}	L_{e^+p} pb^{-1}	Total L pb^{-1}
Medium Q^2 CJC E_p = 920 GeV	2003-2007	44.4	53.2	97.6
Low Q^2 BST E_p = 920 GeV	2006	2.5	3.4	5.9
E_p = 575 GeV	2007	—	5.9	5.9
E_p = 460 GeV	2007	—	12.2	12.2

Table 4: Data samples used in the analysis.

Selection criteria	medium Q^2 CJC E_p = 920 GeV	low Q^2 BST E_p = 920 GeV	reduced energy
Vertex z position	$\lvert Z_{vtx}\rvert < 35$ cm		
Vertex z precision	$\sigma(Z_{vtx}) < 8$ cm		
Scattered lepton energy	$E'_e > 3.4$ GeV		
Radial cluster position	$40 < R_{sp} < 74$ cm	$18 < R_{sp} < 74$ cm	$18 < R_{sp} < 74$ cm
Cluster transverse shape	$R_4 > 0.8$ cm	$R_{\log} < 5$ cm	$R_4 > 0.8$
	ECRA < 4.5 cm	ECRA < 4.5 cm	$R_{\log} < 4.5$ cm for $R_{sp} > 60$ cm
Energy in hadronic Section	$E_h/E'_e < 0.15$		
Tracker validation	$D_{\mathrm{CJC}} < 6$ cm	$D_{\mathrm{BC}} < 3$ cm	
Lepton charge	Agree with beam charge for $y > 0.56$		
Energy-momentum match	—	$\lvert E'_e/P\rvert > 0.5$ for $E'_e < 7$ GeV	
Longitudinal momentum balance	$E-P_z > 35$ GeV		
Total energy in Hadronic SpaCal	—	—	$E_{h,\mathrm{tot}} < 16$ GeV
QED Compton rejection	Topological veto		
Kinematic range	$Q^2 > 7.5$ GeV^2	$Q^2 > 2.37$ GeV^2	$Q^2 > 1.33$ GeV^2

Table 5: Selection criteria.

the energy deposit is reconstructed in the outer SpaCal range, at the distance from the beam line $R_{sp} \geq 38$ cm which corresponds approximately to the inner CJC acceptance. The low Q^2 BST E_p = 920 GeV analysis uses another L2 trigger condition which requires $R_{sp} \geq 17$ cm corresponding to the acceptance of the BST. Both triggers are further filtered at L4 using fully reconstructed events to sharpen low level trigger conditions.

For the reduced proton beam energy run data, the main trigger is the SpaCal trigger at low energy of 2 GeV. The additional tracking segment is reconstructed in the BST pad detector or in the CIP. This trigger is complemented with a trigger at higher energy threshold of $E > 6.5$ GeV and no tracking condition. No L4 filtering is imposed for these runs.

The data are subject to offline cuts which are listed in Table 5. Some of the cuts are common for all data samples, whereas others are different, primarily because of the different tracking used for the scattered lepton validation.

In order to ensure an accurate kinematic reconstruction and to suppress non-ep background, the interaction vertex is required to be reconstructed close to the nominal position with sufficient accuracy.

The scattered lepton is identified with a localized energy deposition (cluster) in the SpaCal calorimeter that is reconstructed at the highest transverse energy E_T. E_T is calculated using the cluster energy and position, the event interaction vertex position and the direction of the beam line. If the highest E_T cluster does not satisfy any of the mentioned below identification cuts,

the next in E_T cluster is tried. The procedure is repeated for up to three clusters. If none of the three clusters satisfies the selection cuts, the event is rejected.

The energy of the scattered lepton is required to exceed $E'_e > 3.4$ GeV to ensure high trigger efficiency. The radial position of the scattered lepton is required to be well inside the SpaCal acceptance and within the active trigger region.

Several cuts are applied to suppress photoproduction background which mainly originates from charge hadrons and $\pi^0 \to \gamma\gamma$ decays for which one of the photons converts into an e^+e^- pair prior to entering the tracking device. The cuts against such background include cuts on transverse shower radius, estimated using logarithmic ($R_{\log}$) and square root (ECRA) energy weighting [85] as well as a fraction of energy of the cluster contained in the four highest energy cells, R_4. The cut $R_4 > 0.8$ is found to be more efficient than the cluster radius estimators, but the L4 trigger condition requires usage of the ECRA cut for the $E_p = 920$ GeV analyses. The transverse shape requirements are efficient against hadronic as well as $\pi^0 \to \gamma\gamma$ background when the two photon clusters merge together.

The cut on the fraction of energy in the hadronic SpaCal behind the lepton candidate cluster, $E_h/E'_e < 0.15$, rejects purely hadronic background. The cut does not reject background for $R_{sp} > 60$ cm because of the limited acceptance of the hadronic SpaCal. As a compromise between signal efficiency and background rejection, an extra cut $R_{\log} < 4.5$ is introduced at $R_{sp} > 60$ cm.

The photoproduction background is suppressed further by requiring cluster validation by a track The medium Q^2 CJC analysis uses tracks reconstructed solely in the CJC tracker. The other analyses use a dedicated reconstruction algorithm which combines information obtained from the CJC, BST, event vertex and the SpaCal (*BC* algorithm [86]). The tracks are extrapolated to the SpaCal position and required to match the SpaCal cluster within $D_{\mathrm{CJC}} < 6$ cm for the CJC reconstruction and within $D_{\mathrm{BC}} < 3$ cm for the BC algorithm. Tighter cut on the track-cluster matching for the BC compared to CJC algorithm is possible for low R_{sp} because of accurate BST θ_e reconstruction and for higher R_{sp} because the SpaCal cluster is used in the BC algorithm and thus pulls the track towards the cluster. As it is discussed in [84], the scattered lepton charge is required to match the beam charge for $y > 0.56$. The sample for which the charges are different is used to estimate the remaining background. For $E'_e < 7$ GeV, the momentum reconstruction is accurate enough to require energy-momentum match, $|E'_e/P| > 0.5$.

The total energy reconstructed in the hadronic section of the SpaCal, $E_{h,\mathrm{tot}}$, is required to be below 16 GeV for the reduced proton beam energy data. This avoids trigger ineficiency arising from a veto on the total energy deposited in the hadronic SpaCal, applied at L1.

Events with high energy initial state photon radiation (ISR) are rejected by requiring $E-P_z > 35$ GeV. This cut is also efficient against the photoproduction background. The QED Compton process $ep \to ep\gamma$, where e and γ are scattered at large angle with respect to each other, is suppressed using a topological cut against events with two back-to-back electromagnetic clusters

reconstructed in the SpaCal.

The distribution of the variables which are used for the scattered lepton identification are obtained [84]. The electron identification selection criteria are designed to have high efficiency for the signal while rejecting significant amount of the background.

4.1.1.2 Cross section determination

For $Q^2 \leq 100$ GeV^2 the contributions to the NC scattering process are dominated by photon exchange with negligible differences between e^+p and e^-p scattering cross sections. The determination of the background is based on the measured lepton-candidate charge. In order to reduce sensitivity to the background charge asymmetry, the cross section is determined for a charge symmetric data sample for medium Q^2 CJC and low Q^2 BST samples. The cross section is calculated in this case for each (x, Q^2) bin according to formula (95), which can be explicitly written as

$$\sigma_r(x, Q^2) = \frac{N_{\text{sig}}^{e^-p} + N_{\text{sig}}^{e^+p} \frac{\mathcal{L}^{e^-p}}{\mathcal{L}^{e^+p}}}{N_{\text{sig,MC}}^{e^-p} \frac{\mathcal{L}^{e^-p}}{\mathcal{L}_{\text{MC}}^{e^-p}} + N_{\text{sig,MC}}^{e^+p} \frac{\mathcal{L}^{e^-p}}{\mathcal{L}_{\text{MC}}^{e^+p}}} \sigma_r^{\text{MC}}(x, Q^2)\,, \tag{96}$$

where $\mathcal{L}^{e^\pm p}$ ($\mathcal{L}_{\text{MC}}^{e^\pm p}$) is the integrated luminosity for the data (MC), $N_{\text{sig,MC}}^{e^\pm p}$ is the number of signal events in MC and $\sigma_r^{\text{MC}}(x, Q^2)$ is the value of the reduced cross section in MC. The DJANGOH MC event generator [89] is used for generation of the DIS signal events. The efficiency is included to MC.

Equation (96) is fairly insensitive to the uncertainty of the background charge asymmetry. The statistical precision of equation (96) is limited by the sample with smaller luminosity, therefore the data taking strategy was tuned to obtain e^+p and e^-p samples of about equal size.

For the reduced proton beam energy samples, the absence of e^-p data does not allow us to use the equation (96), and a more standard cross section determination formula (95) is used

$$\sigma_r(x, Q^2) = \frac{N_{\text{sig}}^{e+p}}{N_{\text{sig,MC}}^{e+p} \frac{\mathcal{L}^{e^+p}}{\mathcal{L}_{\text{MC}}^{e^+p}}} \sigma_r^{\text{MC}}(x, Q^2)\,. \tag{97}$$

The background events are simulated using MC. These cross sections are more sensitive to the uncertainty in the background charge asymmetry.

As a results, cross section measurements [84] have been obtained. The measurements cover range between $Q^2 = 1.5$ GeV^2 and $Q^2 = 90$ GeV^2 reaching high inelasticity $y = 0.85$. The new data provide the first H1 cross-section measurement for the reduced proton energies $E_p = 460$ GeV and $E_p = 575$ GeV. For the high y region, the precision of the nominal proton beam energy data significantly exceeds accuracy of the previous H1 results [69,70], if the global normalization uncertainty is not considered in the comparison. The global normalization

uncertainty, however, is much larger for the new result and this offsets overall precision of the new data.

4.1.2 The systematic uncertainties

The systematic uncertainty on the cross section measurements arises from several contributions. Besides the global normalization uncertainty, these contributions are classified as correlated uncertainties, which affect measurements at different Q^2 and x in a correlated manner, and as uncorrelated ones, for which each of the measurements is affected individually. The summary of all systematic sources for the studied H1 data [84] is given in Table 6.

The global normalization uncertainty is 4% for the $E_p = 460$ GeV and $E_p = 575$ GeV periods, whereas it equals to 3% for the $E_p = 920$ GeV period. The uncertainty includes the uncertainty of the luminosity measurement as well as global trigger and reconstruction efficiency uncertainties.

The uncertainty on the SpaCal electromagnetic energy scale for medium Q^2 CJC $E_p = 920$ GeV is chosen to be 0.3% at $E'_e = 27.5$ GeV increasing to 1% at $E'_e = 2$ GeV because of large period of covered runs. For the reduced proton energy and low Q^2 BST $E_p = 920$ GeV data the uncertainty is determined to be 0.2% at $E'_e = 27.5$ GeV increasing to 1% at $E'_e = 2$ GeV. The uncertainty at around 27.5 GeV is estimated from the difference between the result of the double-angle calibration and the position of the kinematic peak. The uncertainty at $E'_e = 2$ GeV is obtained using $J/\psi \to e^+e^-$ and $\pi^0 \to \gamma\gamma$ decays [69].

The uncertainty on the lepton polar angle is 0.5 mrad, which covers uncertainties of the alignment of the SpaCal as well as of the cluster position determination.

The hadronic energy scale has an uncertainty of 4%. Apart from reconstruction in the LAr calorimeter and in the tacker, this value covers the uncertainty of the hadronic energy scale of the SpaCal, which is important at high y. The uncertainty of the LAr electronic noise and the beam related background is 20%. These uncertainties have little impact on the cross-section measurement which is based on the electron method since they enter only via the $E - P_z$ cut.

The background charge asymmetry is determined with a precision of 2%. It affects only the data for $y \geq 0.56$ where the wrong charge subtraction method is used. For the $E_p = 460$ GeV and $E_p = 575$ GeV runs, the impact on the cross section reaches 3.5% at $y = 0.85$. The uncertainty does not affect the medium Q^2 CJC $E_p = 920$ GeV and low Q^2 BST $E_p = 920$ GeV measurements since they are based on both e^+p and e^-p HERA running periods.

The electron tagger acceptance is known to 20%. This uncertainty is applied for $y < 0.56$ only and, since the background at low y is small, this source does not have a significant impact on the measurement.

The uncorrelated systematic uncertainties include the Monte Carlo statistical errors and the following sources: the uncorrelated part of the trigger efficiency, known to 1%; the track-cluster

link efficiency, known to 1.5%; the uncertainty of the lepton charge determination of 0.5% leading to 1% uncertainty of the cross section, for $y \geq 0.56$ only; the electron identification uncertainty varies from 3% for $y > 0.8$ to 1% for $y < 0.6$; the uncertainty due to the radiative corrections is determined to be 1%.

Uncorrelated uncertainty source	Value
Trigger efficiency	1%
Track-cluster link efficiency	1.5%
Lepton charge determination	1%
Electron identification efficiency	1-3%
Radiative corrections	1%
Correlated uncertainty source	**Value**
Global normalization	3 or 4%
E'_e energy scale	0.2 to 1% or 0.3 to 1%
Polar angle θ_e	0.5mrad
Hadronic energy scale	4%
LAr noise	20%
Background charge asymmetry	2%
Electron tagger acceptance	20%

Table 6: Summary of the H1 systematic uncertainties. The uncertainties of the correlated error sources are given in terms of the uncertainty in the corresponding source. The uncertainties of the uncorrelated error sources are given in terms of the effect on the measured cross section.

4.2 ZEUS data

The ZEUS reduced proton beam energy, $E_p = 460, 575$ GeV, and nominal proton beam energy, $E_p = 920$ GeV, data [87] have been collected during 2006 and 2007 years. The data cover the kinematic region of $20 \leq Q^2 \leq 130$ GeV^2 and $0.09 \leq y \leq 0.78$ which correspond to Bjorken-x $5 \cdot 10^{-4} < x < 0.007$. The corresponding collected integrated luminosities for each proton beam energy are 13.9 pb^{-1}, 7.1 pb^{-1} and 44.5 pb^{-1}.

The ZEUS measurements and the analysis are described in detail in [87,88]. A brief description of this analysis is given below.

4.2.1 Some aspects of the analysis

In the analysis, the kinematic variables are reconstructed using the electron method. A neural network is used for electron identification. This network is based, in turn, on the moments of the three dimensional shower profile of clusters found in the CAL. The energy of the scattered electron, E'_e, is determined using the CAL, whereas the scattering angle, θ_e, is found using the reconstructed interaction vertex and position of the scattered electron in the SRTD or in

the RHES, if the event takes place outside the SRTD acceptance. The angle of the scattered electron cannot be reliably determined using the SRTD+HES system in less than 2% of events. Therefore, these events are rejected.

The quantity $\Sigma = \sum_i (E_i - p_{Z,i})$, where the sum runs over all CAL energy deposits, is used in the trigger and in the offline analysis. The conservation law states that $2E_e = 55$ GeV. A substantial reduction of Σ is caused by the electron final state in photoproduction events which are not detected. A very large Σ is obtained from non-ep collisions.

The online selection of the events is performed by the three-level trigger system. A dedicated trigger makes it possible to obtain high efficiency for high y events. To satisfy the trigger condition, an event should have $\Sigma > 30$ GeV and either an electron candidate with $E'_e > 4$ GeV in the RCAL, or $\Sigma > 20$ GeV calculated solely from the CAL energy deposits for polar angle less than 165°.

The data are subject to offline cuts which are overviewed below:

- 42 GeV $< \sum_i (E_i - p_{Z,i}) <$ 65 GeV;
- The vertex z position: $|Z_{vtx}| < 30$ cm;
- The scattered lepton energy: $E'_e > 6$ GeV;
- The event topology does not correspond to the elastic QED Compton event;
- The event timing is in agreement with the HERA bunch crossing interval;
- The estimation of the inelasticity by the Jacquet-Blondel method larger than 0.05 and the reconstructed inelasticity itself less than 0.95;
- The ratio of the transverse momentum of the hadronic system and electron: $p_{T,h}/p_{T,e} > 0.3$;

The projected path of the electron candidate is required to exit the CTD at a radius larger than 20 cm and enter the RCAL at a radius smaller than 135 cm.

Hit information based on the ratios of the number of observed to the maximum number of possible hits in the MVD and CTD is used to identify the tracks of the electron candidates. These ratios are larger than 0.45 and 0.6 for MVD and CTD, respectively.

The reduced cross section in a given bin is obtained according to (97). The DIS processes are simulated using DJANGOH 1.6 MC model [89], whereas the background events which consist mostly of the photoproduction events are simulated using the PYTHIA 6.2 MC model [90]. The proton PDFs for calculating the numbers of MC events as well as the Born-level reduced cross section are parametrized by CTEQ5D [91].

As a result, the measured cross section data consist of 54 data points for each proton beam energy. The obtained cross section measurements in the datasets cover the kinematic region of $24 \leq Q^2 \leq 110$ GeV^2 and $0.13 \leq y \leq 0.75$.

4.2.2 The systematic uncertainties

The description of the error sources for the systematic uncertainties for the ZEUS data are given below:

- $\{\delta_{\gamma p}\}$: The photoproduction background is estimated using the PYTHIA MC model with an enlargement of the contribution of the direct subprocesses and reduction of the diffractive ones. The predicted photoproduction cross sections for all proton beam energies $E_p = 460, 575, 920$ GeV are then validated against photoproduction data samples selected using the 6m-tagger. The predicted cross sections are consisted with these data within 10% total uncertainty on the data.

- $\{\delta_{E_e}\}$: The scattered electron energy distribution for the data and MC is compared. The distribution is reconstructed using the double angle method and kinematic peak events in DIS and then verified on the QED Compton events and on J/Ψ events. The scattered electron energy in the data and MC is consistent within uncertainty of 0.5% for $E'_e >$ 20 GeV which increases to 1.9% at $E'_e = 6$ GeV.

- $\{\delta_{E_h}\}$: The hadron energy scale uncertainty is estimated by comparison of the identically corrected data and MC simulations. The hadron energy scale corrections are obtained from the ratio of the single jet energy reconstructed with the double angle method and calculated using the CAL only. The electron energy used in double angle method is measured by CTD. The MC agrees with the data within 2%, therefore 2% hadronic energy-scale uncertainty is used.

- $\{\delta_{eID}\}$: The estimation of the electron finding efficiency is based on the energy-dependent probability cut. The applied cut is, in turn, chosen depending on the correlations of the electron finder probability versus the reconstructed electron energy for DIS events and MC. The used electron finder is based on the neural network algorithm.

- $\{\delta_{dx}, \delta_{dx}\}$: The SRTD and HES position uncertainty of 2 mm in both the horizontal and vertical directions is used.

- $\{\delta_{MVD}, \delta_{CTD}\}$: The uncertainty on the hit-finding efficiency is estimated by variation of the hit fraction criteria which is a ratio of the number of observed hits to the maximum number of possible hits in MVD and CTD. The variation is applied simultaneously to data and MC.

- $\{\delta_{diff}\}$: The 10% uncertainty on the scale factors applied to the diffractive DJANGOH component is considered.

The effect of a variation of the given systematic source on the measured cross section is taken as one standard deviation of the Gauss distribution.

Along with the uncertainties listed above, there is a total normalization uncertainty which includes:

- the luminosity uncertainty which is 2.6% for all proton beam energies $E_p = 460, 575, 920$ GeV;
- the interaction-vertex distribution simulation uncertainty, evaluated by comparing the ratio of the number of events with vertex position $|z_{vtx}| \leq 30$ cm and $|z_{vtx}| > 30$ cm in data and MC of 0.3%.
- the trigger-efficiency uncertainty of 0.5%.

These three uncertainties are perfectly correlated between bins. Added in quadrature, they determine a total normalization uncertainty of 2.7%, of which 2.5% is correlated between the running periods and 1.1% uncorrelated. The electroweak correction uncertainty is negligible.

5 Combination procedure

In this chapter the combination method used for the H1 and ZEUS data combination is discussed. The combination method [92] is based on a χ^2-function, assuming that data points are statistically uncorrelated within one experiment. The correlations of the systematic sources for different experiments are taken into account in the combination procedure via certain sensitivity factors and additional measured parameters. Initially, the uncertainties of the measured data points are considered as independent of the central values. In this case, the minimization procedure based on the least square method [93] can be applied. The minimized χ^2-function has a quadratic dependence on the minimization parameters and thus its minimization is obtained by solving a system of linear equations. However, since the statistical and systematic uncertainties depend on the central values, this leads to a deviation from a simple quadratic dependence and requires the iterative procedure for the combination.

5.1 The maximum likelihood estimation

The proposed combination method comes from the technique for parameter estimation which is called maximum likelihood estimation [94]. The latter considers N data points μ^i to be explained by a mathematical model θ with some parameters. If the data points have independent probability distribution functions $p(\mu^i|\theta)$, then it is possible to define the likelihood function $P(\theta)$ as a multiplication of the distribution functions

$$P(\theta) = p(\mu^1|\theta) \dots p(\mu^N|\theta). \tag{98}$$

The maximum of $P(\theta)$ with respect to θ is the condition for obtaining the estimation for parameters of the model.

If we restrict the probability to the normal distribution [95] defined by the probability density function

$$p(\mu^i|m,\Delta) = \frac{1}{\Delta\sqrt{2\pi}} \exp\left\{-\frac{(m-\mu^i)^2}{2\Delta^2}\right\}, \tag{99}$$

with unknown m and Δ, then the maximum of $P(\theta)$ leads to the minimum of the positive χ^2-function

$$\chi^2(m) = \sum_{i=1}^{N} \left\{\frac{m-\mu^i}{\Delta}\right\}^2, \tag{100}$$

which can be found by the extremum condition

$$\frac{d\chi^2}{dm} = 0. \tag{101}$$

This requirement gives an estimate m^0 of m and Δ_0^2 of Δ^2 by the formulas

$$m^0 = \frac{1}{N}\sum_{i=1}^{N}\mu^i, \quad \Delta_0^2 = \frac{1}{N}\sum_{i=1}^{N}\left(m^0 - \mu^i\right)^2. \tag{102}$$

The application of the method explained above to the normally distributed physical observables measured from different experiments gives us the proposed combination method. The uncertainties of the physical quantities obtained at a certain experiment e is characterized by a certain mathematical model θ_e and consequently by a likelihood function $P(\theta_e)$. Considering only one measurement μ^e for each independent experiment, one can construct the general likelihood function as a product of independent functions

$$P(\Theta) = \prod_{e}^{E} P(\theta_e) = \prod_{e}^{E} p(\mu^e|\theta_e), \tag{103}$$

where E is a total number of experiments. We assume that the deviations $\epsilon = m - \mu^e$ of the measured physical quantities m have the normal distribution. This assumption provides a good approximation in many cases and is regarded as the main point of the uncertainty estimation in the experimental physics. It allows us to consider the measurement as a random value spread by the normal distribution near the central value and to obtain

$$P(\Theta) = \left(\frac{1}{\sqrt{2\pi}}\right)^E \left[\prod_{e}^{E}\frac{1}{\Delta_e}\right] \exp\left\{-\sum_{e}^{E}\frac{(m-\mu^e)^2}{2\Delta_e^2}\right\}, \tag{104}$$

where μ^e and Δ^e are independent and different for each experiment. The minimization of the power coefficient gives the averaged over experiments value for m and Δ

$$m_{ave} = \frac{1}{\Delta_{ave}^2}\sum_{e}^{E}\frac{\mu^e}{\Delta_e^2}, \quad \Delta_{ave}^2 = \sum_{e}^{E}\frac{1}{\Delta_e^2}. \tag{105}$$

It is necessary to note here that the given scheme coincides with the scheme for obtaining the estimate according to the method of least squares and the relations (105) are the formulas of this method. As a result, our combination method is a modification of the method of least squares.

5.2 The combination method

Inclusion of the systematic error sources slightly changes the details of the averaging procedure. The averaging is based on a comparison of the measured value with the value of the physical quantity at point i, which is the unknown averaged central value denoted by m^i. In general, the measured value μ^i at point i has the uncorrelated uncertainty Δ_i and the correlated systematic uncertainty. The former is related to the statistical $\Delta_{i,stat}$ and uncorrelated systematic uncertainty

$\Delta_{i,unc}$ as $\Delta_i^2 = \Delta_{i,stat}^2 + \Delta_{i,unc}^2$. The latter is given by $\partial\mu^i/\partial\alpha_j$, where α_j denotes the central value for a correlated systematic error source. $\partial\mu^i/\partial\alpha_j$ defines the sensitivity of the measurement μ^i at point i to the systematic source j and this sensitivity can be different for different measured values. It is also useful to define the relative correlated systematic uncertainty of μ^i by the ratio

$$\gamma_j^i = \frac{\partial\mu^i/\partial\alpha_j}{\mu^i}. \tag{106}$$

The correlated systematic uncertainty is taken into account by introduction of the additional parameter of minimization $b_j = a_j - \alpha_j$ which is the shift of the systematic uncertainty and α_j is the central value of the systematic source. By convention, one can choose $\alpha_j = 0$ and assume unit uncertainty for b_j. As a result, an extra term of $\pm\partial\mu^i/\partial\alpha_j$ is added to describe the correlated uncertainty for the measured value at point i.

The two types of the uncertainty treatment are used at HERA:

1) the *additive* treatment, if the systematic uncertainties are proportional to the measured values

$$\Gamma_j^i = \mu^i\gamma_j^i \tag{107}$$

2) the *multiplicative* treatment, if the systematic uncertainties are proportional to the central values

$$\Gamma_j^i = m^i\gamma_j^i. \tag{108}$$

Here Γ_j^i is the matrix of the correlated systematic uncertainties, which takes into account the type of uncertainty treatment.

The combination procedure is based on the minimization of the χ^2-function which takes into account all assumptions mentioned above. For a single experiment the χ^2-function is given by the formula [69]

$$\chi^2_{exp}(\vec{m},\vec{b}) = \sum_i \frac{\left(m^i - \sum_j \Gamma_j^i b_j - \mu^i\right)^2}{\Delta_i^2} + \sum_j b_j^2. \tag{109}$$

The χ^2_{exp}-function depends on two vectors: values of the physical quantity $\vec{m}$ and on the shifts of the systematic uncertainties $\vec{b}$. The above formula can be generalized to several experiments by denoting the number of measurements by N_M and the number of systematics sources by N_S. This leads us to the χ^2_{tot}-function

$$\chi^2_{tot}(\vec{m},\vec{b}) = \sum_e \sum_{i=1}^{N_M} \frac{\left(m^i - \sum_{j=1}^{N_S} \Gamma_{j,e}^i b_j - \mu_e^i\right)^2}{\Delta_{i,e}^2} w_{i,e} + \sum_{j=1}^{N_S} b_j^2. \tag{110}$$

Here the first sum runs over all experiments and the symbol $w_{i,e}$ is equal to 1 if the experiment e contributes a measurement at the point i, otherwise it is equal to 0. In a similar way, $\Gamma_{j,e}^i$ is equal to zero if the measured value at point i from experiment e is insensitive to the systematic

source j.

The denominator of (110) contains variance which can be also treated additively and multiplicatively. In case of additive treatment, the variance $\Delta_i^2 = \Delta_{i,stat}^2 + \Delta_{i,unc}^2$ depends only on the measured values μ^i and is consequently constant. Thus equation (110) is a quadratic form of $\vec{m}$ and $\vec{b}$. This quadratic form can be reduced to

$$\chi^2_{tot}(\vec{m},\vec{b}) = \chi^2_{min} + \sum_{i=1}^{N_M} \frac{\left(m^i - \sum_{j=1}^{N_S} \frac{\partial \mu^{i,ave}}{\partial \alpha_j} b_{j,ave} - \mu^{i,ave}\right)^2}{\Delta^2_{i,ave}} + \sum_{j=1}^{N_S}\sum_{k=1}^{N_S} b_{j,ave} b_{k,ave} [\mathbf{A}'_s]^{jk}. \qquad (111)$$

The values μ^i_{ave} and $b_{j,ave}$ define the minimum of χ^2_{tot} and are found from the extremum condition. The formulas for these variables as well as for matrix $\mathbf{A}'_s$ are given in the next section. The multiplicative treatment is discussed in the section after next.

5.3 The minimization method

The minimization of the χ^2_{tot}-function (110) is performed in a following way. The χ^2 is a quadratic function of its parameters and the minimum is given by the extremum conditions

$$\frac{\partial \chi^2_{tot}}{\partial m^i}(\vec{m},\vec{b}) = 0, \quad \frac{\partial \chi^2_{tot}}{\partial b^i}(\vec{m},\vec{b}) = 0. \qquad (112)$$

In case of the additive treatment of the uncertainties the equations (112) produce the system of linear equations, whereas for the multiplicative one the system is nonlinear and the iteration procedure is used. The linear system can be presented in the block form

$$\begin{pmatrix} \mathbf{A}_M & \mathbf{A}_{SM} \\ \mathbf{A}^T_{SM} & \mathbf{A}_S \end{pmatrix} \begin{pmatrix} \vec{M}^{ave} \\ \vec{B}^{ave} \end{pmatrix} = \begin{pmatrix} \vec{C}_M \\ \vec{C}_S \end{pmatrix}, \qquad (113)$$

where the blocks and vectors are explained below. The block $\mathbf{A}_M$ has a diagonal structure with N_M diagonal elements. The i-th element is defined as a sum over experiments of inverse squared variances of the measurements at point i (common for all experiments):

$$[\mathbf{A}_M]^{ii} = \sum_e \frac{1}{\Delta^2_{i,e}}. \qquad (114)$$

The block $\mathbf{A}_{SM}$ has a size $N_M \times N_S$ and their elements are defined as

$$[\mathbf{A}_{SM}]^{ij} = -\sum_e \frac{\Gamma^i_{j,e}}{\Delta^2_{i,e}}. \qquad (115)$$

The elements of the coupling block $\mathbf{A}_S$ are given by the formula

$$[\mathbf{A}_S]^{ij} = \delta_{ij} + \sum_e \sum_{k=1}^{N_M} \frac{\Gamma^k_{i,e}\Gamma^k_{j,e}}{\Delta^2_{k,e}}, \tag{116}$$

where δ_{ij} is the Kronecker delta and sums run over all N_M measured points and over all experiments. The right hand side vectors are given by the following expressions:

$$[\vec{C}_M]^i = \sum_e \frac{\mu^i_e}{\Delta^2_{i,e}}, \tag{117}$$

$$[\vec{C}_S]^i = -\sum_e \sum_{k=1}^{N_M} \frac{\mu^k_e \Gamma^k_{i,e}}{\Delta^2_{k,e}}. \tag{118}$$

In the above formulas, the weight coefficient $w_{i,e}$ is omitted for simplicity.

The linear system (113) is solved and the vectors $\vec{M}^{ave}$ and $\vec{B}^{ave}$ are obtained. Although solving of the system can be performed directly by inversion of the whole matrix, it is more convenient to take advantage of the diagonal structure of the block $\mathbf{A}_M$. Applying the method of the Schur complement, the system (113) is reduced to the form

$$\begin{pmatrix} \mathbf{A}_M & \mathbf{A}_{SM} \\ \mathbf{0} & \mathbf{A}_S - \mathbf{A}^T_{SM}\mathbf{A}^{-1}_M\mathbf{A}_{SM} \end{pmatrix} \begin{pmatrix} \vec{M}^{ave} \\ \vec{B}^{ave} \end{pmatrix} = \begin{pmatrix} \vec{C}_M \\ \vec{C}_S - \mathbf{A}^T_{SM}\mathbf{A}^{-1}_M\vec{C}_M \end{pmatrix}. \tag{119}$$

The block upper triangular form of the matrix allows us to easily obtain the solution

$$\begin{aligned} \vec{B}^{ave} &= \tilde{\mathbf{A}}^{-1}_S \left(\vec{C}_S - \mathbf{A}^T_{SM}\mathbf{A}^{-1}_M\vec{C}_M\right), \\ \vec{M}^{ave} &= \mathbf{A}^{-1}_M \left(\vec{C}_M - \mathbf{A}_{SM}B^{ave}\right), \end{aligned} \tag{120}$$

where

$$\tilde{\mathbf{A}}_S = \mathbf{A}_S - \mathbf{A}^T_{SM}\mathbf{A}^{-1}_M\mathbf{A}_{SM}. \tag{121}$$

It is worth noting that the only nontrivial inversion in (120) is the inversion of the block $\tilde{\mathbf{A}}_S$. The size of this block is usually smaller than the size of the initial matrix, therefore the proposed scheme is preferable for computation. The equation (120) provides the explicit formula for μ^i_{ave} by using the components of vector $\vec{B}^{ave}$. The components of the solution $\vec{M}^{ave}$ are given by

$$\mu^{i,ave} = \frac{\sum_e \left[\left(\mu^i_e + \sum_j \Gamma^i_{j,e} b_{j,ave}\right)\frac{1}{\Delta^2_{i,e}}\right]}{\Delta^2_{i,ave}}, \tag{122}$$

where the average variance is defined by the inverse of elements of the diagonal matrix $\mathbf{A}_M$

$$\Delta^2_{i,ave} = \frac{1}{\sum_e \frac{1}{\Delta^2_{i,e}}}. \tag{123}$$

5.4 Iterative procedure

In case of the multiplicative treatment of the uncertainties, the statistical, correlated and uncorrelated uncertainties are considered as functions of the central values of measurements. Moreover, the statistical uncertainties $\Delta_{i,stat}$ are proportional to the square roots of the central values:

$$\Delta_{i,stat} = \delta_{i,stat}\sqrt{m^i\mu^i}. \tag{124}$$

The correlated and uncorrelated systematic uncertainties are proportional to the central values:

$$\begin{aligned} \Gamma^i_j &= m^i\gamma^i_j, \\ \Delta_{i,unc} &= m^i\delta_{i,unc}. \end{aligned} \tag{125}$$

This affects the denominator of the formula (109) for χ^2_{exp} and changes it to

$$\Delta^2_{i,e} = \delta^2_{i,stat}\mu^i\left(m^i - \sum_{j=1}^{N_S}\gamma^i_j m^i b_j\right) + \delta^2_{i,unc}(m^i)^2. \tag{126}$$

The dependence of $\Delta_{i,e}$ on m^i and b_j breaks the quadratic form of the χ^2-function. Therefore, an iterative procedure is used to find its minimum. For each iteration, the denominator is set to a constant value and the solution (122) is used. To evaluate $\Delta_{i,e}$, it is assumed that $m^i = \mu^i$ and $b_j = 0$ for the first iteration and that $m^i = \mu^i_{ave}$ and $b_j = b_{j,ave}$ for the consequent iterations. The convergence is achieved after two iterations.

6 Results

In this chapter the results of a combination of the published H1 and ZEUS reduced proton beam energy, $E_p = 460, 575$ GeV, cross section data are presented. The developed common bin grid for the combination and a modified procedure for calculation of the swimming corrections are used. The combination and the account of ambiguities due to the different treatment of the uncertainies are described. The DGLAP and dipole model fits to the combined data are performed. The fitted parameters for the models are obtained and the results of the fits are described in detail. The longitudinal structure function is also extracted from the data and compared to the published results of the H1 collaboration.

6.1 The common grid

The combination of two measurements is feasible only if they are measured at the same (x, Q^2) bin center. Since the bins for the H1 and ZEUS experiments are different, it is necessary to extrapolate (swim) the measurements corresponding to nearby bins into one bin before the averaging. The extrapolation from one bin to another leads to change of the cross section. The correction of the cross section (swimming correction) can be based on different theoretical predictions. In our analysis the HERAPDF1.0 QCD fit results are used by default for calculation of the theoretical cross sections.

The common grid is based on the condition of the minimal swimming corrections. The latter is achieved by performing shifts of (x, Q^2) bins as smaller as possible. In addition, in order to keep the initial Q^2 binning of the data, the shifts along x bins are more preferable than shifts along Q^2. Also, the extraction of longitudinal structure function F_L requires to obtain unbiased estimate of the uncertainties as for high y and therefore it is important to avoid significant swimming in y for high values of y.

Although there can be the measurements which originate from either H1 or ZEUS and are not changed during the swimming, they become shifted after the averaging due to correlations of their systematic sources. In case of more than one measurement of the same experiment swim to the same common grid bin, these measurements are firstly averaged according to formula (105) using their statistical uncertainties and then added into the combination. A number of these measurements for the resulting combination should be minimal.

The H1 Q^2 binning has been mainly used for a construction of the common grid because the ZEUS measurements take place only for $Q^2 \geq 24$ GeV^2. For the kinematic range $24 \leq Q^2 \leq 110$ GeV^2 where the measurements from both experiments take place, x bins were obtained as

$$x = \frac{Q^2_{\mathrm{H1}}}{y_{\mathrm{ZEUS}} s_{460}}, \tag{127}$$

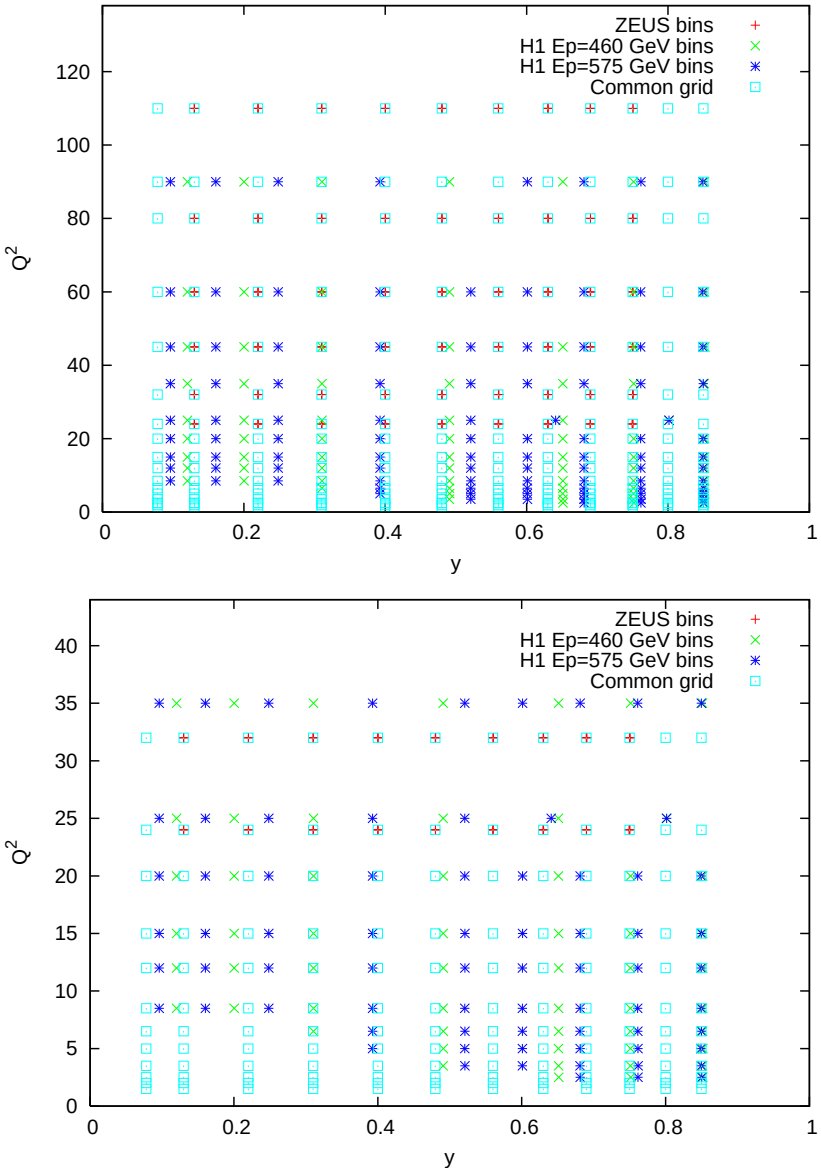

Figure 28: The figure shows the H1 and ZEUS bin centers for measurements together with bin centers of the developed common bin grid for the combination procedure. The ZEUS bins correspond to the measurements at $E_p = 460, 575, 920$ GeV, whereas the H1 bins indicate the measurements for $E_p = 460, 575$ GeV. The bottom plot shows the lower part of the top one.

where $s_{460} = 4E_e$ 460 GeV is the center-of-mass energy (CME) squared corresponding to the proton beam energy $E_p = 460$ GeV. Nevertheless, a few lowest Q^2 bins from ZEUS replace the nearest H1 bins in the common grid in order to describe the most important ZEUS lowest Q^2 measurements without corrections.

The obtained common bin grid and the H1 and ZEUS (y, Q^2) bins for data $E_p = 460, 575$ GeV^2 are shown in Figure 28 by their bin centers. The developed common grid satisfies the specified requirements and allows us to obtain good results of the combination of the published H1 and

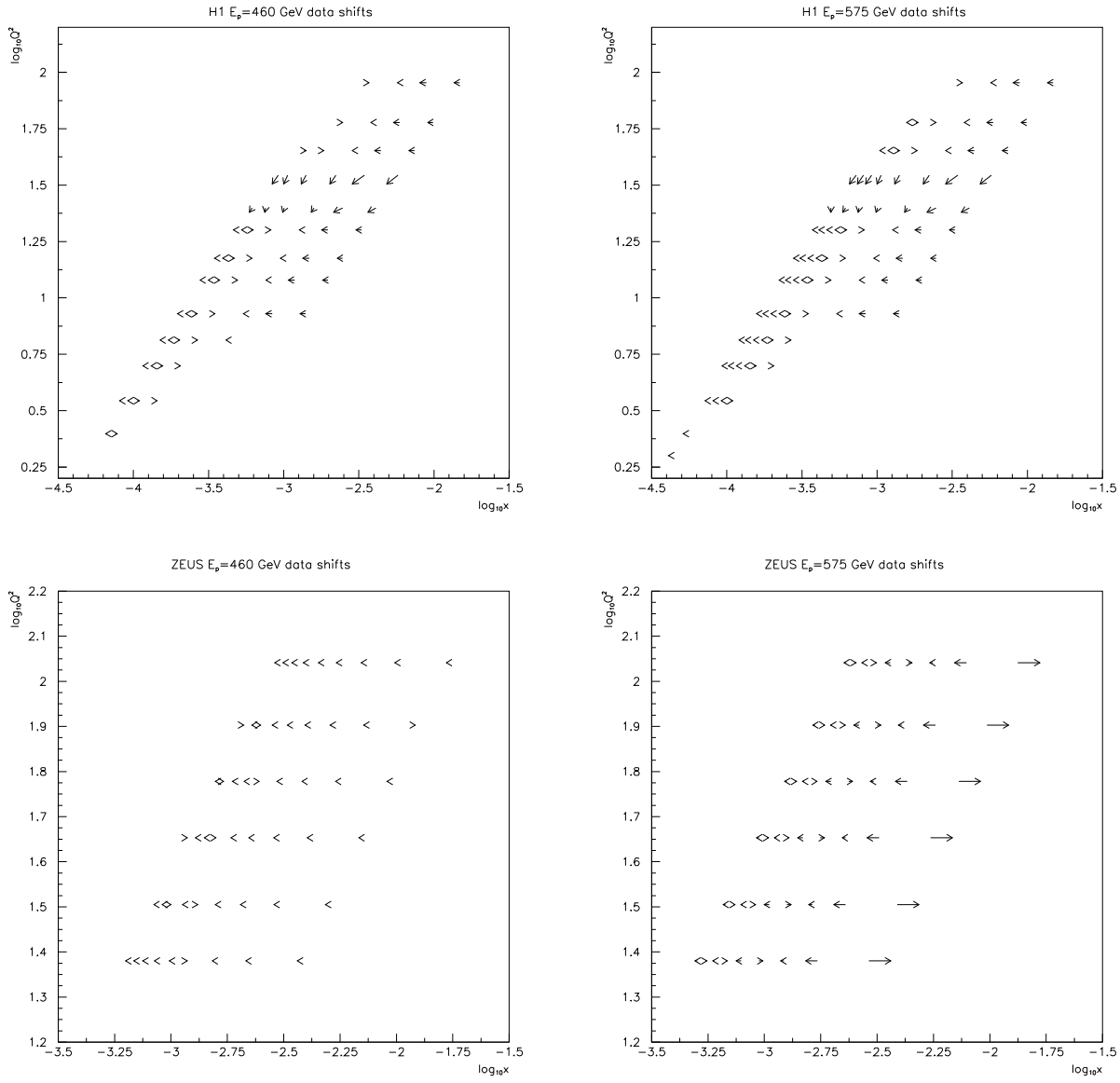

Figure 29: The movements of the original bin centers of the H1 and ZEUS reduced proton beam energy data to the commons grid bin centers.

ZEUS cross section data. Although in this analysis we used only the published ZEUS reduced proton beam energy data, the developed common grid can also be used for a combination of the currently analyzed ZEUS data with $Q^2 < 24$ GeV^2.

The movements of the original bin centers of the cross section data to the common bin centers are shown in Figure 29. All movements except one set of $E_p = 575$ GeV^2 for the ZEUS experiment are relatively small. Since the larger shifts correspond to high x bins and thus to low y values, it does not affect the accuracy of F_L extraction.

6.2 The combination of the H1 and ZEUS $E_p = 460, 575$ GeV data

A combination of the H1 and ZEUS reduced proton beam energy cross section data have been performed by averaging of the datasets for two different proton beam energies $E_p = 460, 575$ GeV. Four HERA II published datasets have been used in this combination.

To increase the number of resulted data points the combination of the H1 and ZEUS $E_p = 460, 575$ GeV cross section measurements is performed at the same common CME. For this purpose, the CME correction of the cross sections to the common CME $\sqrt{s} = 251$ GeV is done. This CME correction is performed only in the kinematic range corresponding to small reference $y < 0.35$, where the contribution of the structure function F_L into the cross section is small. The reference y is chosen to be at the proton energy $E_p = 460$ GeV as $y = Q^2/(xs_{460})$. For higher inelasticities the measurements are taken separately in the combination procedure.

The swimming corrections are based on the HERAPDF1.0 predictions, which are obtained as the results of the NLO DGLAP QCD fit in the ACOT scheme to the previously published combined HERA I inclusive cross section data. The fit describes these data well in the entire kinematic region and allows us to obtain the theoretical cross sections for the initial and common grid bins.

The systematic uncertainties are considered as uncorrelated across experiments. At HERA, the systematic uncertainties are proportional to central values and the additive treatment of the uncertainties leads to a bias of averaged results. This bias depends on different factors and the main factor is the magnitudes of the systematic uncertainties of initial data. It is possible to show that for sufficiently large systematic uncertainties the bias is about 1%. This fact is presented in Figure 30. The left figure shows the scale of the total uncertainty used for obtaining the bias of about 1%. The uncorrelated and correlated systematic uncertainties are taken equal to about 5%, whereas the statistical uncertainty equals to 2%. The right figure shows the bias obtained from averaging of two test datasets. It is clearly seen that the results of averaging using the additive treatment of the systematic uncertainties are shifted for about 1% compared to results obtained with multiplicative treatment. Therefore, the correct treatment of the uncertainties is important for averaging of the HERA cross section data.

Different treatment of the systematic uncertainties is studied to estimate the sensitivity of the averaged results. The additive treatment of the systematics is defined by the standard combination procedure using the formula (122). The additive treatment is used as a check, whereas the multiplicative treatment of the systematic uncertainties is used by default. Although the convergence of the iterative procedure for this case is observed already after the second step, 5 iterations have been performed. The results of the combination in terms of the χ^2/ndf with different treatments of the uncertainties are listed in the Table 7. It shows that the low energy data are consistent between the experiments. The sizable increase of ndf for the resulted combination of the data for both proton beam energies is an effect of the CME correction. The ndf

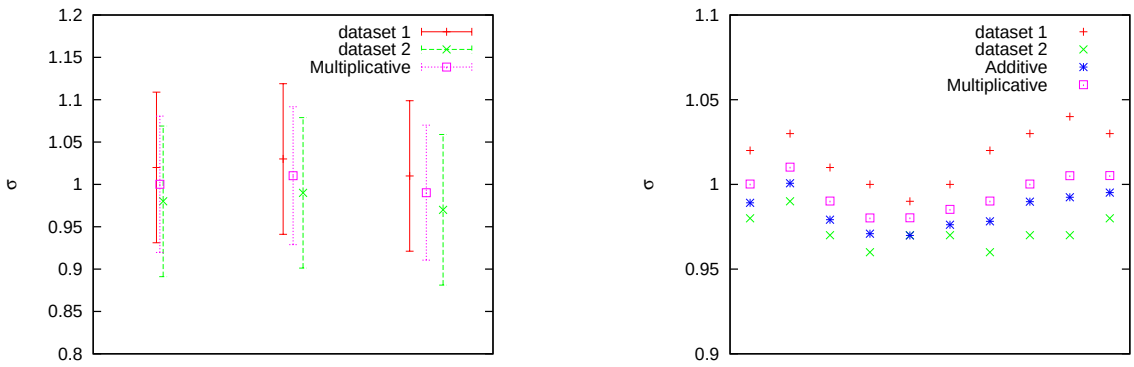

Figure 30: The left figure shows the magnitude of the total uncertainty of initial test datasets 1 and 2 in order to obtain the bias of averaged data of about 1%. The right figure shows the systematic bias of the averaged data if the systematic uncertainties are treated as additive (blue stars) compared to the results with the multiplicative treatment of uncertainties (pink squares).

E_p, GeV	460	575	460/575
Additive	28.72/20	14.84/21	70.04/72
Multiplicative	29.91/20	15.26/21	73.58/72

Table 7: The χ^2/ndf of the H1 and ZEUS published reduced proton beam energy cross section data combination. The combination is performed for separate and both proton beam energies $E_p = 460, 575$ GeV with the additive and multiplicative treatment of the uncertainties.

is defined in the combination as

$$ndf = N_F - N_C, \tag{128}$$

where N_F is the full number of data points from all experiments and N_C is the number of common bins filled by measurements. For the given combination $N_F = 271$ and $N_C = 199$.

The ambiguities in the treatment of the uncertainties have been considered and resulted in the three additional *procedural uncertainties*. The first one is related to the multiplicative and additive treatment of the uncertainties. At HERA, the systematic uncertainties are generally proportional to the central values, therefore in the combination all systematic uncertainties are treated as multiplicative (108). However, it holds unambiguously only for the normalization (luminosity) uncertainty and might be not correct for other uncertainties. In order to study a behavior of the averaged cross sections in relation to the additive treatment of the non-normalization uncertainties an additional averaging has been performed. It was obtained that the mean difference of the cross sections for the described combination and default combination is about 0.3%, and does not reach 0.6%, except one bin with the difference 1.5%. The ratios of the cross sections for these combinations are shown in Figure 31.

The second procedural uncertainty is related to correlations of the uncertainties between the experiments. Due to the similar methods of the calibration and reconstruction of kinematics, it is possible that the uncertainties of the hadron energy scale, electron energy scale and scattered

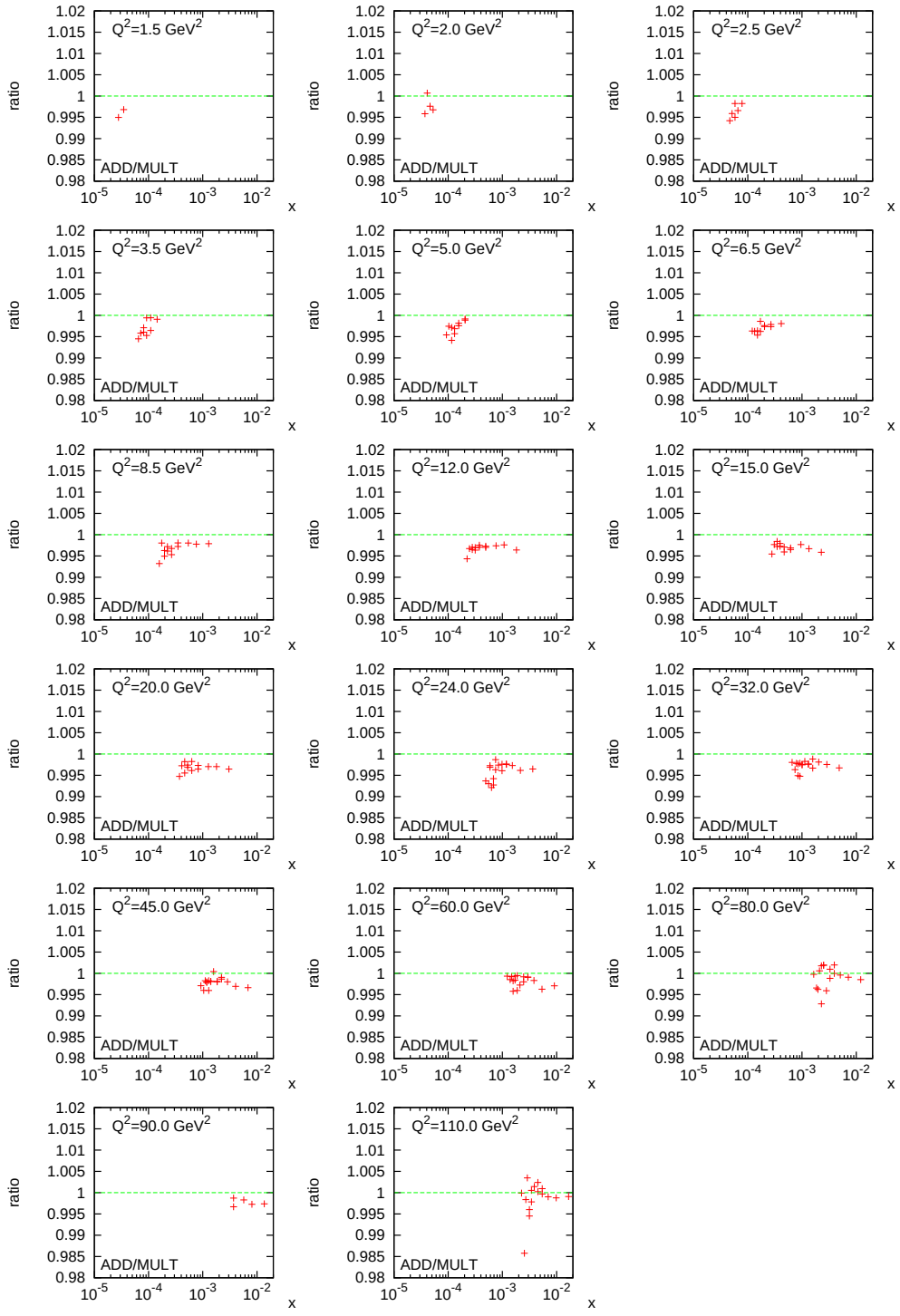

Figure 31: The ratios of the combined cross sections obtained treating all non-normalization systematic uncertainties as additive (ADD) to the cross sections obtained in the default combination (MULT).

electron position are correlated between the experiments. As a test, the introduction of this correlation for the electron and hadron energy scales as well as for the electron scattering angle and X,Y positions did not improve the combination results. A study of possible correlations of these sources between the experiments has revealed that the changes of the resulted cross sections are mainly caused by the electron energy scale systematic source. Nevertheless, the mean change is rather small, namely 0.4%, whereas the maximum 2.6% is reached in one bin.

The third procedural uncertainty originates from a study of correlations of systematic sources having a significant influence on the total χ^2. The shifts of the point-to-point correlated uncertainties are given in the Table 8. There are no large shifts of the H1 systematic sources and only four ZEUS sources have substantial shifts. They are the photoproduction background, electron energy scale, the MVD hit finding efficiency and the luminosity. A study of the point-to-point correlations of these sources treating them as uncorrelated showed that the significant change of the combination results at about 0.7% for most of the cross sections is achieved in case of uncorrelated treatment of the electron energy scale. This source may have a significant uncorrelated component, not reported by the experiment. Therefore, treating the electron energy scale in ZEUS as point-to-point uncorrelated is added as additional procedural uncertainty. It is estimated as a difference in the central values of the average for the correlated and uncorrelated treatment. The difference of the cross sections for this combination and default combination is added as the third procedural uncertainty in the combination in addition to previous ones.

The impact from a contribution of each data point into the total χ^2 is studied using the difference between a given data point and the averaged value. For this purpose the special quantity called pull $p^{i,e}$ can be defined as

$$p^{i,e} = \frac{\mu^{i,e} - \mu^{i,ave}\left(1 - \sum_j \Gamma^{i,e}_j b_{j,ave}\right)}{\sqrt{\Delta^2_{i,e} - \Delta^2_{i,ave}}}, \tag{129}$$

where $\Delta^2_{i,e}$ ($\Delta^2_{i,ave}$) is the statistical and uncorrelated systematic uncertainty added in quadrature for the experiment e (the average value). The distributions of pulls for $E_p = 460$ GeV and $E_p = 575$ GeV data are presented in Figure 32. There are no bins beyond the range of the histograms and thus the Gauss-like distributions show absence of tensions for the averaged data.

In conclusion, it is worth presenting the plots of initial and combined data points. These data are shown in Figures 33-35 by different colors. The plots show that the ZEUS data take place only for $Q^2 \geq 24\,\mathrm{GeV}^2$. Nevertheless, the H1 cross section data change slightly even for Q^2 ranges without ZEUS data due to shifts of the correlated systematic uncertainties. The reduction of total uncertainties is also clearly seen for the regions where measurements for both experiments are present. Additionally, the combined data are listed in Table 23 in Appendix.

Experiment	Systematic source	shift	uncertainty
H1	SpaCal electromagnetic energy scale	0.31	0.74
	Electron scattering angle	-0.20	0.87
	Calorimeter hadronic energy scale	0.26	0.99
	LAr calorimeter noise	0.16	0.99
	Background charge asymmetry	0.14	1.00
	Electron tagger acceptance	0.15	1.00
	Luminosity 460	-0.19	0.51
	Luminosity 575	-0.34	0.51
ZEUS	Photoproduction background	0.94	0.93
	Electron energy scale	1.16	0.49
	Hadron energy scale	0.67	0.78
	Electron finding efficiency	0.44	0.90
	X position	-0.02	0.63
	Y position	0.20	0.86
	MVD hit finding efficiency	1.32	0.54
	CTD hit finding efficiency	-0.73	0.68
	Scale factor	0.45	0.98
	Luminosity 460/575	0.33	0.79
	Luminosity 460	0.94	0.76
	Luminosity 575	-0.79	0.77

Table 8: Shifts of the central values and the obtained reductions of uncertainties of the systematic error sources during the combination of the reduced proton beam energy E_p = 460, 575 GeV data. The shifts are expressed in units of one standard deviation. The reductions are given as a fraction of the original uncertainty.

6.3 Results of the fit

6.3.1 DGLAP fit

The QCD fits to the combined H1 and ZEUS reduced proton beam energy data together with the previously published combined inclusive HERA I NC and CC cross section data [47] have been performed. The DGLAP evolution equation in the RT and ACOT heavy flavour number schemes has been used for a calculation of the theory predictions. The initial fit conditions are explicitly described in Chapter 2. The minimum Q^2 cut is chosen to be $Q^2 = 3.5$ GeV^2 as prescribed in [47] and the parametrization (70) with 10 as well as 13 fitted parameters is used. The fits have been performed at NLO in QCD.

The quality of the fits in terms of χ^2/ndf depending on the heavy-flavour scheme is given in Table 9. It is clearly seen from the table that the DGLAP fit in the ACOT scheme gives better description of the data with overall $\chi^2/ndf = 868.12/769$ for 10 parameter fit and $\chi^2/ndf = 856.81/766$ for 13 parameter fit than the DGLAP fit in the RT scheme. Therefore, the ACOT fit has been chosen for further investigation.

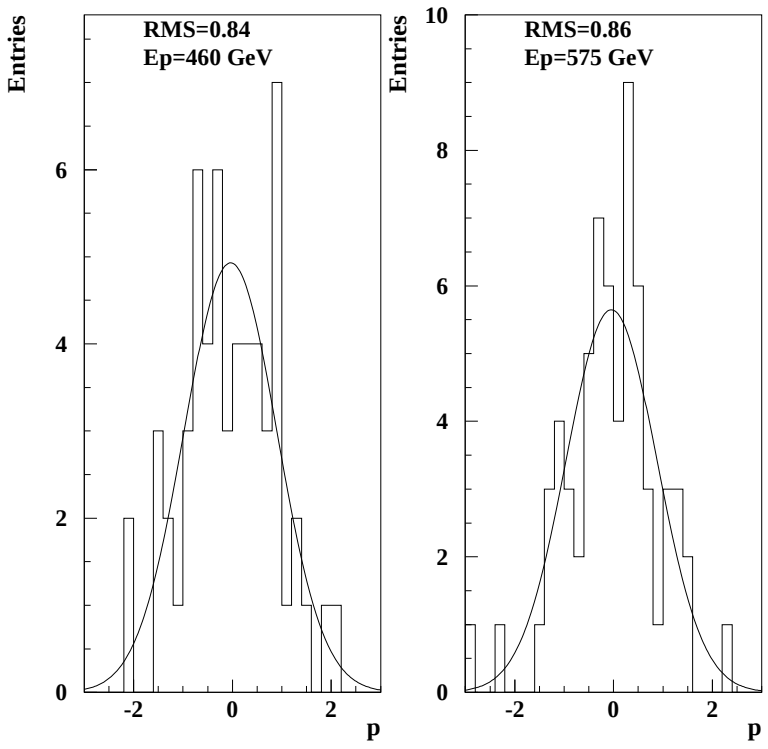

Figure 32: The distribution of pulls (129) for the H1 and ZEUS cross section data samples with $E_p = 460, 575$ GeV. The binned log-likelihood Gaussian fit for the distribution is also shown. The presented RMS gives the root mean square of each distribution.

10 parameters		
HF scheme	χ^2/ndf	χ^2/ndf-partial
RT	869.27/769	251.79/187
RT fast	876.01/769	253.05/187
ACOT full	868.12/769	249.06/187
13 parameters		
HF scheme	χ^2/ndf	χ^2/ndf-partial
RT	869.27/766	248.37/187
RT fast	861.54/766	241.64/187
ACOT full	856.81/766	241.93/187

Table 9: The quality of the NLO DGLAP fits in terms of χ^2/ndf. 10 and 13 parameter fits using the HERA parametrization are used. χ^2/ndf-partial corresponds to a quality of the fit for studied combined reduced proton beam energy dataset.

In order to justify the choose of the used parametrization the scan of these parameters have been performed. The starting point for the scan was the parametrization with 9 free parameters (70) A_q, B_q, C_q. The fits to data have been done introducing the D_q and E_q parameters

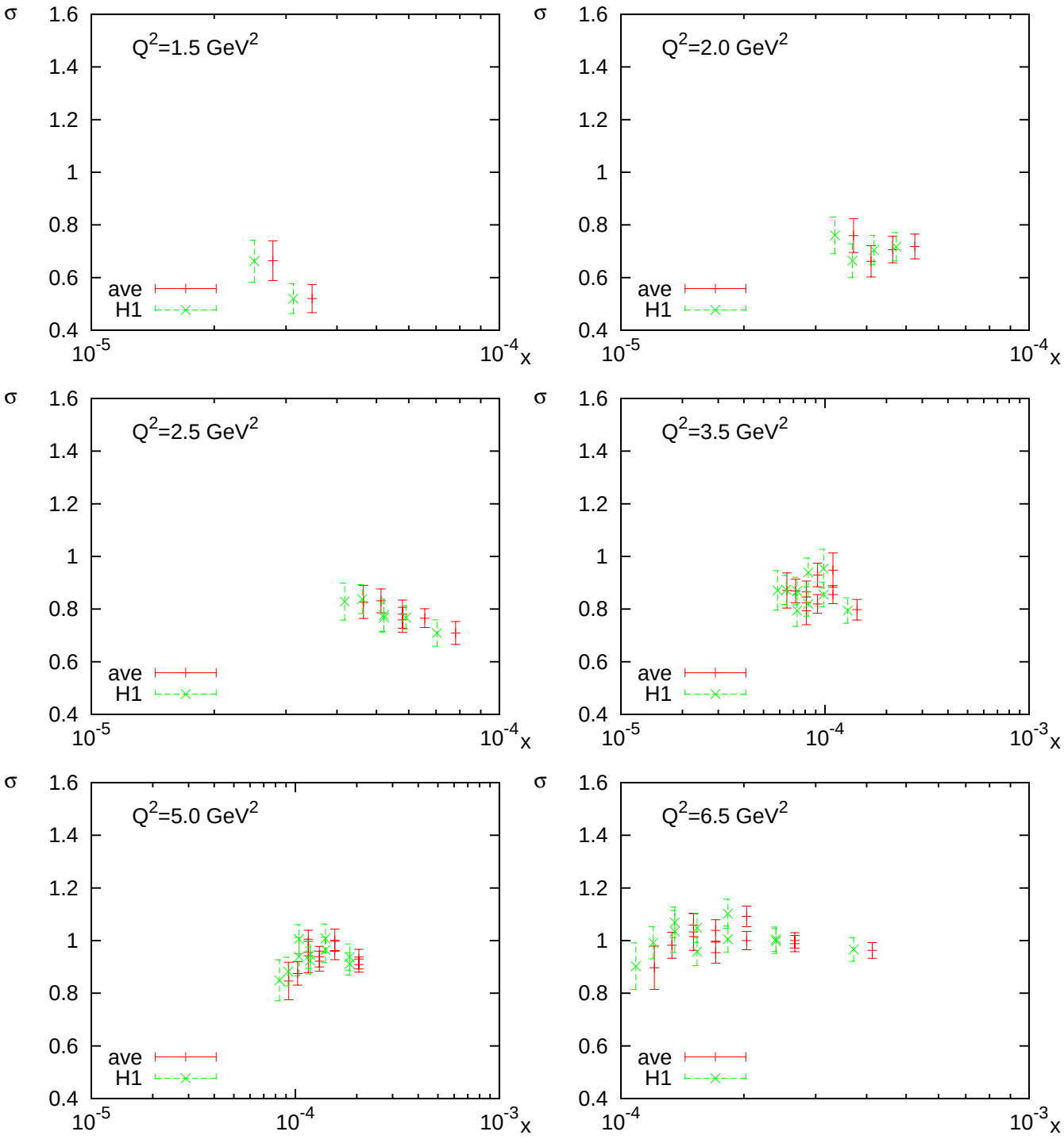

Figure 33: The combined reduced cross section data together with the initial H1 and ZEUS $E_p = 460, 575$ GeV measurements. The red ticks correspond to combined data. The total uncertainty for data points is shown.

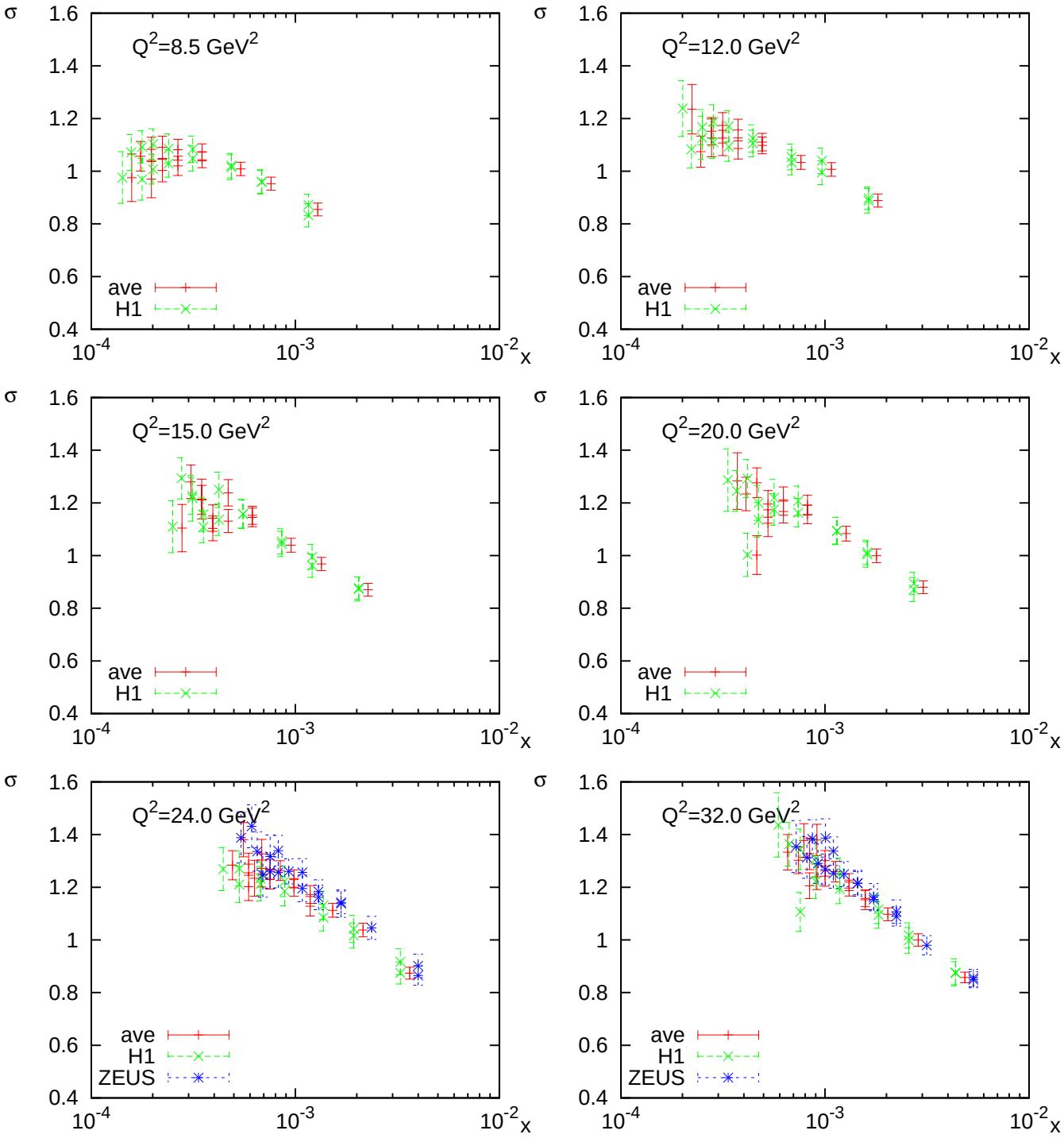

Figure 34: The continuation of Figure 33.

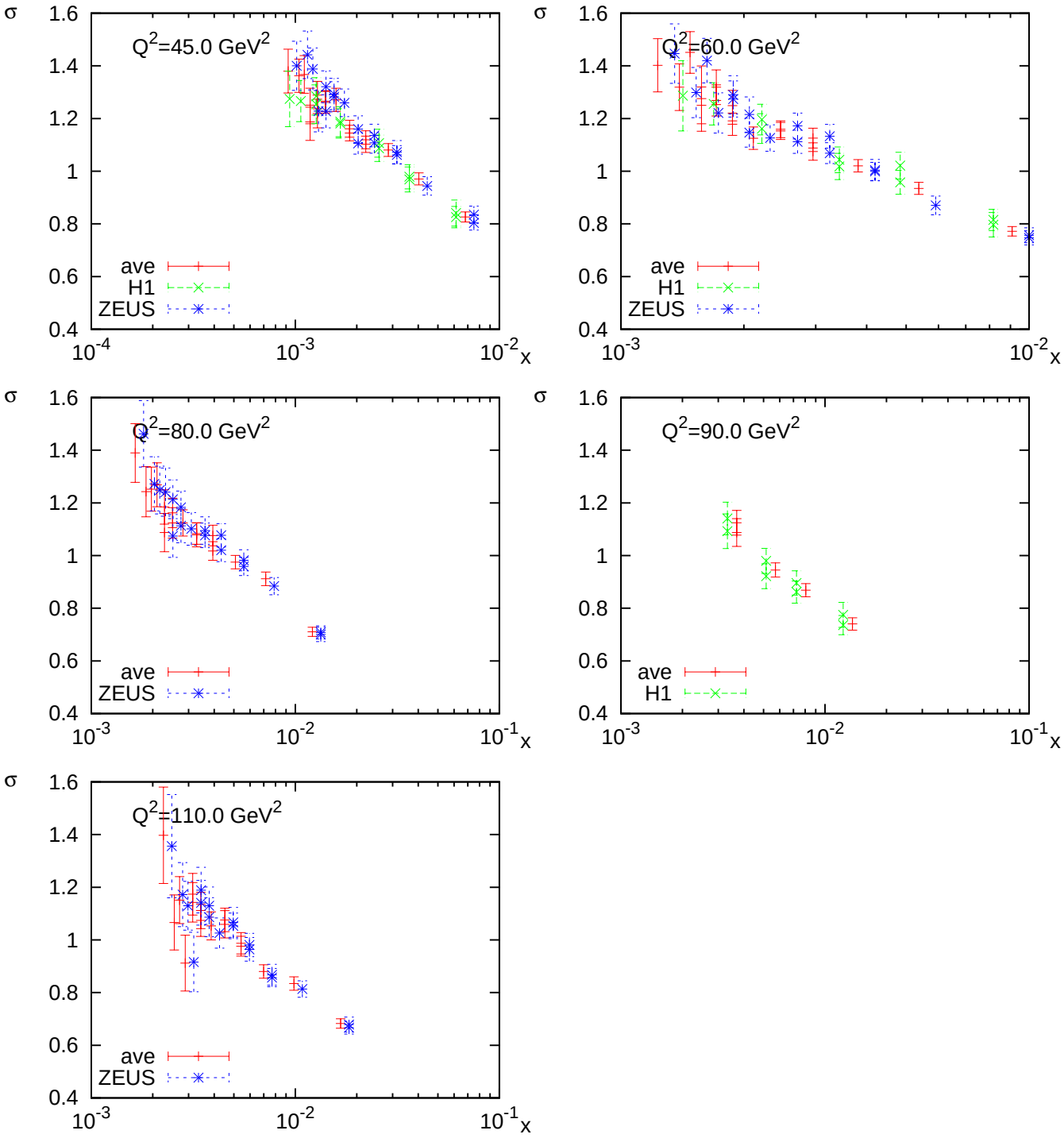

Figure 35: The continuation of Figure 33.

for the parton densities one at a time. A significant improvement in χ^2/ndf of the fit has been found if E_{u_v} parameter is added to the fit. The fit has $\chi^2/ndf = 862.67/769$ and the resulted value $E_{u_v} = 11.094$, whereas the fit with 9 parameters gave 905.91/770. The next point was to add the eleventh free parameter to the parametrization. There was no significant reduction of the χ^2 except during making the parameter $D_{\overline{U}}$ to be free. However, it produces the noticeable distortion of the $\overline{U}$ distribution in the high x region. Also this change violates the valence quark condition $xd_v > x\overline{d}$ and therefore the addition of further parameters can not be considered as an improvement.

Removing the condition $B_{u_v} = B_{d_v}$ and using flexible gluon parametrization (72) with free parameters A' and B' improved the resulted χ^2 which became equal to 856.7/766. Nevertheless, in spite of a good χ^2, the flexible gluon parametrization explicitly allows for a negative gluon contribution at the starting scale. This can be seen in Figure 36, which shows the fitted PDFs at the starting scale and, in particular, the gluon distribution is negative at small x. At larger scales, the gluon distribution is positive but inherits a small inflexion at low x.

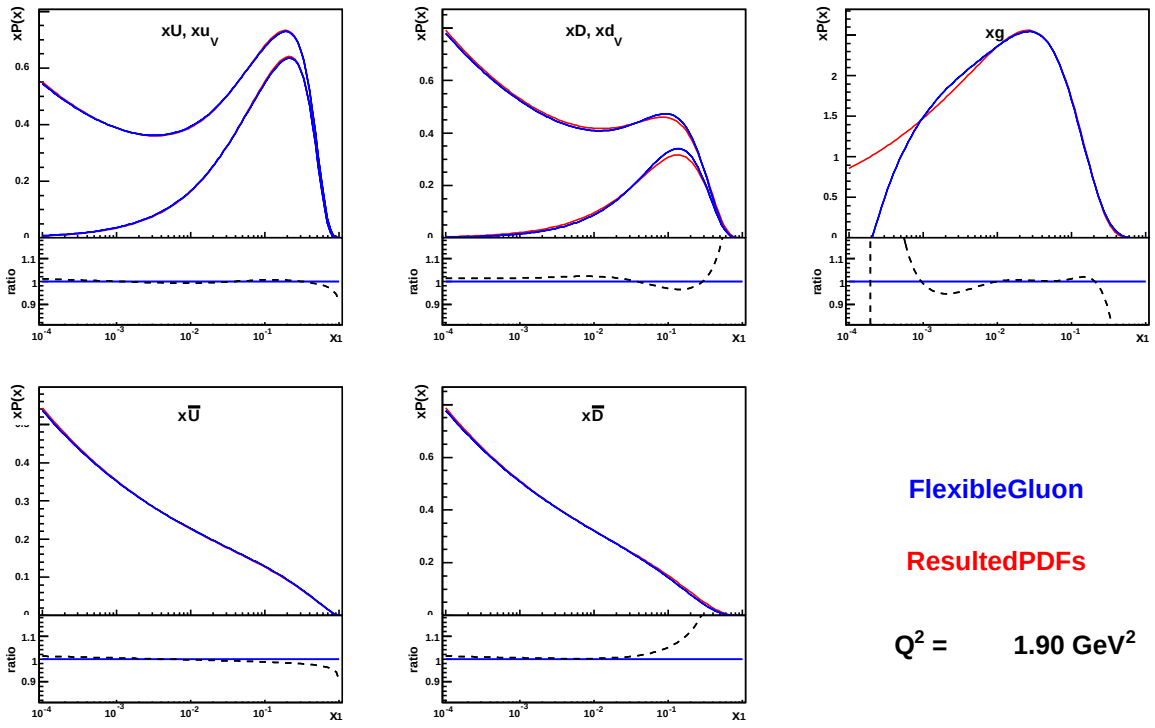

Figure 36: The PDFs extracted from the NLO DGLAP fit to the combined HERA I and combined reduced proton beam energy $E_p = 460, 575$ GeV data at the starting scale $Q^2 = 1.9$ GeV^2. The red curve shows the PDFs obtained using the resulted parametrization. The blue curve in turn shows the PDFs extracted using the flexible gluon parametrization (72). The gluon distribution becomes negative at low x. The bottom panel shows the ratios of the extracted PDFs using the resulted parametrization to the PDFs obtained with the flexible gluon parametrization.

As a result, the obtained parametrization is identical to original HERAPDF1.0 [47] parametriza-

tion and includes 10 fitted parameters (see equation(71)). Using this parametrization in the fit one obtains all positive PDFs and a good description of the data with $\chi^2/ndf = 862.67/769$. The fitted values for the parametrization are listed in Table 10. The combined reduced proton beam energy data compared to the NLO DGLAP fit in the ACOT scheme are shown in Figures 37-39.

PDF	A	B	C	E
xg	7.86	0.241	9.14	
xu_v	4.15	0.690	5.05	11.09
xd_v	2.42	0.690	4.49	
$x\overline{U}$	0.096	-0.187	1.59	
$x\overline{D}$	0.141	-0.187	3.40	

Table 10: The fitted parameters of the used parametrization obtained after a NLO QCD fit to the combined HERA I and combined $E_p = 460, 575$ GeV datasets.

While the quality of the central fit is satisfactory, its χ^2/ndf is not very good corresponding to consistency probability of about 1%. The tensions between data and theory may arise at low Q^2 where DGLAP description of the data may break down. The sensitivity of the fit to inclusion of low-Q^2 data has been studied by varying the minimum-Q^2 cut. The variation of the fit quality in terms of χ^2/ndf is presented in Table 11. The partial χ^2/ndf for the combined reduced proton beam energy data is also given. The difference between the data and calculated theory predictions becomes larger at low Q^2 and decreasing of the minimum-Q^2 cut leads to increase of χ^2/ndf. It means that the fit has some difficulties to describe low-Q^2 data and the preservation of conventional minimum $Q^2 = 3.5$ GeV^2 cut is reasonable.

The comparison of the extracted PDFs for the data including the combined reduced E_p data and for HERA I data only at two different scales is shown in Figure 40. It is clearly seen that the main difference consists in larger gluon distribution for medium and low x for different Q^2 scales. Other PDFs do not undergo any sufficient changes for all values of x, but they are slightly decreased at low x. As a result, the addition of low-x data does not introduce any substantial changes in the PDFs except the gluon distribution.

The comparison of the total uncertainties of the extracted PDFs shows an improvement in precision of the gluon distribution for low x and low Q^2. These plots are presented in Figure 41. It is better seen for the starting scale $Q^2 = 1.9$ GeV^2, while for higher values of Q^2 the reduction of uncertainties is smaller.

A check of the combination procedure has been performed by applying the DGLAP fit to the combined data compared to the original uncombined data from the H1 and ZEUS collaborations. The parameters of the PDFs extracted in the DGLAP fits to uncombined data are presented in Table 12. The obtained values of the fitted parameters are similar to values in Table 10. It means that the PDFs extracted from fits to uncombined and combined data are the

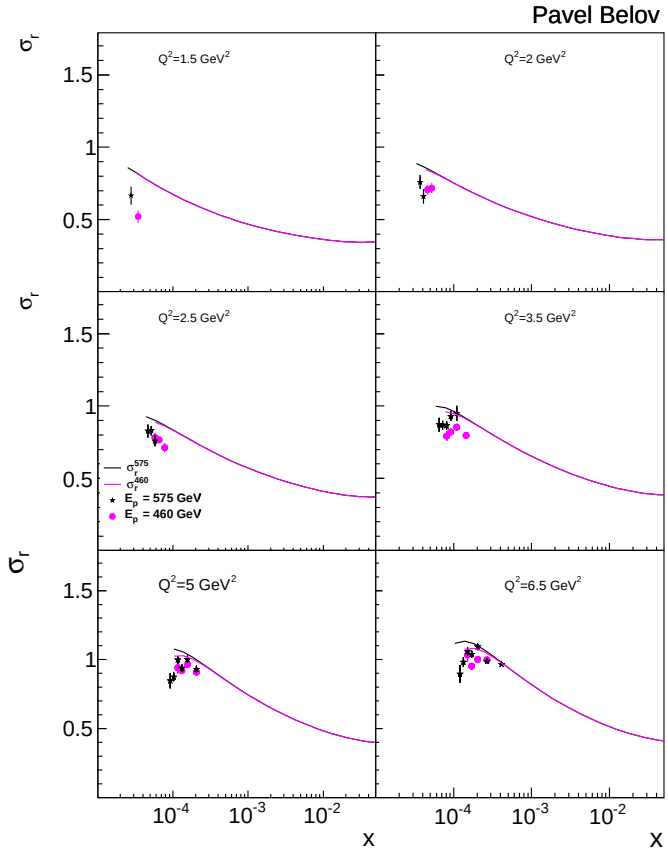

Figure 37: The reduced proton beam energy $E_p = 460, 575$ GeV cross section data as a function of x for different values of Q^2. The solid lines present the results of the NLO DGLAP fit in the ACOT scheme to the combined reduced proton beam energy together with the HERA I NC data. The data with Q^2 below 3.5 GeV^2 were excluded from the fit.

same, the combined data are consistent and the combination does not introduce a distortion in the results of DGLAP fits. The uncertainties of the extracted PDFs also did not change. It is confirmed in Figure 42, where the total uncertainties of the PDFs for performed fits as well as the ratios of the PDF central values are shown.

Q^2_{min}, GeV^2	1.5	2.0	2.5	3.5	5.0
χ^2/ndf	979.7/824	935.1/808	891.5/791	862.7/769	797.3/734
χ^2/ndf-partial	269.8/199	264.8/197	258.2/193	249.4/187	227.0/178

Table 11: The quality of the NLO DGLAP fits in terms of χ^2/ndf with respect to variation of the minimum Q^2 cut. The partial χ^2/ndf for combined $E_p = 460, 575$ GeV data is also given.

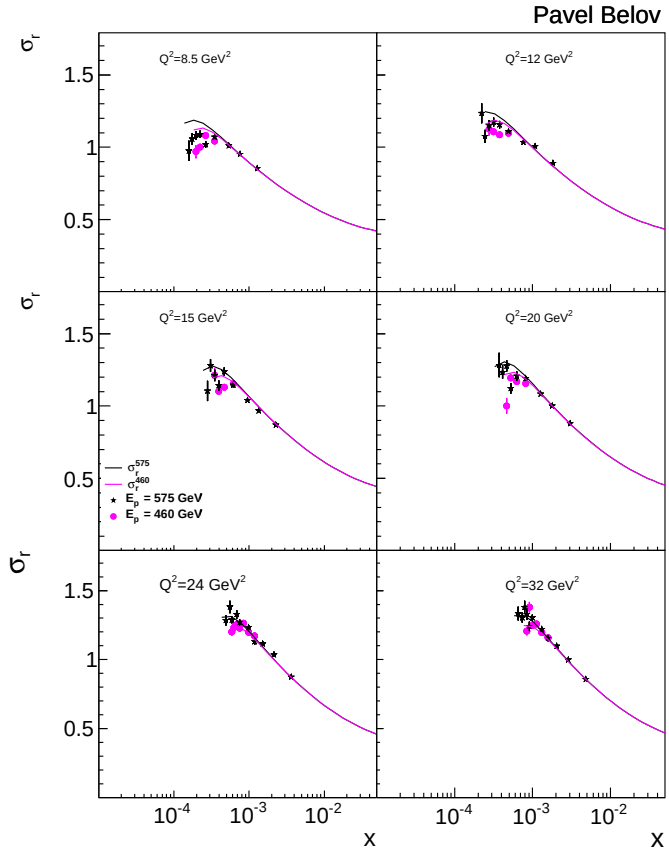

Figure 38: The continuation of Figure 37.

PDF	A	B	C	E
xg	7.87	0.241	9.16	
xu_v	4.16	0.691	5.06	11.15
xd_v	2.42	0.691	4.49	
$x\overline{U}$	0.098	-0.186	1.58	
$x\overline{D}$	0.142	-0.186	3.47	

Table 12: The fitted parameters of the used parametrization obtained after a NLO QCD fit to the combined HERA I and uncombined $E_p = 460, 575$ GeV datasets. The values of parameters are similar to data in Table 10.

6.3.2 Dipole model fits

The dipole models (see Chapter 2 for more details) are based on the one-photon exchange and therefore describe only NC data. They are applicable at $x < 0.01$ where the gluon and sea quark densities dominate. The dipole model fits to combined H1 and ZEUS reduced proton beam energy data together with the previously published inclusive HERA I NC cross section data

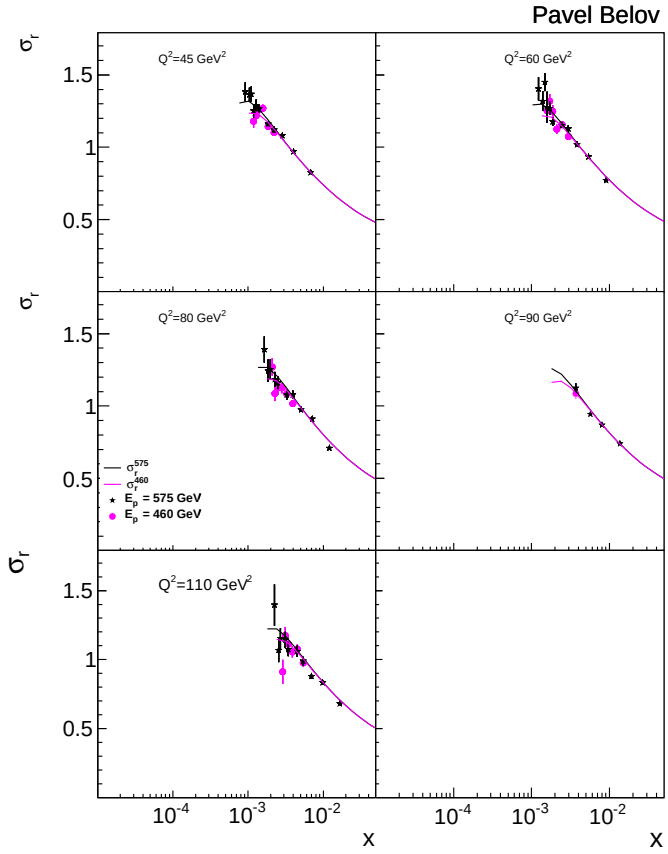

Figure 39: The continuation of Figure 37.

have been performed in this kinematic region. Three dipole models were under consideration. The original GBW and IIM dipole models are valid down to $Q^2 \approx 0$, therefore no Q^2 cuts have been applied for these fits. In contrast, the BGK dipole model incorporates the DGLAP evolution of the gluon distribution and is applicable only in the restricted kinematic region $Q^2 > 3.5$ GeV^2, where the DGLAP evolution equations are valid. Therefore, the BGK dipole model fits to data have been performed in this restricted kinematic region. It is also interesting to see how the GBW and IIM dipole models describe the data in this restricted kinematic region. Thus, all dipole model fits have been performed for $x < 0.01$ and $Q^2 > 3.5$ GeV^2.

The fitted parameters and χ^2/ndf values for the entire kinematic region are listed in Table 13, whereas the results for the restricted kinematic region are presented in Table 14. The results of the fits show that the dipole models describe the data with different level of accuracy. It was found that the GBW dipole model leads to very poor value of χ^2/ndf, while the IIM dipole model can describe the data relatively well with $\chi^2/ndf = 709.8/540$ for the fits performed without Q^2 cut. The values of the model's parameters were found to be similar to the

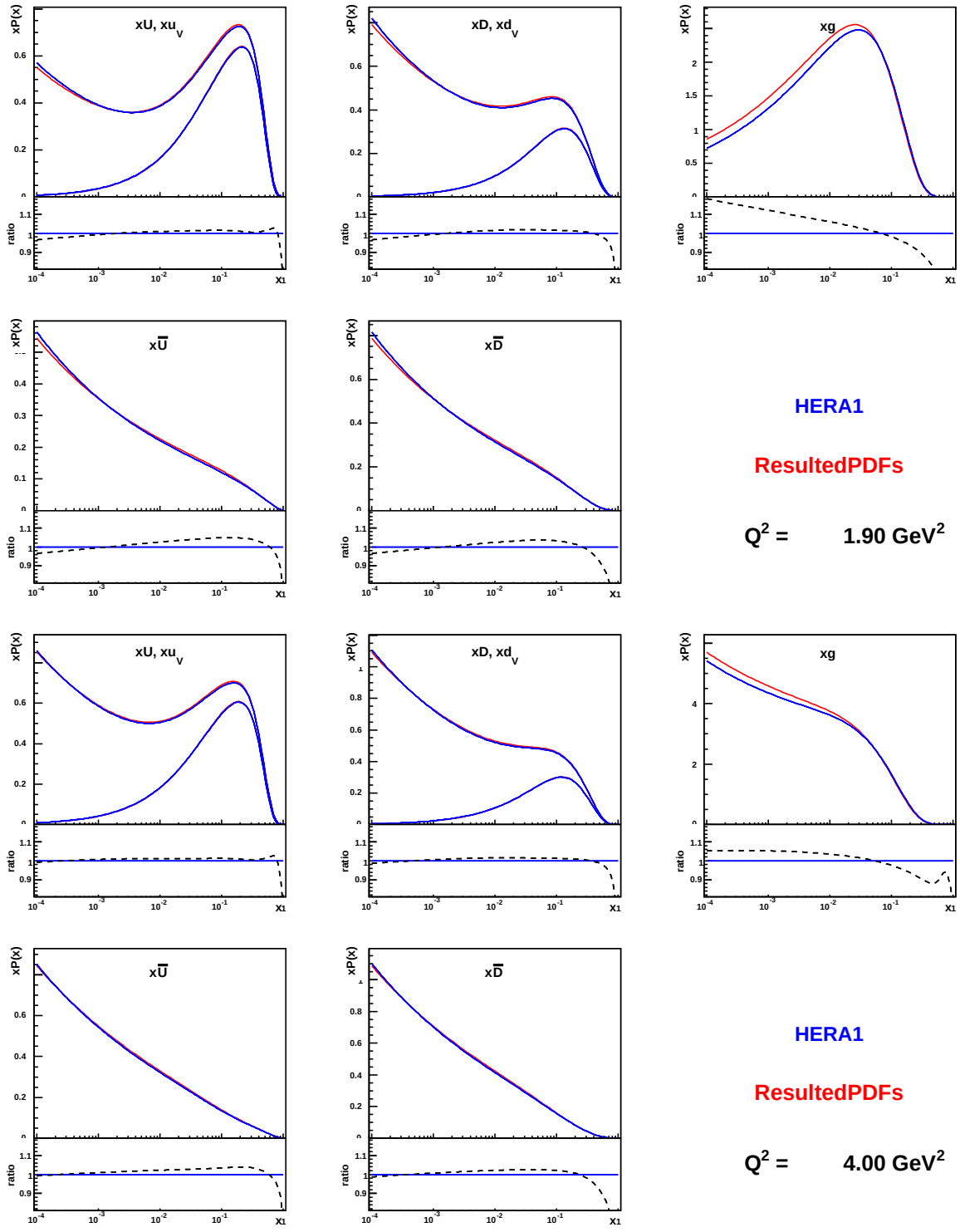

Figure 40: The comparison of the extracted PDFs from the fit to HERA I data including the obtained combined measurements and to HERA I data only at two different scales $Q^2 = 1.9, 4.0$ GeV^2. The bottom panel shows the ratio of these PDFs.

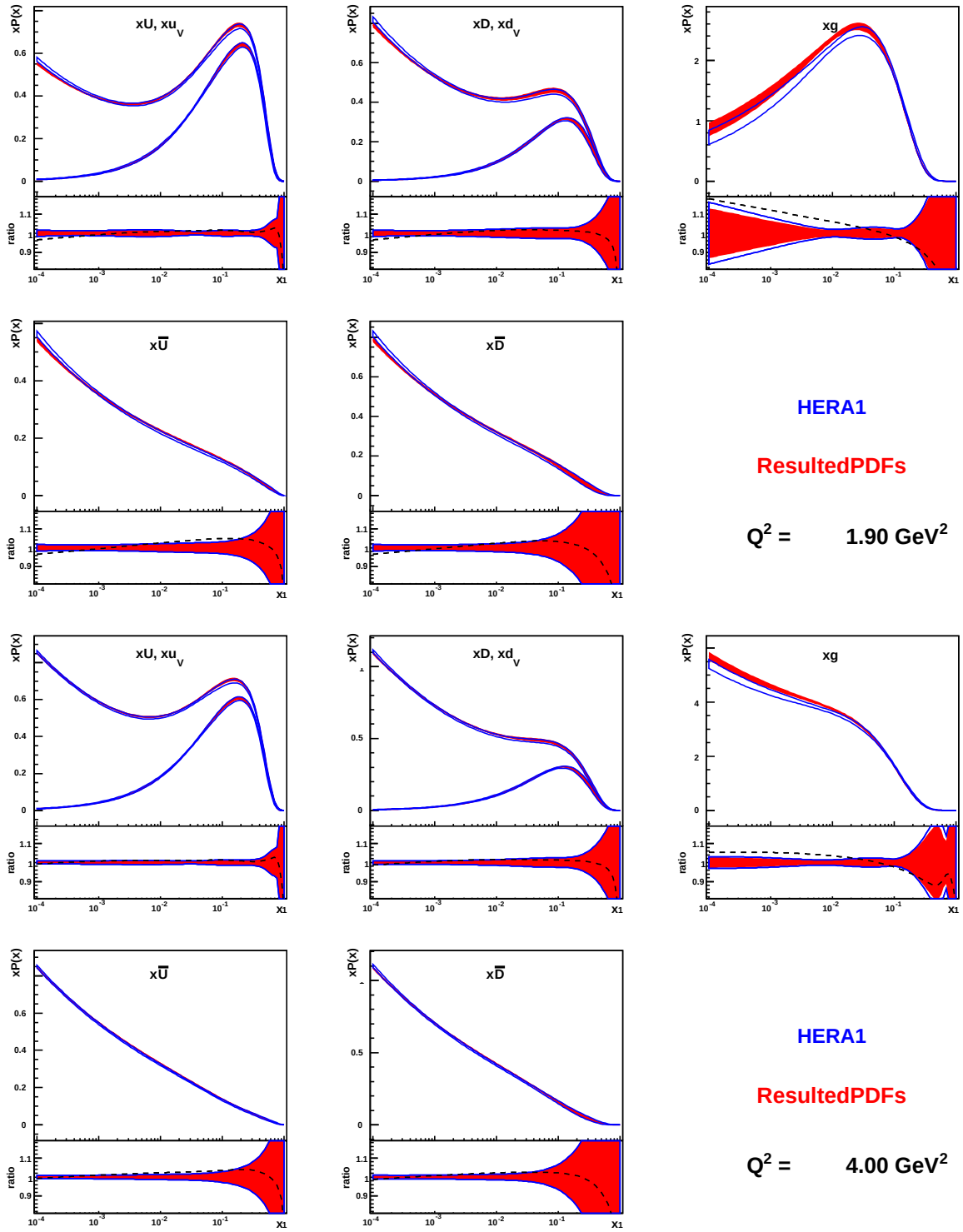

Figure 41: The comparison of the total uncertainties of the extracted PDFs for the combined data and for HERA I data at two different scales $Q^2 = 1.9, 4.0\,\mathrm{GeV}^2$. The bottom panel also shows the ratio of the PDF central values.

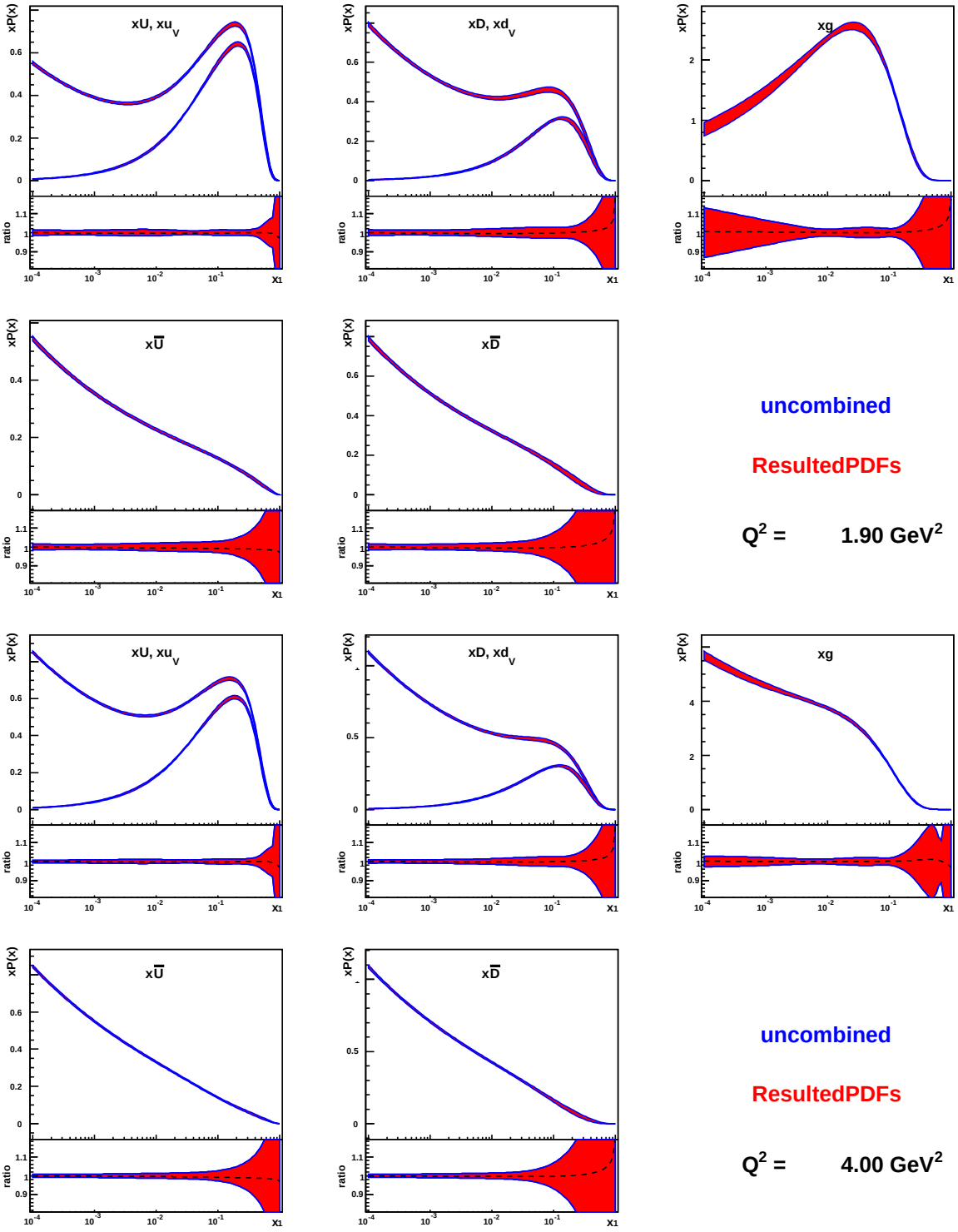

Figure 42: The comparison of the uncertainties of the PDFs extracted from the DGLAP fits to obtained combined reduced proton beam energy data and uncombined reduced proton beam energy data at two different scales $Q^2 = 1.9, 4.0\,\mathrm{GeV}^2$. The identity of the results is clearly shown. The dashed line in the bottom panel shows the ratio of the PDF central values.

values obtained in the previous fits [84]. The combined reduced proton beam energy run data together with IIM fit curves for all Q^2 are shown in Figures 43-45. The extrapolation of fitted curve to the $x > 0.01$ kinematic region is shown by the dashed line.

For the restricted kinematic region, the BGK dipole model shows the best description of the data with $\chi^2/ndf = 444/380$. The NLO DGLAP fit to data has been used for determination of the parameters for the gluon density at the starting scale. The coupled DGLAP evolution of the gluon and sea quark distributions was performing during the dipole model fit in order to obtain the gluon density at different scales. The parameter C_{BGK} was taken to be 4 GeV^2. As a result, the BGK model is best suited for the description of the combined reduced proton beam energy. The very good fit results obtained in the present work are confirmed by recent studies [96]. It is also interesting that the parameters of the IIM dipole model are almost the same for the fits in the restricted and entire kinematic regions.

The DGLAP fits show that the contribution of the valence quarks varies between 5% and 15% for x varying from 0.0001 to 0.01. However, the dipole models do not take the valence contribution into account assuming it to be negligible. Nevertheless, this contribution can be taken into account in the modified dipole fits. In these fits the contribution from the valence quarks to the cross section is added to the dipole model prediction. The valence contribution has been estimated by the NLO DGLAP fit to the combined reduced energy and previously published combined HERA I data which was performed over the restricted $Q^2 > 3.5$ GeV^2 and $0 < x < 1$ kinematic region. The details of the performed NLO DGLAP fit in the ACOT scheme are described in the previous section. The PDF parameters for a calculation of the contribution from the valence quarks are listed in Table 10.

The results of the dipole model fits with the constant DGLAP valence contribution in terms of χ^2/ndf and the fitted parameters of the dipole models are presented in Table 14. A good description of the data is provided by the IIM and BGK dipole models. With addition of the valence contribution the fitted parameters of these two models have been changed with a significant difference for the x_0 parameter fitted in the IIM+DGLAP$_{\text{valence}}$ fit. The obtained values of the parameters are also similar to the values already obtained in [84]. Comparing the obtained χ^2/ndf's, it is possible to note that the quality of GBW and IIM fits became worse with the addition of the constant valence contribution. Therefore, it does not allow us to state that the addition of the valence contribution to the GBW and IIM dipole model predictions helps to describe the data. However, the addition of the valence contribution improves a quality of the BGK dipole model fit.

The obtained predictions for the BGK dipole model fit with the valence contribution are shown in Figures 46-48. The valence contribution is sizable at medium and high x and makes it possible to improve the description of the data at these x. At low x, the predictions are not significantly changed.

The dipole models provide the predictions for the longitudinal proton structure function F_L.

Predictions obtained from the models in given QCD analysis together with the published values of F_L from [84] are presented in Figure 49. The data are given with the total uncertainties. Unfortunately, relatively large uncertainties of the data do not allow us to decide decisively which prediction is favoured by the data. Nevertheless, it is possible to state that all predictions agree with the data. Moreover, the prediction of the GBW model agrees with the data in spite of moderate fit results. For $Q^2 > 10$ GeV^2 all models agree with the data and IIM model seems to be the best one, but for $Q^2 < 10$ GeV^2 GBW and IIM dipole models predict larger values of F_L than BGK dipole model. The BGK model shows better description of the structure function F_L for small Q^2.

Model	Parameter	Value	
GBW	χ^2/ndf	1526.4/540	
	σ_0 (mb)	20.35	± 0.41
	λ	0.304	± 0.002
	x_0	$2.29 \cdot 10^{-4}$	$\pm 0.19 \cdot 10^{-4}$
IIM	χ^2/ndf	709.8/540	
	R_0 (fm)	0.602	± 0.024
	λ	0.264	± 0.003
	x_0	$0.515 \cdot 10^{-4}$	$\pm 0.044 \cdot 10^{-4}$

Table 13: Obtained fitted parameters, their total uncertainties and the qualities in terms of χ^2/ndf for the GBW and IIM dipole model central fits. The fits are performed without applying any constrains to four-momentum squared Q^2.

6.4 The nominal proton beam energy $E_p = 920$ GeV data

The nominal proton beam $E_p = 920$ GeV cross section data have been examined using the QCD fits and data combination. The used data include H1 reduced cross section data measured with the low Q^2 BST, H1 reduced cross section data measured with the medium Q^2 CJC [84] as well as ZEUS reduced cross section measurements [87]. The separate combination of the only nominal proton beam energy data gives $\chi^2/ndf = 10.13/13$, which implies that there only few data points reported in similar bins. This fact is confirmed in Figure 50, which shows the H1 and ZEUS bin centers and their movements to the common grid bin centers. The data from two experiments correspond to partially overlapping kinematic ranges and thus common (x, Q^2) points are rare. The H1 data concentrate at high y and low Q^2, while ZEUS data extend to low y. These features are driven by the F_L extraction needs: for that H1 uses more accurate data collected in the year 2000 while ZEUS uses this HERA II sample.

A common combination of the H1 and ZEUS data at $E_p = 460, 575$ and 920 GeV gives a good $\chi^2/ndf = 100.3/93$. On the other hand, the DGLAP fit to the uncombined H1 and ZEUS $E_p = 920$ GeV data as well as combined reduced proton beam energy data and combined

Model	Parameter	$\text{DGLAP}_{\text{valence}}$		$Q^2 \geq 3.5$ GeV^2	
GBW	χ^2/ndf	1323.4/382		1214.1/382	
	σ_0 (mb)	17.82	± 0.23	19.30	± 0.17
	λ	0.361	± 0.002	0.309	± 0.002
	x_0	$3.34 \cdot 10^{-4}$	$\pm 0.12 \cdot 10^{-4}$	$2.84 \cdot 10^{-4}$	$\pm 0.40 \cdot 10^{-4}$
IIM	χ^2/ndf	504.4/382		487.1/382	
	R_0 (fm)	0.686	± 0.008	0.603	± 0.006
	λ	0.303	± 0.004	0.264	± 0.003
	x_0	$0.110 \cdot 10^{-4}$	$\pm 0.021 \cdot 10^{-4}$	$0.499 \cdot 10^{-4}$	$\pm 0.046 \cdot 10^{-4}$
BGK	χ^2/ndf	432.0/380		444.3/380	
	σ_0	76.0	± 4.0	119.7	± 7.0
	μ_0^2	5.86	± 1.01	1.44	± 0.07
	A_g	3.68	± 0.56	2.15	± 0.09
	B_g	0.012	± 0.003	0.105	± 0.005
	C_g	16.5	± 1.6	6.0	± 0.6

Table 14: Obtained fitted parameters, their total uncertainties and the qualities in terms of χ^2/ndf of the dipole model fits for restricted kinematic region without and with the constant valence contribution estimated from the DGLAP fit in the ACOT scheme. The fits of both types are performed with a constrain to four-momentum squared $Q^2 \geq 3.5$ GeV^2.

HERA I data shows that the ZEUS data are inconsistent. As it is shown in Table 15, the partial χ^2/ndf for ZEUS dataset is 141.1/54, even though other datasets have reasonable χ^2/ndf's. The presented results of the fit show the existing tensions of the ZEUS $E_p = 920$ GeV data.

Dataset	χ^2/ndf
H1 CJC $E_p = 920$ GeV	19.1/29
H1 BST $E_p = 920$ GeV	29.6/23
ZEUS $E_p = 920$ GeV	141.1/54
Combined $E_p = 460, 575$ GeV	243.1/187
HERA I	561.4/592

Table 15: The partial χ^2/ndf's of the DGLAP in the ACOT scheme fit to the uncombined H1 and ZEUS $E_p = 920$ GeV data as well as combined reduced proton beam energy data and combined HERA I data.

In spite of good results of the combination the uncertainties of the data seem to be poorly understood. Therefore these data cannot be used for further analysis and QCD fits.

As a result, the ZEUS nominal proton beam energy cross section data are excluded and the combination of the $E_p = 460, 575, 920$ GeV data has not been performed.

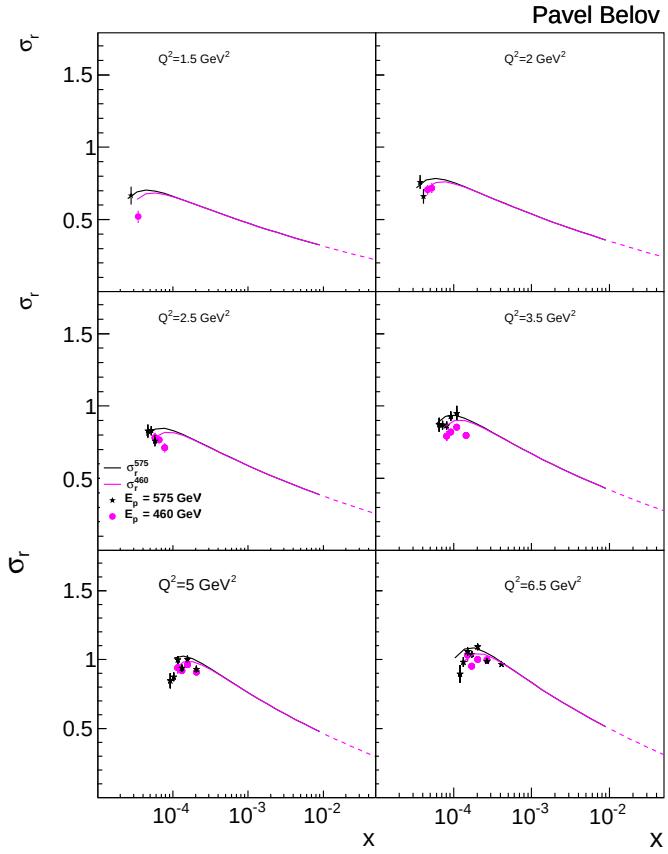

Figure 43: The reduced proton beam energy $E_p = 460, 575$ GeV cross section data as a function of x for different values of Q^2. The solid lines present the results of IIM dipole model central fit to the combined reduced proton beam energy together with the HERA I NC data. No Q^2 cuts have been applied. The extrapolation of fitted curves to the $x > 0.01$ kinematic region is shown by the dashed lines.

6.5 Fits to H1 $E_p = 920$ GeV and combined $E_p = 460, 575$ GeV data

The QCD analysis, similar to that described in Sections 6.3, with an addition of the H1 $E_p = 920$ GeV cross section data has been performed. The input datasets for fits also contain the combined reduced proton beam energy $E_p = 460, 575$ GeV data and combined HERA I NC and CC cross section data [47]. Based on the already performed fits, the DGLAP evolution equation in the ACOT heavy flavour number scheme has been chosen for a calculation of theory predictions.

The scan of parameters has been performed for determination of the appropriate parametrization and obtaining the central values of the parameters. Similar to Section 6.3.1, the resulted parametrization includes 10 parameters (71) and the values of these parameters are listed in tTable 17. The quality of the fit is very good and χ^2/ndf is equal to 896.51/821 which is bet-

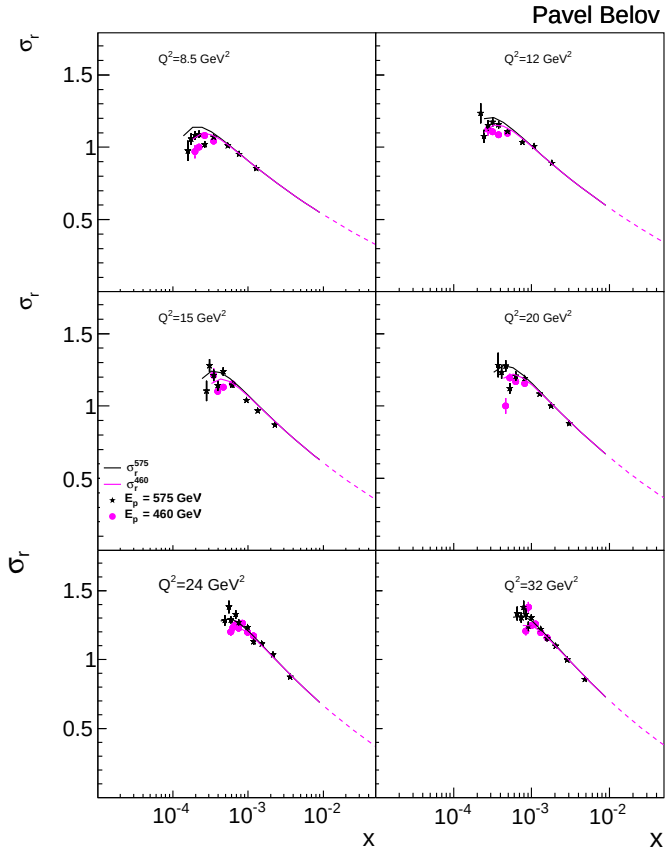

Figure 44: The continuation of Figure 43.

ter than in the previous analysis. The values of the partial χ^2/ndf are given in Table 16 for comparison. The table shows that the low Q^2 data is described by the DGLAP fit moderately.

Dataset	without E_p = 920 GeV	with E_p = 920 GeV
Combined E_p = 460, 575 GeV	247.8/187	246.3/187
HERA I	551.0/592	552.4/592
H1 CJC E_p = 920 GeV	—	13.9/29
H1 BST E_p = 920 GeV	—	22.5/23
Correlated χ^2	59.2	61.4

Table 16: The partial χ^2/ndf's of the DGLAP in the ACOT scheme fits to combined reduced proton beam energy data and combined HERA I data without and with H1 nominal proton beam energy data. The correlated χ^2 is also shown.

The central values obtained in the current analysis (Table 17) are very similar to the values from the previous analysis (Table 10). Therefore, the extracted PDFs are almost identical to the PDFs shown in Figure 36. The comparison of the PDFs obtained in current and previous

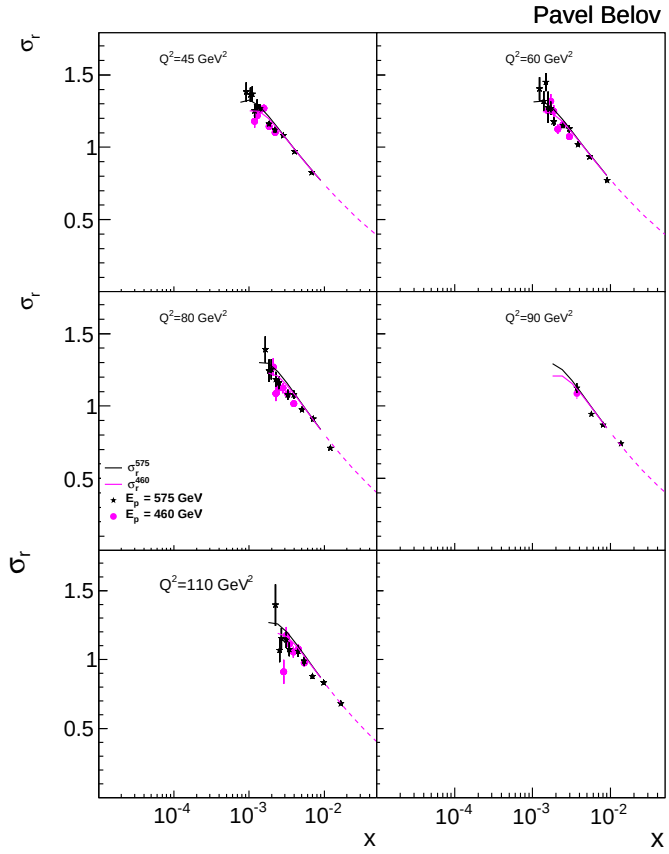

Figure 45: The continuation of Figure 43.

analyses is shown in Figure 51. It is clearly seen in the plots that there are no large differences of the PDFs obtained in these two analyses. As a result, it is possible to state that the addition of the H1 nominal proton beam energy data improves the fit quality but does not affect the extracted PDFs.

PDF	A	B	C	E
xg	7.73	0.236	9.11	
xu_v	4.15	0.691	5.02	10.88
xd_v	2.41	0.691	4.45	
$x\overline{U}$	0.099	-0.184	1.63	
$x\overline{D}$	0.143	-0.184	3.49	

Table 17: The fitted parameters of the HERAPDF1.0 parametrization obtained after a NLO QCD fit to the H1 nominal proton beam energy $E_p = 920$ GeV run data as well as the combined HERA I and combined $E_p = 460, 575$ GeV data.

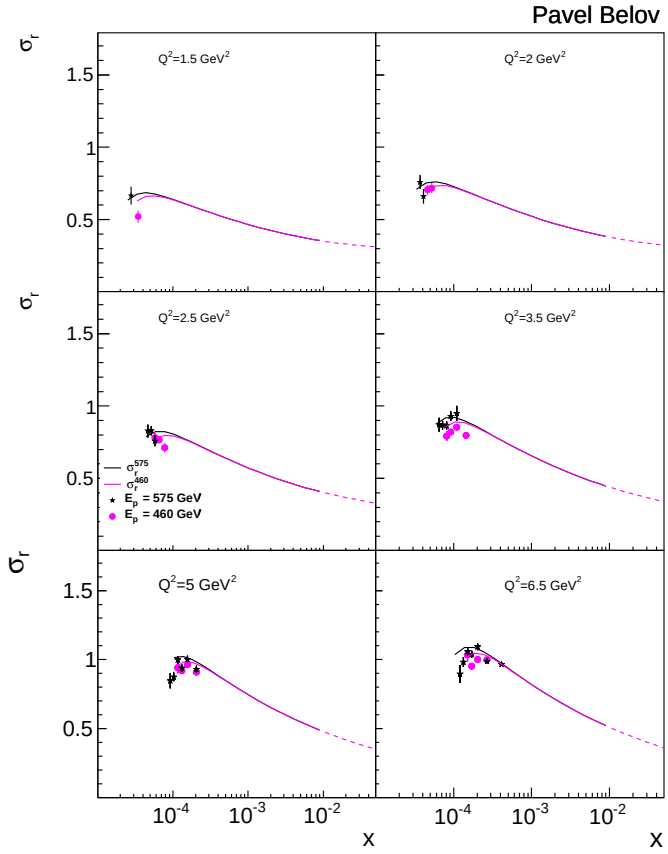

Figure 46: The reduced proton beam energy $E_p = 460, 575$ GeV cross section data as a function of x for different values of Q^2. The solid lines present the results of BGK dipole model central fit with DGLAP valence contribution to the combined reduced proton beam energy together with the HERA I NC data. The fit to data has been performed in the restricted $Q^2 > 3.5$ GeV^2 and $x < 0.01$ kinematic region. The extrapolation of fitted curves to the $x > 0.01$ kinematic region is shown by the dashed lines.

The dipole model fits have been also performed. The fit conditions are identical to the dipole model fits which are described above. The results of the dipole model fits as well as the dipole model fits with the constant valence contribution estimated by DGLAP together with the obtained values of the parameters are given in Tables 18-19. It is clearly seen from the obtained χ^2's that comparing with the previous dipole model fits the qualities of all fits have improved, while the central values of the model parameters remained similar. For the entire kinematic range over Q^2 better description of the data is achieved by IIM dipole model. For the restricted range $Q^2 > 3.5$ GeV^2 BGK dipole model shows the best description of the data with $\chi^2/ndf = 487.4/432$. The addition of the valence quark contribution estimated from DGLAP fit improves quality of the fit also only for the BGK dipole model. The χ^2/ndf becomes even

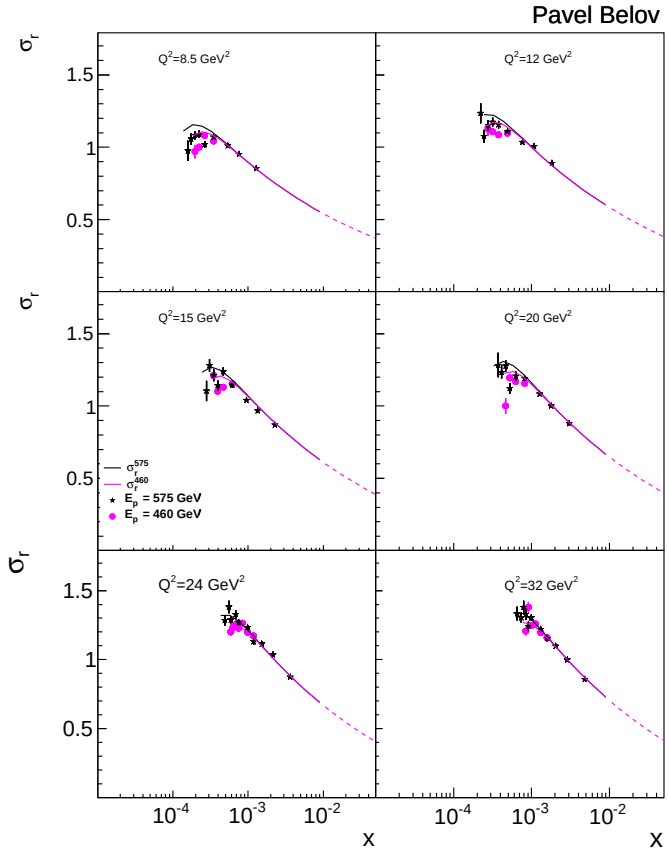

Figure 47: The continuation of Figure 46.

better and equals to 471.4/432.

The cross section data and curves obtained using the fitted parameters for the best fit, which is the BGK dipole model fit with the valence quark contribution estimated by DGLAP, are presented in Figures 52-54. The curves for proton beam energies $E_p = 460, 575$ GeV are similar to the curves shown in Figures 46-48. The Q^2 binning of the data with $E_p = 920$ GeV differ from the binning used in our analysis, therefore some plots do not contain the nominal proton beam energy datapoints.

In summary, the addition of the nominal proton beam energy data improves the fit results and does not significantly change the values of the PDF parameters and the dipole model parameters. IIM and BGK dipole models describe the data well and original GBW model still describes the data poorly.

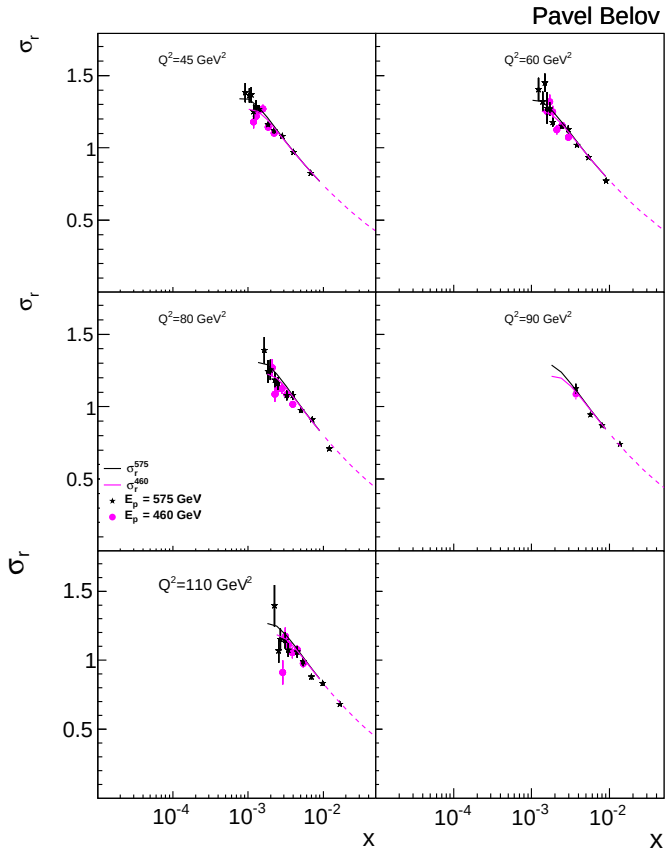

Figure 48: The continuation of Figure 46.

Model	Parameter	Value	
GBW	χ^2/ndf	1620.8/595	
	σ_0 (mb)	20.27	± 0.35
	λ	0.304	± 0.002
	x_0	$2.46 \cdot 10^{-4}$	$\pm 0.18 \cdot 10^{-4}$
IIM	χ^2/ndf	749.6/595	
	R_0 (fm)	0.603	± 0.021
	λ	0.264	± 0.002
	x_0	$0.514 \cdot 10^{-4}$	$\pm 0.012 \cdot 10^{-4}$

Table 18: Obtained fitted parameters, their total uncertainties and the qualities in terms of χ^2/ndf for the GBK and IIM dipole model central fits to the data including H1 nominal proton beam energy data. The fits are performed without applying any constrains to four-momentum squared Q^2.

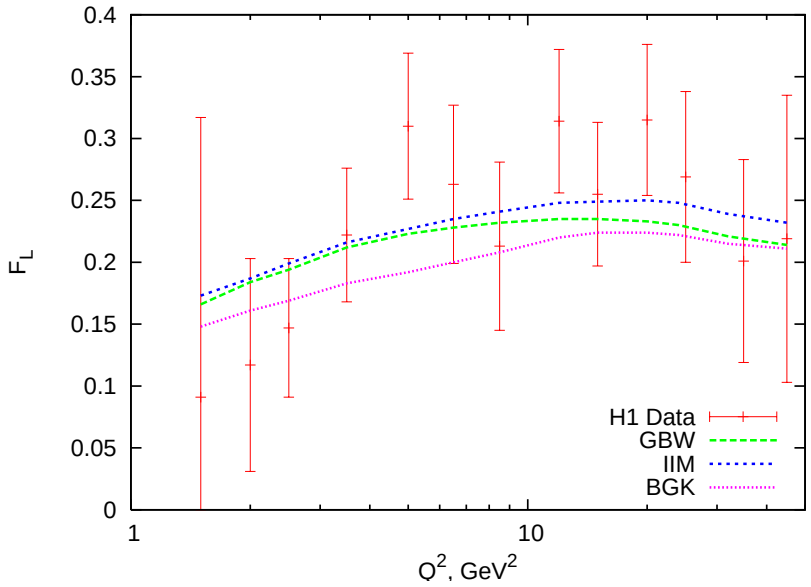

Figure 49: The proton structure function F_L as a function of Q^2. The data are given in [84]. The full error bars indicate the total uncertainty. The dashed lines show the predictions of F_L obtained from the different dipole model fits to data used in this analysis.

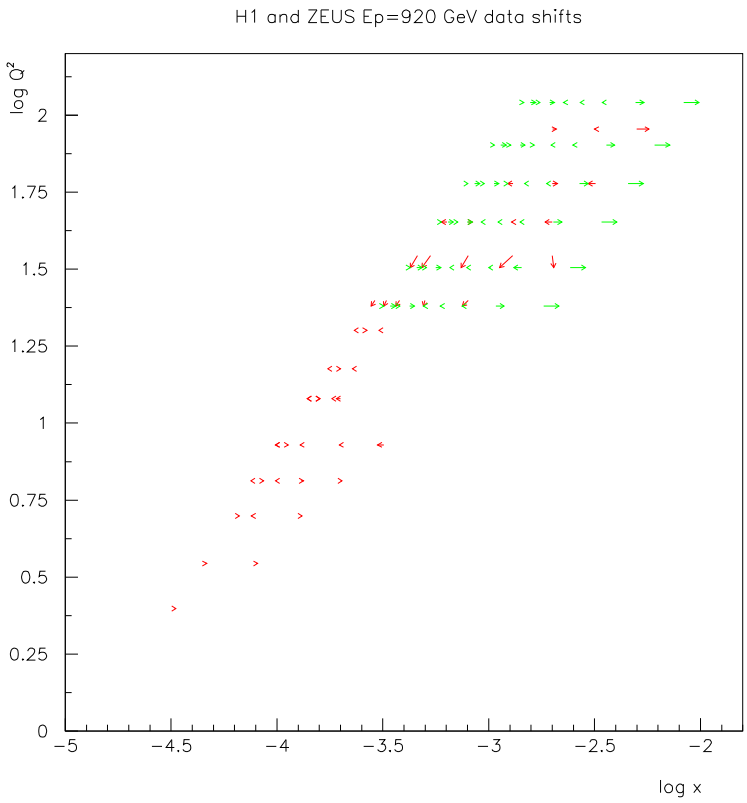

Figure 50: The H1 and ZEUS bin centers and their movements to the common grid bin centers. The H1 bin centers are shown by red color, the ZEUS bin centers are green.

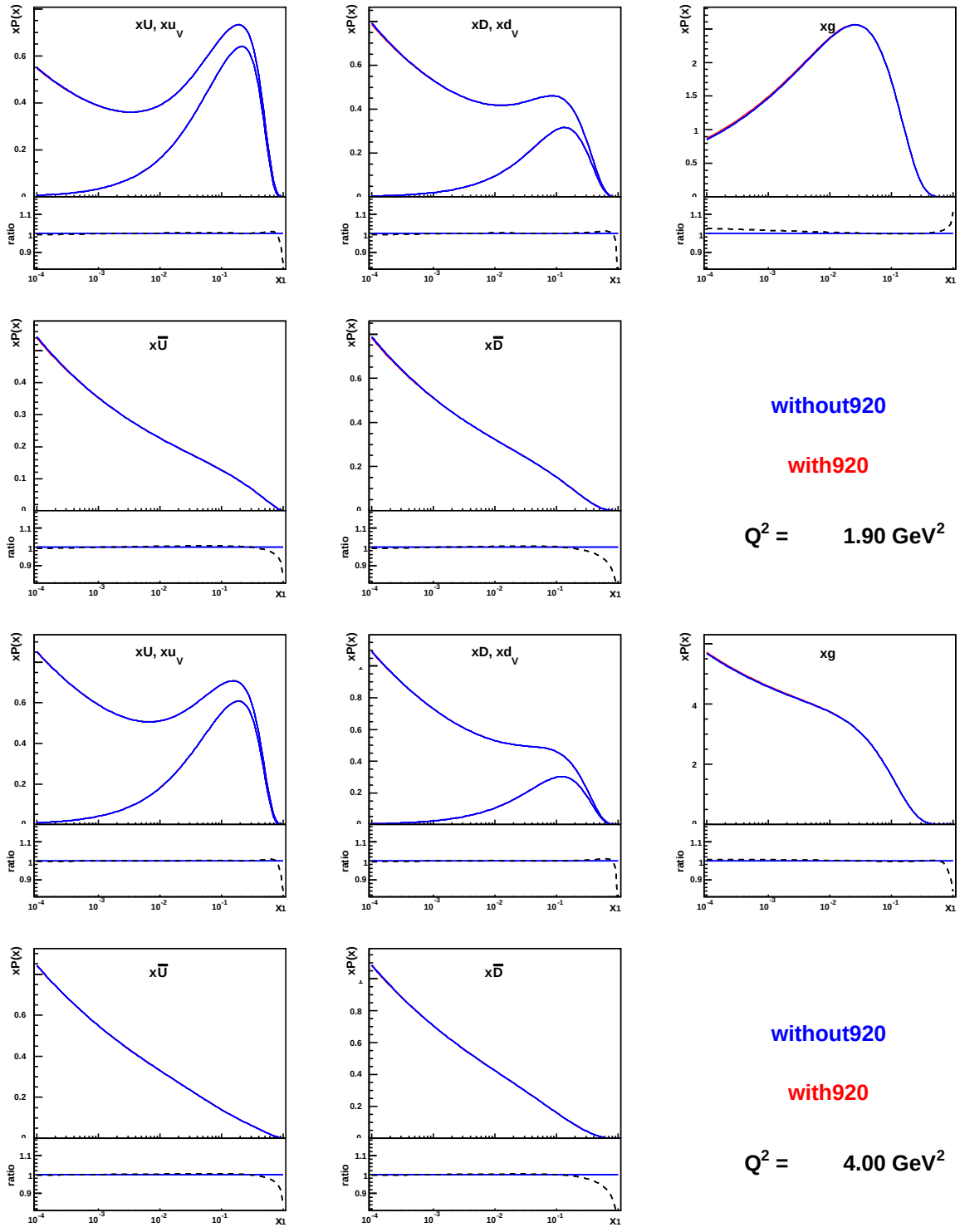

Figure 51: The comparison of the extracted PDFs for the $E_p = 920$ GeV data, HERA I data and combined reduced proton beam energy data at two different scales $Q^2 = 1.9, 4.0\,\mathrm{GeV}^2$. The bottom panel shows the ratio of these PDFs.

Model	Parameter	$\text{DGLAP}_{\text{valence}}$		$Q^2 \geq 3.5\ \text{GeV}^2$	
GBW	χ^2/ndf	1416.1/434		1312.1/434	
	σ_0 (mb)	17.45	± 0.56	19.33	± 0.57
	λ	0.360	± 0.003	0.310	± 0.002
	x_0	$3.61 \cdot 10^{-4}$	$\pm 0.42 \cdot 10^{-4}$	$2.97 \cdot 10^{-4}$	$\pm 0.38 \cdot 10^{-4}$
IIM	χ^2/ndf	548.5/434		525.5/434	
	R_0 (fm)	0.684	± 0.008	0.604	± 0.006
	λ	0.302	± 0.004	0.264	± 0.003
	x_0	$0.115 \cdot 10^{-4}$	$\pm 0.015 \cdot 10^{-4}$	$0.495 \cdot 10^{-4}$	$\pm 0.049 \cdot 10^{-4}$
BGK	χ^2/ndf	471.4/432		487.4/432	
	σ_0	75.3	± 3.5	115.5	± 6.1
	μ_0^2	6.66	± 1.06	1.64	± 0.14
	A_g	4.24	± 0.66	2.28	± 0.09
	B_g	0.012	± 0.003	0.095	± 0.011
	C_g	17.7	± 1.7	6.5	± 1.4

Table 19: Obtained fitted parameters, their total uncertainties and the qualities in terms of χ^2/ndf of the dipole model fits for restricted kinematic region without and with the constant valence contribution estimated from the DGLAP fit in the ACOT scheme. The fits of both types are performed with a constrain to four-momentum squared $Q^2 \geq 3.5\ \text{GeV}^2$. The input data include the H1 nominal proton beam energy data.

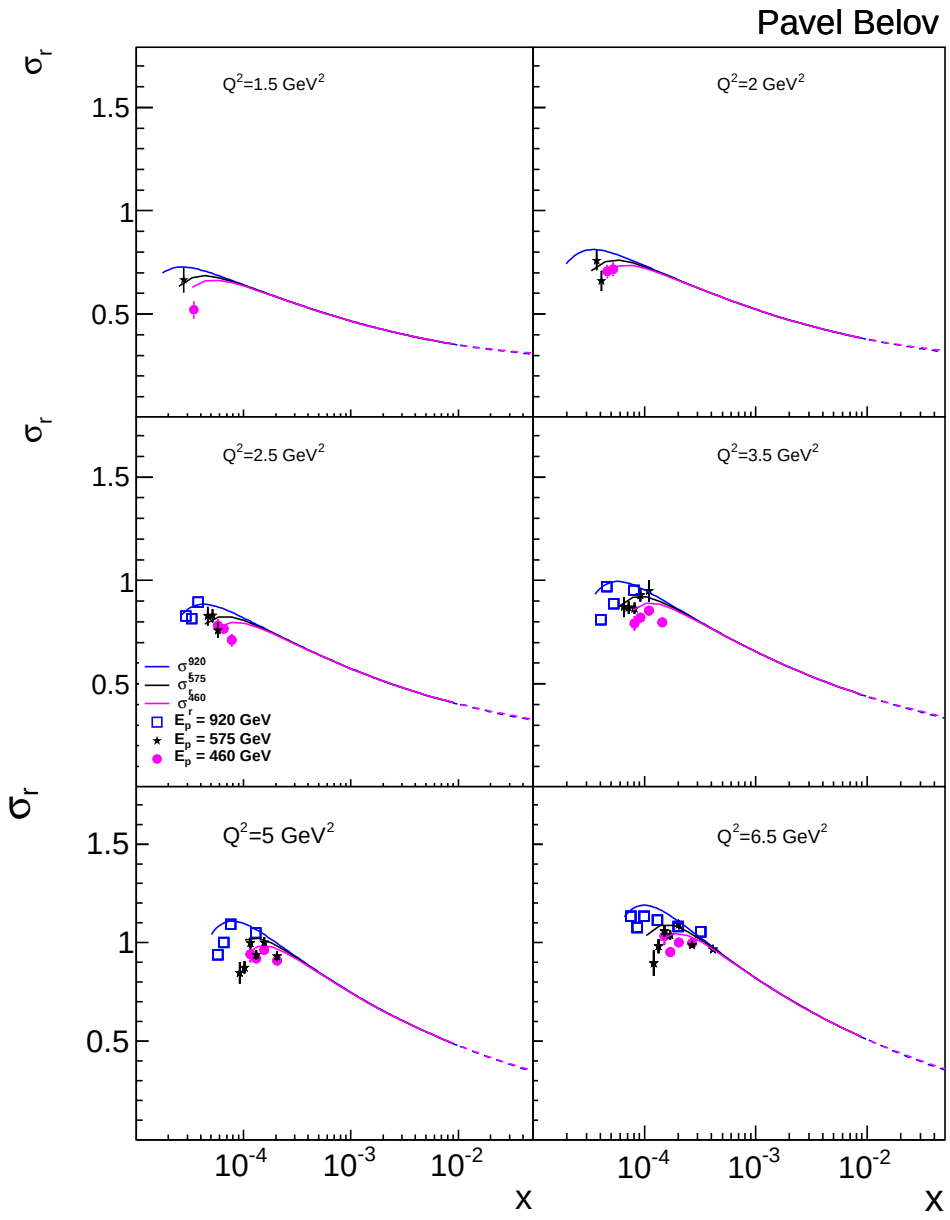

Figure 52: The reduced proton beam energy $E_p = 460, 575$ GeV and nominal proton beam energy cross section data as functions of x for different values of Q^2. The solid lines present the results of BGK dipole model central fit with DGLAP valence contribution. The fit to data has been performed in the restricted $Q^2 > 3.5\,\mathrm{GeV}^2$ and $x < 0.01$ kinematic region. The extrapolation of fitted curves to the $x > 0.01$ kinematic region is shown by the dashed lines.

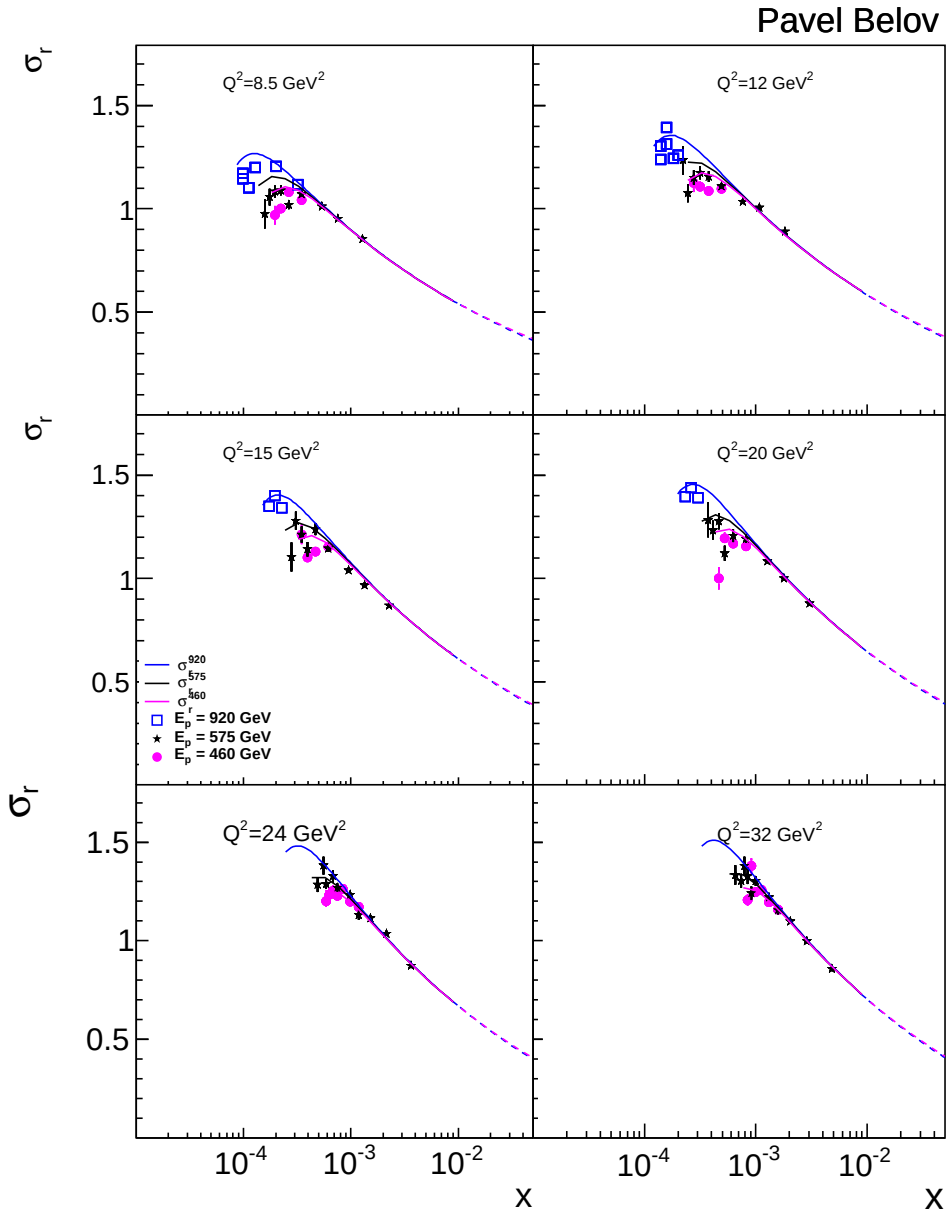

Figure 53: The continuation of Figure 52.

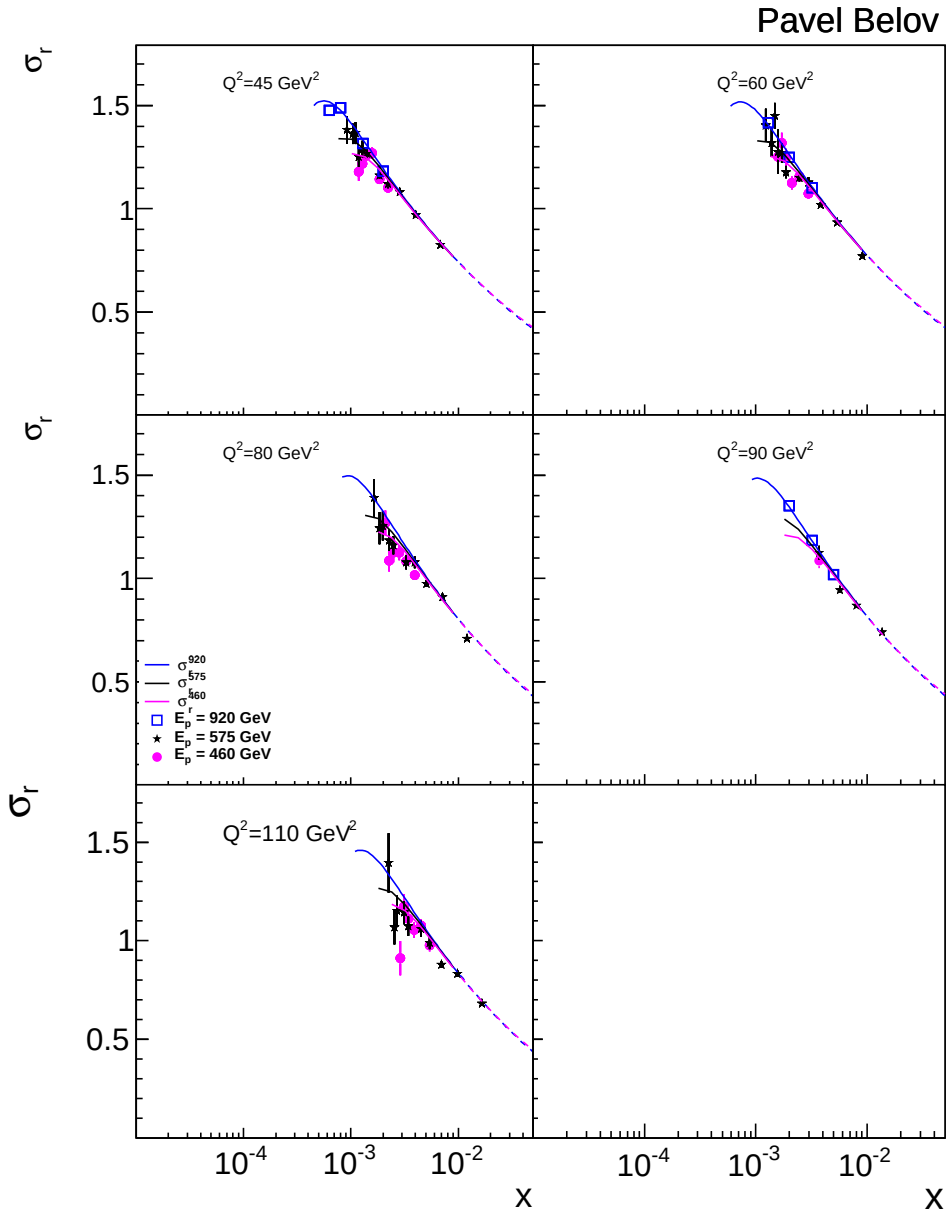

Figure 54: The continuation of Figure 52.

6.6 Extraction of the structure function F_L

6.6.1 Modification of the combination procedure

The determination of the structure function F_L is based on the combination procedure presented in Chapter 5. For extraction, the described combination procedure is modified by introducing in the χ^2-function the two vectors corresponding to the structure functions F_2 and F_L. With these modifications, the χ^2 function becomes:

$$\chi^2_{exp}(\vec{F_2}, \vec{F_L}, \vec{b}) = \sum_i \frac{\left((F_2^i - ((y^i)^2/Y)F_L^i) - \sum_j \Gamma_j^i b_j - \mu^i\right)^2}{\Delta_i^2} + \sum_j b_j^2, \tag{130}$$

where the formula (15) has been explicitly used. The measured values of the reduced cross sections for different (x, Q^2) bins and different CMEs are denoted by μ^i. The statistical and uncorrelated systematic uncertainties are added in the demonimator in quadrature $\Delta_i^2 = \Delta_{i,stat}^2 + \Delta_{uncor}^2$.

The χ^2-function depends on the structure function values F_2^i, F_L^i and systematic shifts b_j. For small $y < 0.35$, the coefficient y^2/Y becomes less than 0.086 and thus the structure function F_L can not be accurately measured. For the studied kinematic range, an additional term has been added to the χ^2 function (130). This additional term is given by the formula

$$\chi^2_{add}(\vec{F_2}, \vec{F_L}) = \sum_i \frac{\left(F_L^i - \frac{R}{R+1}F_2^i\right)^2}{\Delta_{F_L}^2}. \tag{131}$$

Here R is the ratio (22) which does not strongly vary as a function of x in the given kinematic region. The measurements show [84] that $R \sim 0.25$, and therefore it was chosen equal to 0.25. The width $\Delta_{F_L} = 3$ is taken in a such way that the extra penalty term (131) gives a negligible influence for $y > 0.35$. The term has a significant contribution at low y only and affects the points with large uncertainties on F_L. This term provides a constraint for cross normalisation of the cross-section data at low y and thus reduces uncertainties due to the relative normalisation of the data at different CMEs.

6.6.2 Results and comparisons

For determination of the longitudinal structure function, the H1 and ZEUS separate reduced proton beam energy $E_p = 460, 575$ GeV datasets together with the combined sample of the published H1 $E_p = 920$ GeV data from [69,70] have been used. Taking into account the published H1 HERA I data instead of new HERA II data is motivated by a wider Q^2 acceptance at low y, extending to $Q^2 = 1.5\,\mathrm{GeV}^2$, and better accuracy of the HERA I measurements. The extraction of the longitudinal structure function F_L from cross section measurements has

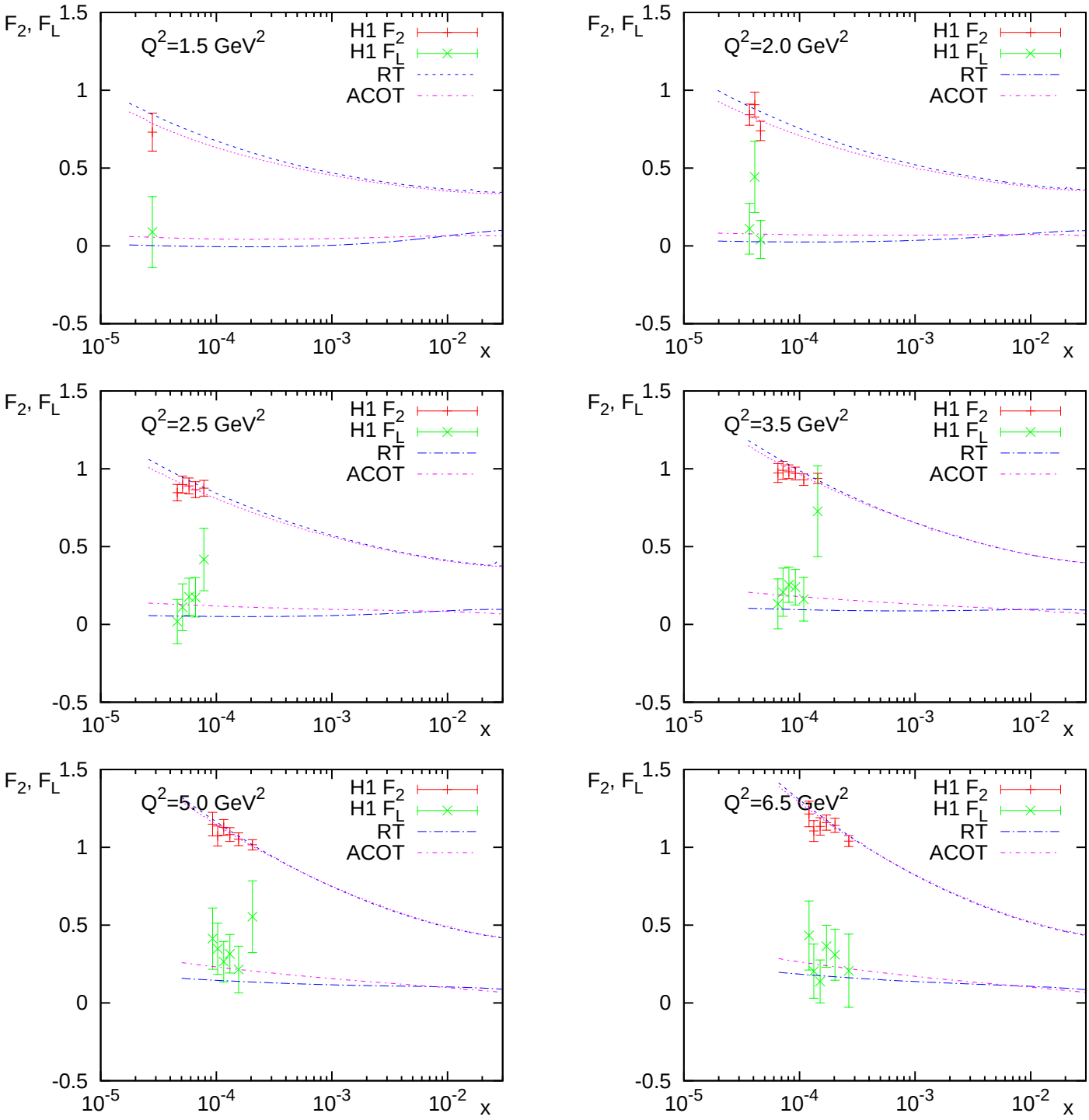

Figure 55: The extracted values of proton structure functions $F_2(x, Q^2)$ and $F_L(x, Q^2)$ as well as predictions of the DGLAP fit in the RT and ACOT schemes are shown. The total uncertainties of the data are indicated. Some uncertainties are large and spread beyond the plot.

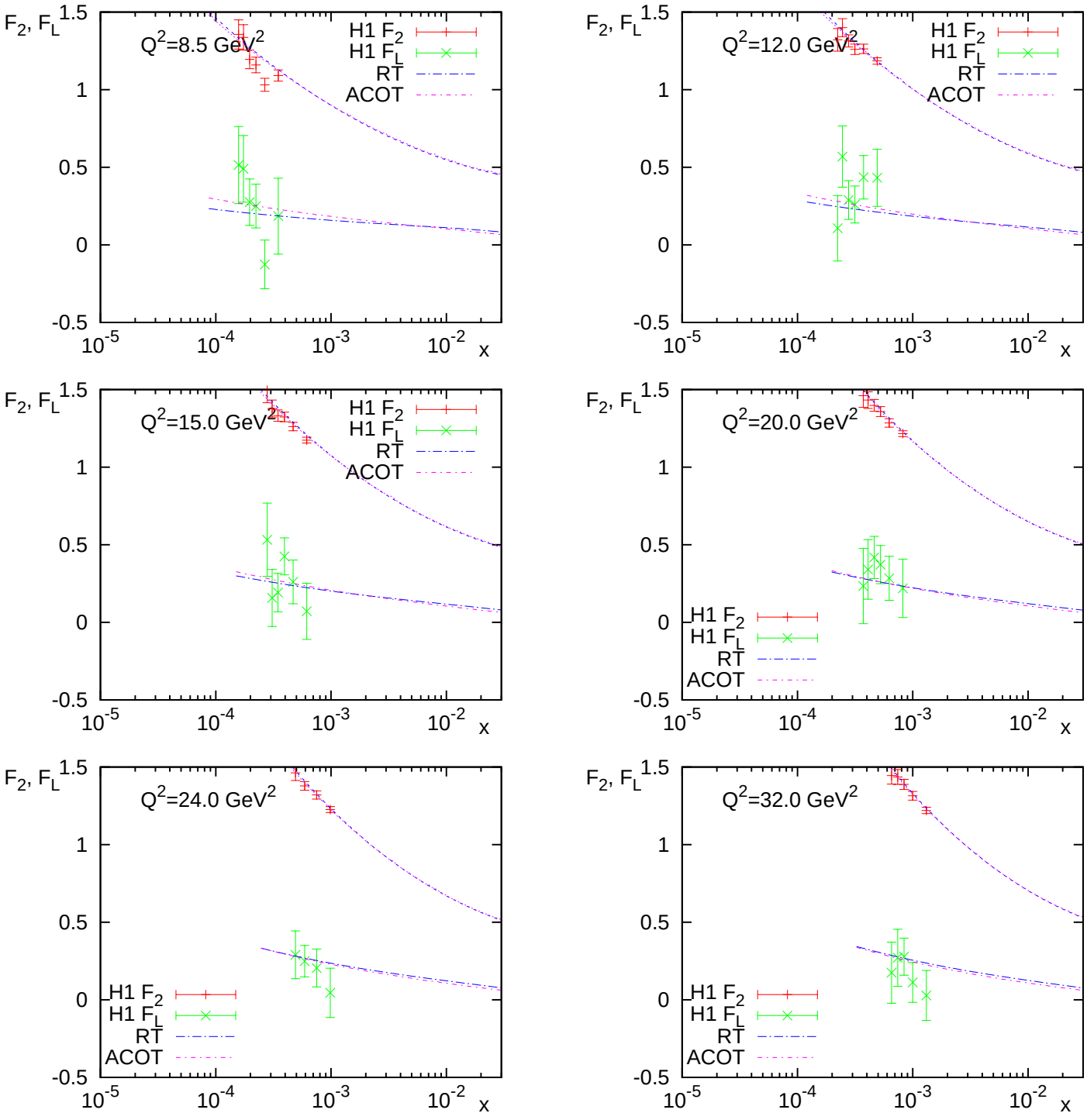

Figure 56: The continuation of Figure 55.

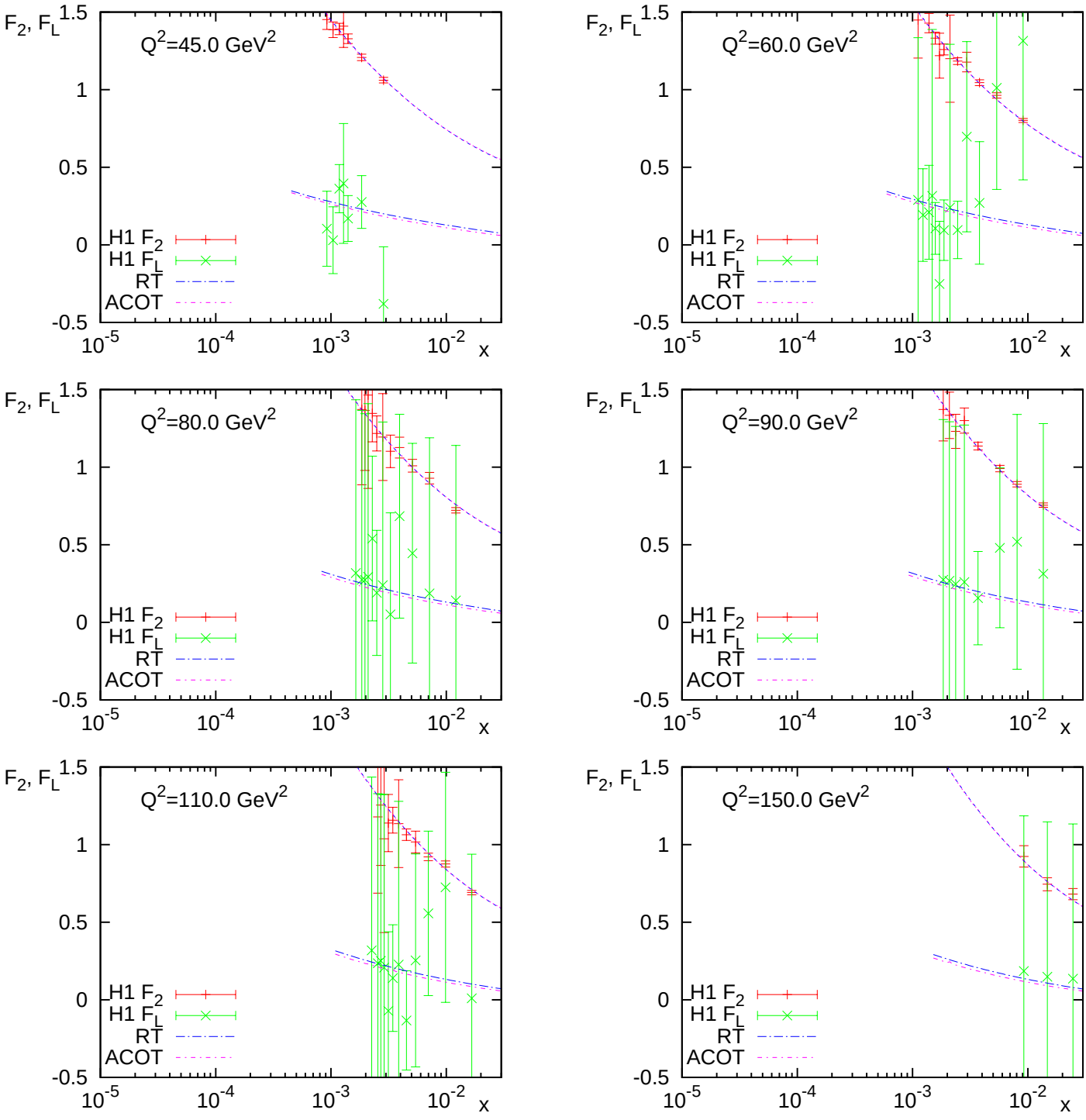

Figure 57: The continuation of Figure 55.

been carried out by the modified combination procedure described above. The common grid presented in this chapter has been used in the combination procedure for F_2 and F_L extraction.

The obtained values of the longitudinal structure function F_L together with the uncorrelated and correlated systematic, statistical and total uncertainties are given in Table 29. The structure function values are given for $1.5 \leq Q^2 \leq 150$ GeV^2. The data are shown only with the total uncertainties below 0.3 for $Q^2 < 40$ GeV^2 and below 0.4 for $Q^2 = 45$ GeV^2. The presented values complement the previously published values of F_L by the H1 and ZEUS collaborations [84,87]. The total uncertainties for some values of F_L are sufficiently large and do not allow us to make a strong conclusion about the behavior of the longitudinal structure function in correspondent kinematic domains. Nevertheless, the extracted F_L values with relatively small uncertainties are similar to the previously published values of F_L.

Figures 55-57 show the obtained values of the structure functions F_2 and F_L compared to predictions of the NLO DGLAP fit in the ACOT and RT schemes. The data are shown for all Q^2 bins after the cuts on the total uncertainty described above. The structure function F_2 is determined much more precisely than F_L. The measurements show the nonzero longitudinal structure function at medium Q^2. As predicted by perturbative QCD, F_L is significantly smaller than F_2 but aquires non-zero value due to higher order effects. The structure function F_L is in particular sensitive to the gluon density which can be constrained by the F_L data. The predicted values of F_L have been obtained from DGLAP fits to the separate reduced proton beam energy and combined HERA I data. In spite of large uncertainties of the data with $Q^2 > 45$ GeV^2, it is seen that the predictions agree with the data. It is also seen that there is a significant difference between the predictions at low Q^2 and small x. The DGLAP fit in the ACOT scheme shows better description of the data predicting larger values of F_L at low Q^2. With the increase of Q^2 the ACOT and RT based predictions become almost the same.

The values of F_L averaged over x for fixed Q^2 are presented in Table 20. The averaging has been performed and the uncertainties have been calculated taking into account only statistical and uncorrelated uncertainties according to formula (105). The total uncertainty squared is a sum of the statistical and uncorrelated systematic uncertainties together with the systematic correlated uncertainties of the averaged measurements added in quadrature. The cuts on the total uncertainty mentioned above are applied before averaging. Different cuts on total uncertainties have been tried. The cuts suppressing F_L with large uncertainties at high Q^2 lead to floating of F_L at such values of four-momentum transfers squared and even make it negative at some Q^2 bins, whereas the results at low Q^2 do not significantly change. This takes place due to data with relatively small uncertainties at low Q^2. Otherwise, the absence of cuts leads to negative F_L at low Q^2. As a result, the already mentioned cuts to the data as in [84] have been chosen due to its reliability.

The obtained values of F_L together with the statistical and total uncertainties are also shown in Figure 58. The statistical uncertainty of the $F_L(x, 150)$ is beyond the limits of the figure.

Q^2 GeV^2	x	F_L	Δ_{stat}	Δ_{unc}	Δ_{cor}	Δ_{tot}
1.5	0.279×10^{-4}	0.089	0.114	0.190	0.061	0.229
2.	0.426×10^{-4}	0.125	0.039	0.075	0.018	0.086
2.5	0.589×10^{-4}	0.161	0.025	0.051	0.008	0.057
3.5	0.881×10^{-4}	0.235	0.021	0.049	0.007	0.054
5.	0.129×10^{-3}	0.318	0.022	0.055	0.007	0.059
6.5	0.170×10^{-3}	0.267	0.023	0.059	0.009	0.064
8.5	0.226×10^{-3}	0.220	0.025	0.063	0.009	0.068
12.	0.322×10^{-3}	0.335	0.027	0.051	0.008	0.058
15.	0.406×10^{-3}	0.272	0.027	0.051	0.009	0.059
20.	0.545×10^{-3}	0.333	0.029	0.054	0.009	0.062
24.	0.687×10^{-3}	0.208	0.026	0.052	0.013	0.059
32.	0.935×10^{-3}	0.177	0.032	0.052	0.013	0.063
45.	0.141×10^{-2}	0.202	0.038	0.059	0.005	0.070
60.	0.205×10^{-2}	0.148	0.047	0.065	0.001	0.081
80.	0.345×10^{-2}	0.322	0.091	0.185	0.000	0.206
90.	0.460×10^{-2}	0.266	0.122	0.175	0.003	0.213
110.	0.489×10^{-2}	0.127	0.098	0.132	0.004	0.164
150.	0.162×10^{-1}	0.157	0.573	0.060	0.001	0.576

Table 20: The longitudinal proton structure function $F_L(x, Q^2)$ obtained by averaging the data from Table 29.

Comparison of the obtained values with the F_L data from the publication [84] shows that the addition of the ZEUS data makes it possible to significantly reduce the uncertainties for $24 \leq Q^2 \leq 45$ GeV^2. The measurements of F_L and the ratio of values obtained in the current analysis to the published H1 F_L data are given in Figure 59. The extracted central values are in good agreement with the results obtained by the H1 and ZEUS collaborations [84,87]. Smaller uncertainties of F_L data from ZEUS may be caused by the ZEUS nominal proton beam energy $E_p = 920$ GeV data which were excluded from the current analysis (see section 6.4).

The obtained data have been confronted to the theoretical predictions calculated using the PDFs from MSTW and HERAPDF sets [34,48]. Depending on the certain PDF set, the calculations have been performed at NLO or NNLO in perturbative QCD. These plots are shown in Figures 60-61. The predictions based on MSTW08 PDF set describe the data reasonably well. A good description is achieved at medium and high Q^2, where the predicted F_L has also small total uncertainties. At low Q^2, the uncertainties of the predicted F_L become larger. Nevertheless, the predictions calculated at NLO and NNLO agree with the measurements. In the case of HERAPDF sets, the predictions strongly depend on the orders of perturbation theory. The HERAPDF1.0 and HERAPDF1.5 sets give similar predictions at NLO. They describe the data well at medium and high Q^2, whereas at $Q^2 < 10$ GeV^2 the predictions are lower than the data. At NNLO, the HERAPDF1.5 set shows good description of data for all range of Q^2. The uncertainties of the predicted values at NNLO are much larger than at NLO and comparable

with the uncertainties of MSTW predictions. Large uncertainties of the longitudinal structure function originate from large uncertainties of the gluon distribution at low x [48]. F_L (56) is a direct function of the gluon distribution and thus inherits all its properties. The more flexible gluon parametrization (72) used at NNLO and higher sensitivity to minimum-Q^2 cut are the main error sources. The latter clearly suggests that NNLO fits are more sensitive to low Q^2 data. Such uncertainties and sensitivity may indicate that the low Q^2 and low x data contain contributions beyond the standard perturbation expansion and therefore need to be considered in more detail in future.

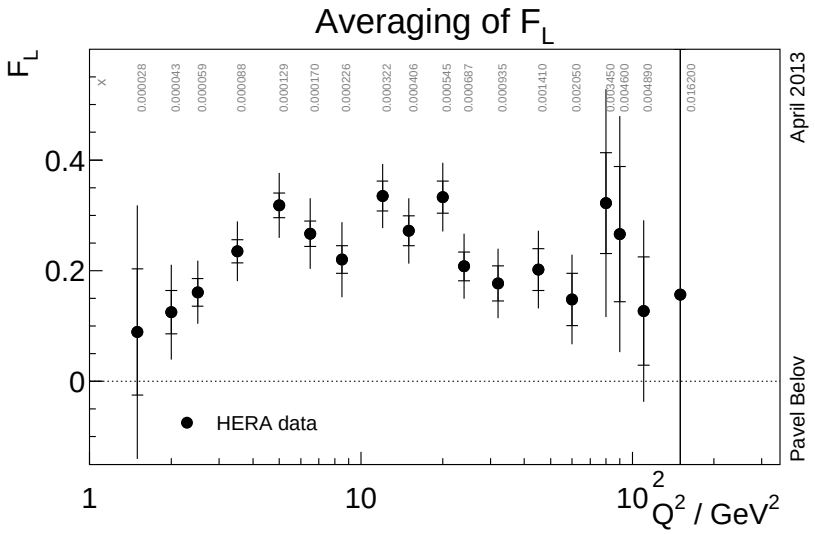

Figure 58: The longitudinal proton structure function F_L averaged over x shown as a function of Q^2. The average x values for each Q^2 are also shown. The inner error bars represent statistical uncertainties, whereas total error bars show total uncertainties.

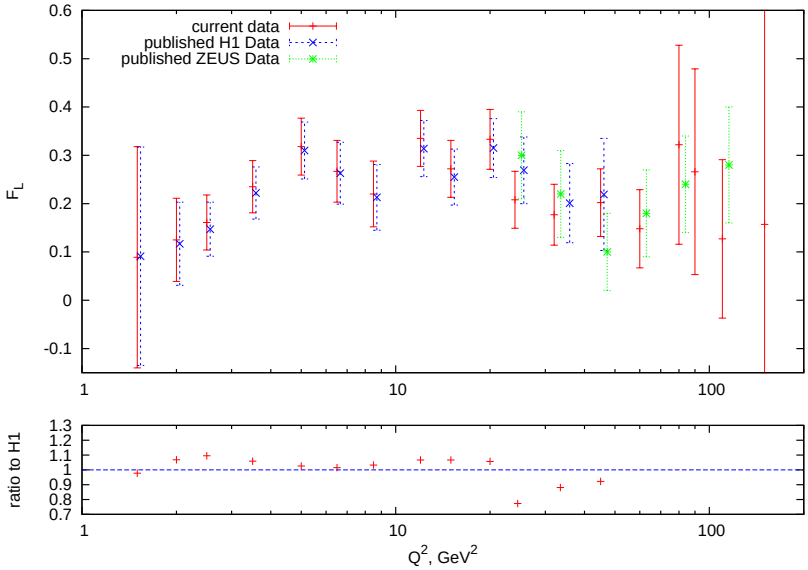

Figure 59: The values of F_L obtained in the current analysis as well as published H1 and ZEUS F_L values as functions of Q^2. The ratio to the H1 results are also shown. The error bars represent total uncertainties.

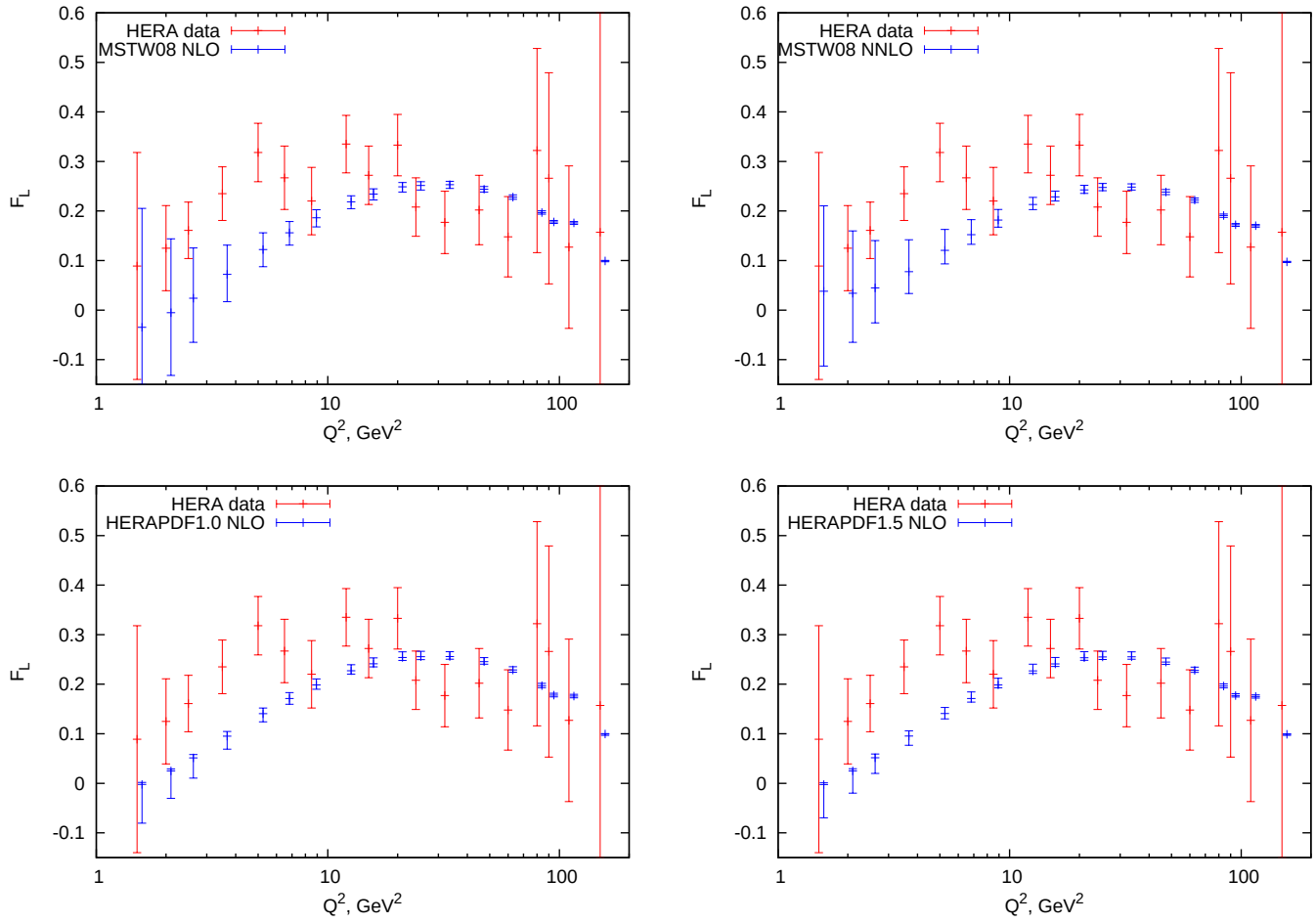

Figure 60: The obtained averaged values of the structure function F_L together with the different predictions calculated using the PDFs from MSTW and HERAPDF sets [34,48]. The error bars represent total uncertainties.

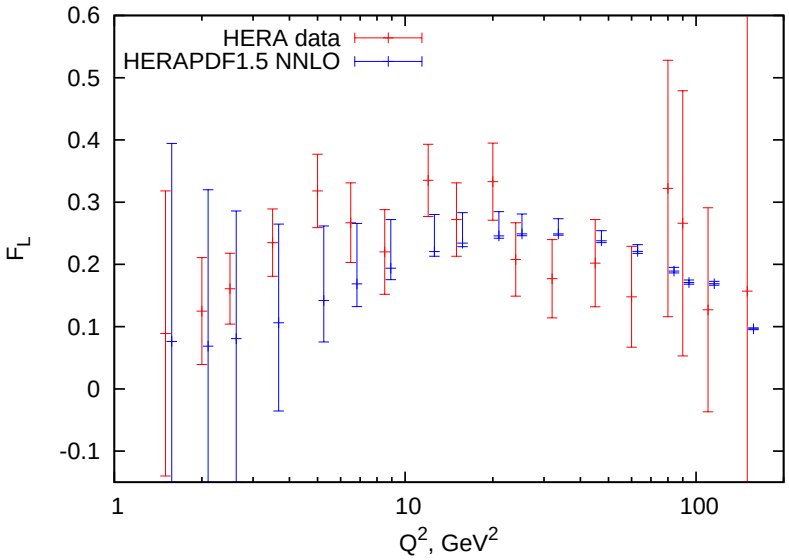

Figure 61: The obtained averaged values of the longitudinal structure function F_L together with the prediction from NNLO HERAPDF1.5 [48]. The error bars represent total uncertainties.

7 Conclusions

This thesis describes a combination of the H1 and ZEUS inclusive cross section measurements at proton beam energies of $E_p = 460$ GeV and $E_p = 575$ GeV and following QCD fits to the combined data. The combination has been performed using a dedicated combination procedure implemented as an independent averaging package and a common bin grid. The HERA II reduced proton beam energy $E_p = 460, 575$ GeV data from two experiments show a good compatibility and therefore these data have been combined. The cross section central values have been averaged and uncertainties of obtained data points have decreased in the overlapping phase-space.

The QCD fits to data have been carried out. The NLO DGLAP fits to the published HERA I and combined reduced proton beam energy data made it possible to accurately determine PDFs. The comparison of PDFs obtained in the current work with PDFs obtained solely from HERA I data showed small changes of the densities. The main difference is in the gluon distribution which became larger for $x < 0.01$ with addition of the combined data. Other distributions demonstrate almost no variations for $0 < x < 1$. The uncertainties of PDFs have reduced slightly and the main improvement in precision is observed for the gluon distribution. A fit which includes additional H1 cross section data taken at $E_p = 920$ GeV in high y region during the HERA II operation period showed improved quality, however PDFs did not change significantly.

The low-x dipole models have been tested using the combined data and the parameters of the models have been determined. Three models have been under investigation. They are the original GBW model, the IIM dipole model which is based on the colour glass condensate approach to the high parton density regime and the BGK dipole model taking into account the DGLAP evolution of the gluon distribution. The fits to the neutral current data have been done in the kinematic region $x < 0.01$ and for the BGK dipole model additionally $Q^2 > 3.5\,\mathrm{GeV}^2$. The GBW dipole model failed to describe the data. The IIM dipole model described the data well, whereas the BGK dipole model showed the best description of data with the χ^2/ndf approaching unity.

The original dipole models ignore contributions of the valence quarks. To study the impact of the valence densities, they have been estimated using DGLAP fits and added to the dipole models. The addition of the valence contribution degraded the quality of GBW and IIM fits, but remarkably improved the quality of BGK fit. The fitted parameters of the models are similar to the parameters obtained before. Similar to DGLAP fits, taking into account the H1 nominal proton beam energy data improved the quality of fits and parameters changed slightly.

The longitudinal structure function F_L has been obtained using a modified combination procedure. The H1 and ZEUS reduced proton beam energy data together with the published H1 $E_p = 920$ GeV data have been used for F_L extraction. The extracted values of F_L are similar to data obtained in previous analyses. The lack of low Q^2 ZEUS data and large experimental

uncertainties of available H1 data prevent any strong conclusion about the behavior of F_L at $Q^2 < 10\,\mathrm{GeV}^2$. Nevertheless, the accuracy of F_L values have been sufficiently improved at medium Q^2 where measurements of both experiments are present. The measured structure function F_L is described by the theoretical predictions based on the MSTW and HERAPDF sets.

8 Acknowledgments

This chapter is totally devoted to the gratitude which I would like to express to all people who helped me by the advices and questions and also paid attention to my work. Without you this work could not be done and it is pleasure to me to say thank you!

The given work contains the ideas and results of many individuals. Most of their names are listed in the bibliography and especially in the correspondent H1 and ZEUS papers. I highly appreciate their important contributions to the subject. Moreover, I wish to extend my deep gratitude to the following physicists who have given me invaluable assistance with many parts of my studies.

First of all, I would like to thank my supervisor Dr. Alexandre Glazov, who provided me a possibility to work in the H1 collaboration in DESY. His constant attention to my work was extremely helpful and without it I most likely did not managed to succeed with my studies. His impact to my work can hardly be overestimated and the influence was so high that I sometimes thought that he follows to me. Nevertheless, it is great that it was so and my studies were successful because of it. Moreover, I am thankful to him for the willing to be a referee of my Dissertation and Disputation.

Secondly, I would like to say thanks here to all authors of the H1 and ZEUS collaborations. About half of them I have never seen, but without their work and work of many others who are beyond the lists of the H1 and ZEUS authors but contributed a lot to the HERA experiments the present thesis could not appear. I am grateful to all these people. You and your work have left the prominent mark in the contemporary particle physics.

Especially, I would like to note my close colleagues: Voica Radescu who was helping and checking my contributions to the HERAFitter, Ringaile Plačakyte who was helping to solve various problems arising during the HERAFitter development, Katerina Lipka who was the main user of the HERAverager and helping to make it better, Katarzyna Wichmann who was performing test of the data combination, Dieter Haidt who paid an attention to a part of my work and gave valuable advices, Henri Kowalski who is the expert in the dipole models and an active user of the dipole part of the HERAFitter. Agnieszka Luszczak who is also the advanced user of the HERAFitter and was helping me with implementation and checking of the BGK dipole model, Alexey Petrukhin who was teaching me who to do the analysis and to use the dedicated machinery, Alexander Bylinkin who was helping with some plotting tools and supporting me during the weekends.

I also very thankful to Anastasia Grabenyuk, Julia Grebenyuk, James Dassoulas, Mikhail Karnevskiy for reading and making valuable comments on the manuscript. Misha and Nastja, with your recommendations and corrections the thesis became much better! I am also very proud that James was of so high opinion of my English.

Thirdly, I am very glad to say thanks to my office-mates (in chronological order): Mira

Krämer, Zlatka Staykova, Pedro Cipriano, Jörg Behr, Martin von den Driesch, Martin Brinkmann. It was nice to share the offices with you and to feel that I am not alone there. I would like to express special thank to Martin Brinkmann and Daniel Britzger who kindly translated the abstract of my thesis to German and were also helping me a lot to communicate with secretaries from the university. I wish you all the best in his future live and a big success in science.

Fourthly, I wish to express my gratitude to my kantinemates: Hannes Jung, Albert, Nastja, Panos, Paolo, Samanta, Pedro and many others who joined us during the lunches. You were extremely helping me to feel the dishes much more taste!

Fifthly, I am grateful to Carsten Niebuhr (on behalf of DESY) for the financial support of my studies and Alla Grabowsky for a lot of help with the bureaucratic matters which I had some time.

After all, I am very grateful to my parents: Alexey Belov and Tatiana Belova and also to my sister Olya who was supporting and inspiring me all my life and especially via Skype these three years.

In conclusion, I would like to express my gratitude to

- The referee of my Dissertation: PD Dr. Thomas Schörner-Sadenius,
- The referee of my Disputation: Prof. Dr. Peter Schleper,
- The chairman of my Disputation: Prof. Dr. Dieter Horns.

Thank you very much!

9 Appendix

9.1 HERAverager documentation

9.1.1 Introduction

The present manual provides a brief practical description of the HERAverager program which makes it possible to perform averaging of data from different experiments. Although the averaging procedure is independent of the type of data, for the deep inelastic scattering (DIS) data the specific options for averaging are designed.

9.1.2 Installation

The package is available on the cite

https://wiki-zeuthen.desy.de/HERAverager

The packed tarball can be downloaded and unpacked into any directory in a local machine. The installation assumes following prerequisites:

- Unix/Linux operation system with 2MB free disk space
- standard gfortran compiler version 4.1 and higher
- libraries CERNLibs with the environment variable CERN_ROOT,
  which can be defined by the command
  `export CERN_ROOT=/afs/cern.ch/sw/lcg/external/cernlib/2006a`
- (optionally) the HERAFitter package with the environment variable HERAFITTER,
  which points out to the main directory of the package

To install HERAverager please execute the following commands in a directory with the tarball:

```
>tar -xzf heraverager-XYZ.tar.gz
>cd heraverager
>./configure
>make install
```

In case of success the executable file HERAverager of the program will be placed in directory ./bin In case of any fail of the commands above please do not hesitate to contact the developers by email

heraverager-help@desy.de

Please, do not forget to indicate the configuration of your computer system and the type of error.

9.1.3 Files

After successful installation the main directory of the `HERAverager` package will consist of installation files, `README` file and following subdirectories with files:

`./bin`

- `HERAverager` — the executable file

`./include`

- `common.inc` — the file with common variables

`./output` — the directory for the results of averaging

`./script`

- `DoSwimming.cmd` — the script for calling the `HERAFitter`

`./source` — the source codes

- `averaging.f` — perform the iteration procedure if needed
- `fillarrays.f` — prepare the system of equations
- `getcovar.f` — calculate variance and covariance matrices
- `heraverager.f` — the main source file
- `initave.f` — initialization of the parameters and performing the averaging
- `output.f` — print out the averaged cross sections into the data files
- `readdata.f` — read datasets and fill in the arrays of data and uncertainties
- `statrecalc.f` — perform a rescale of the uncertainties between iterations
- `swimming.f` — calculate the swimming corrections
- `toblockdiag.f` — solve the obtained system of linear equations

`./test` — examples and published data for testing purposes

- `steering` — test steering file
- `grid.dat` — test common grid file
- `h1460new.public.dat` — H1 inclusive NC E_p = 460 GeV dataset for testing
- `zeus460new.public.dat` — ZEUS inclusive NC E_p = 460 GeV dataset for testing
- `h1575new.public.dat` — H1 inclusive NC E_p = 575 GeV dataset for testing

- `zeus575new.public.dat` — ZEUS inclusive NC E_p = 575 GeV dataset for testing

The description of the averaging procedure which is implemented in the source files can be found in the correspondent chapter. Here we pay attention only to the practical usage of the averager.

9.1.4 Steering file

The launch of the test averaging inside the directory `./bin` is performed by the command:

```
>./HERAverager ../test/steering
```

The steering is a plain text file which consists of the following namelists:

`InFiles` defines the datasets to be averaged

`CommonGrid` defines the common bin grid

`HERAverager` defines the type for averaging of bins from one experiment

`BiasCorrection` contains options for type of the bias correction

`Swimming` defines the type for searching the common bins

`DIS` contains options applicable for DIS datasets

All options and possible values of them are listed in Table 21.

9.1.5 Datasets

The format of datasets for the `HERAverager` is the standard format which is used for `HERAFitter` datasets. The complete description of the format can be found in [LINK]. Below the simplest dataset for performing averaging is shown.

```
 &Data
   Name = 'ZBOSON'
   NData =           4
   NColumn =         6
   ColumnType = 2*'Bin','Sigma', 3*'Error'
   ColumnName = 'M1', 'M2', 'data', 'stat', 'uncor','sys5'

   IndexDataset = 1
   Reaction = 'Z'
```

InFiles	
`NInputFiles`	*integer* Number of averaged datasets
`InputFileNames(i)`	*string* Location of the i-th dataset
CommonGrid	
`GridType`	*string* Type of the common grid: • `External` - common grid is taken from an external file • `Auto` - the grid is taken immediately from the dataset grid points
`GridFiles`	*string* Locations of the external files with common grid
HERAverager	
`AveSameExp`	*logical* `.true., .false.` Whether to calculate a weighted average from two measurements of the same experiment hitted into the same bin
BiasCorrection	
`AverageType`	*string* Type of uncertainty treatment: • `'ADD'` - additive - no bias correction • `'MULT'` - multiplicative - all uncertainties are multiplicative • `'MIXED'` - mixed - according to the prescription in the dataset: 'sys1:A' - additive, 'sys1:M' - multiplicative
`Iteration`	*integer* Number of iterations in case of multiplicative or mixed treatment of the uncertainties
`RescaleStatSep`	*logical* `.true., .false.` Whether to rescale the stat and uncorr uncertainties separately
`CorrectStatBias`	*logical* `.true., .false.` Whether to correct the syst bias for stat errors
`FixStat`	*logical* `.true., .false.` Whether to keep the stat uncertainties fixed

Table 21: The options and possible values for these options in the steering file.

Swimming	
NearestType	*string* Type of uncertainty treatment: • 'Linear' - linear nearest bin by the order as they placed in the datafile (all processes) • 'DIS:ModuleXQ2' - minimum module of X and Q2 (only for DIS processes) • 'DIS:SwimY' - closest Y bin (only for DIS processes)

DIS	
DoSwimming	*logical* .true., .false. Whether to do swimming for DIS datasets
MakeDataset	*logical* .true., .false. Whether to create new datasets
LCOMCME	*logical* .true., .false. Whether to correct CME to the common CME
CMEYREF	*real* The value of the reference CME for calculation of reference y
Yref	*real* The value of reference y
CorrYrefSwim	*logical* .true., .false. Whether to calculate reference y using the found grid bin values
DISoutput	*logical* .true., .false. Whether to write x, Q^2, y bins on the screen

Table 22: The continuation of the Table 21

```
   Percent = false,false,false

 &END
   1.0     2.0      110.00       5.0       5.0       1.0
   2.0     3.0      200.00       5.0       5.0       1.0
   3.0     4.0      300.00       5.0       5.0       1.0
   4.0     5.0      400.00       5.0       5.0       1.0
```

The content of the this simplest dataset is intuitively clear. It is only need to mention that names of columns of the 'Errors' make sense because the same `'ColumnName'`s mark the same correlated uncertainties across different files and processes. The field `Percent` indicates the type of uncertainties: absolute (false) or relative (true).

9.1.6 Grid file

The grid file contains all possible bins which will be used for search of the common bins for different measurements.

```
&Grid
  Reaction = 'Z'          !> name of the reaction
  NDimension = 2          !> number of dimensions (columns) of the grid
  NPoints = 6             !> full number of ponts of the common grid
  BinNames = 'M1','M2'    !> names of the bin-columns
&End
  1.0   2.0
  2.0   3.0
  3.0   4.0
  4.0   5.0
  5.0   6.0
  6.0   7.0
```

The header consists of several fields and the first field is crucial because it defines the reaction for which this grid will be used.

9.1.7 Swimming corrections

For the DIS dataset the swimming corrections are calculated using the theory packages implemented in the `HERAFitter`. To perform the swimming correction it is necessary to export the environment variable `HERAFITTER` which will be point out inside the main directory of the fitting package. To enable the corrections in the averaging procedure define the options

DoSwimming and MakeDataset as .true.. The swimming procedure is as follows. The temporary datasets for the initial and swimmed bins and the corresponding steering files are generated in the directory ./script. The executable file DoSwimming is automatically launched in the same directory. This file executes the HERAFitter two times and obtains the text files with theoretical cross sections for the initial and swimmed bins. These cross sections are red by the HERAverager and the swimming correction is performed.

9.1.8 Output

The results of the averaging are printed out in the text files ALLEXP_FirstDimBin.dat, where the FirstDimBin are the values of the bins corresponding to the first dimension of each reaction. The example of the output file for DIS processes is listed below. (The right part is transfered at the bottom)

```
#      Q^2          x              y           Sigma_ave        dSigma_tot
   1.500000      3.4749199E-05  0.8526708      0.5181571      5.3659040E-02
   1.500000      2.7865000E-05  0.8544463      0.6631654      7.5363949E-02

~ transfer of the right part ~

   Sigma_1        dSigma_tot     Sigma_2        dSigma_tot
 0.5198570      5.6774933E-02   0.000000       0.000000
 0.6623530      7.9744279E-02   0.000000       0.000000
```

The first three columns represent the bins and other show the averaged value, total uncertainty of the averaged value, the data point for the first experiment, total uncertainty of data point for the first experiment, and so on for the second, third...

The plots of the resulted averaged data together with the initial data points can be made using the gnuplot and the dedicated script:

```
>gnuplot allexp.plt
```

9.2 Table of the combined reduced cross sections

Q^2, GeV^2	x	y	σ	δ_{stat}, %	δ_{unc} , %	δ_{corr} , %	δ_{tot} , %
1.50	0.0000279	0.850	0.664	9.35	4.94	4.14	11.35
1.50	0.0000347	0.852	0.520	8.10	4.96	4.09	10.34
2.00	0.0000372	0.850	0.759	6.37	4.34	3.49	8.46
2.00	0.0000410	0.769	0.662	7.44	3.97	3.19	9.02
2.00	0.0000463	0.852	0.707	4.56	4.31	3.37	7.12
2.00	0.0000525	0.751	0.718	4.59	3.93	2.62	6.58
2.50	0.0000464	0.850	0.827	5.44	4.12	3.35	7.60
2.50	0.0000513	0.769	0.831	3.87	3.10	2.34	5.48
2.50	0.0000579	0.681	0.759	5.01	3.14	2.08	6.27
2.50	0.0000579	0.852	0.781	4.17	4.16	3.52	6.86
2.50	0.0000656	0.751	0.766	2.64	3.03	2.28	4.62
2.50	0.0000781	0.631	0.709	4.32	3.45	2.56	6.09
3.50	0.0001094	0.505	0.948	5.41	3.27	2.71	6.87
3.50	0.0001094	0.631	0.855	2.03	2.47	2.45	4.03
3.50	0.0001436	0.481	0.798	2.55	2.45	3.38	4.89
3.50	0.0000650	0.850	0.871	5.56	4.05	3.42	7.69
3.50	0.0000718	0.769	0.868	3.52	2.92	2.46	5.19
3.50	0.0000811	0.681	0.865	3.16	2.49	2.62	4.80
3.50	0.0000811	0.852	0.793	4.21	4.05	3.20	6.66
3.50	0.0000919	0.601	0.930	3.38	2.66	2.17	4.81
3.50	0.0000919	0.751	0.820	2.22	2.86	2.44	4.37
5.00	0.0001026	0.769	0.875	3.53	2.84	2.24	5.06
5.00	0.0001158	0.681	0.997	2.67	2.37	2.20	4.20
5.00	0.0001158	0.852	0.942	4.18	4.01	3.44	6.74
5.00	0.0001313	0.601	0.939	2.61	2.37	2.23	4.17
5.00	0.0001313	0.751	0.922	2.07	2.80	2.31	4.18
5.00	0.0001563	0.505	1.002	2.44	2.04	2.79	4.23
5.00	0.0001563	0.631	0.962	1.69	2.33	2.20	3.62
5.00	0.0002051	0.385	0.930	2.59	2.06	2.30	4.03
5.00	0.0002051	0.481	0.909	1.16	1.87	2.23	3.13
5.00	0.0000929	0.850	0.846	6.49	3.99	3.55	8.41

Table 23: The combined cross section for the reduced proton beam energy $E_p = 460, 575$ GeV. The statistical, uncorrelated systematic and correlated systematic uncertainties are given. The total uncertainty squared is the sum of these uncertainties taken in quadrature.

Q^2, GeV^2	x	y	σ	δ_{stat}, %	δ_{unc} , %	δ_{corr} , %	δ_{tot} , %
6.50	0.0001207	0.850	0.897	7.20	4.03	3.92	9.14
6.50	0.0001333	0.769	0.982	3.50	2.85	2.25	5.04
6.50	0.0001506	0.681	1.059	2.57	2.35	2.18	4.11
6.50	0.0001506	0.852	1.033	4.26	4.02	3.44	6.80
6.50	0.0001707	0.601	1.039	2.31	2.32	2.18	3.94
6.50	0.0001707	0.751	0.954	2.15	2.80	2.25	4.19
6.50	0.0002032	0.505	1.092	2.06	1.96	2.19	3.59
6.50	0.0002032	0.631	1.000	1.60	2.30	2.09	3.49
6.50	0.0002667	0.385	0.989	1.39	1.83	2.14	3.14
6.50	0.0002667	0.481	1.001	0.90	1.82	2.10	2.92
6.50	0.0004129	0.250	0.963	1.14	1.87	2.19	3.10
8.50	0.0012875	0.105	0.855	1.16	1.45	2.19	2.87
8.50	0.0001579	0.850	0.975	7.10	4.00	4.43	9.28
8.50	0.0001744	0.769	1.057	3.84	2.90	2.24	5.30
8.50	0.0001969	0.681	1.083	2.81	2.39	2.20	4.30
8.50	0.0001969	0.852	0.970	4.68	4.01	3.87	7.27
8.50	0.0002232	0.601	1.090	2.33	2.33	2.09	3.90
8.50	0.0002232	0.751	1.003	2.39	2.84	2.24	4.34
8.50	0.0002657	0.505	1.020	2.04	1.93	2.23	3.58
8.50	0.0002657	0.631	1.081	1.66	2.32	2.28	3.65
8.50	0.0003487	0.385	1.072	1.21	1.81	2.08	3.01
8.50	0.0003487	0.481	1.044	0.85	1.81	2.12	2.92
8.50	0.0005399	0.250	1.009	0.78	1.30	2.02	2.52
8.50	0.0007608	0.177	0.952	0.86	1.31	2.09	2.62
12.00	0.0010741	0.177	1.007	0.78	1.30	2.06	2.55
12.00	0.0018177	0.105	0.889	1.04	1.40	2.19	2.81
12.00	0.0002229	0.850	1.235	5.52	4.00	3.44	7.63
12.00	0.0002461	0.769	1.074	4.08	2.91	2.30	5.51
12.00	0.0002780	0.681	1.152	3.09	2.43	2.19	4.50
12.00	0.0002780	0.852	1.126	3.90	3.98	3.09	6.37
12.00	0.0003151	0.601	1.174	2.57	2.37	2.17	4.11
12.00	0.0003151	0.751	1.107	2.38	2.85	2.24	4.34
12.00	0.0003751	0.505	1.156	2.13	1.96	2.08	3.56
12.00	0.0003751	0.631	1.086	1.87	2.36	2.10	3.67
12.00	0.0004923	0.385	1.111	1.20	1.81	2.07	3.00
12.00	0.0004923	0.481	1.098	0.89	1.81	2.10	2.92
12.00	0.0007622	0.250	1.033	0.74	1.29	2.04	2.53

Table 24: The continuation of Table 23.

Q^2, GeV^2	x	y	σ	δ_{stat}, %	δ_{unc} , %	δ_{corr} , %	δ_{tot} , %
15.00	0.0013426	0.177	0.968	0.80	1.30	2.09	2.59
15.00	0.0022721	0.105	0.870	1.02	1.39	2.23	2.82
15.00	0.0002787	0.850	1.104	6.33	4.04	3.11	8.12
15.00	0.0003077	0.769	1.280	3.42	2.90	2.14	4.97
15.00	0.0003475	0.681	1.211	3.20	2.47	2.06	4.54
15.00	0.0003475	0.852	1.214	3.91	4.06	2.68	6.24
15.00	0.0003938	0.601	1.142	2.99	2.43	2.11	4.39
15.00	0.0003938	0.751	1.103	2.34	2.84	2.14	4.25
15.00	0.0004688	0.505	1.238	2.34	2.01	2.64	4.06
15.00	0.0004688	0.631	1.131	2.05	2.40	2.21	3.85
15.00	0.0006154	0.385	1.145	1.30	1.82	2.13	3.09
15.00	0.0006154	0.481	1.153	0.96	1.83	2.14	2.98
15.00	0.0009528	0.250	1.039	0.77	1.29	2.03	2.53
20.00	0.0012704	0.250	1.083	0.84	1.31	2.07	2.59
20.00	0.0017901	0.177	0.999	0.86	1.32	2.07	2.60
20.00	0.0030294	0.105	0.879	1.10	1.42	2.12	2.78
20.00	0.0003715	0.850	1.283	6.60	4.25	2.92	8.37
20.00	0.0004102	0.769	1.234	3.67	2.93	2.16	5.17
20.00	0.0004633	0.681	1.276	3.06	2.46	2.06	4.43
20.00	0.0004633	0.852	1.002	5.34	4.21	2.74	7.33
20.00	0.0005251	0.601	1.123	3.19	2.46	2.12	4.55
20.00	0.0005251	0.751	1.196	2.27	2.87	2.16	4.25
20.00	0.0006251	0.505	1.207	2.58	2.06	2.98	4.45
20.00	0.0006251	0.631	1.167	1.98	2.39	2.06	3.72
20.00	0.0008205	0.385	1.192	1.42	1.84	2.09	3.13
20.00	0.0008205	0.481	1.156	1.06	1.85	2.14	3.02

Table 25: The continuation of Table 23.

Q^2, GeV^2	x	y	σ	δ_{stat}, %	δ_{unc} , %	δ_{corr} , %	δ_{tot} , %
24.00	0.0011815	0.321	1.128	2.13	1.00	2.28	3.27
24.00	0.0011815	0.401	1.172	1.61	0.70	2.28	2.87
24.00	0.0015245	0.250	1.113	0.82	0.65	2.10	2.34
24.00	0.0021481	0.177	1.038	0.89	0.82	2.19	2.51
24.00	0.0036353	0.105	0.874	0.98	0.75	2.24	2.56
24.00	0.0004923	0.769	1.284	2.82	1.95	2.61	4.31
24.00	0.0005560	0.681	1.380	3.26	1.80	2.86	4.70
24.00	0.0005907	0.641	1.288	1.85	1.50	2.23	3.26
24.00	0.0005907	0.801	1.202	2.43	2.94	2.18	4.39
24.00	0.0006301	0.751	1.234	2.92	2.10	4.18	5.51
24.00	0.0006849	0.553	1.327	2.39	1.30	3.12	4.14
24.00	0.0006849	0.691	1.252	2.51	1.60	2.81	4.09
24.00	0.0007501	0.505	1.268	1.70	1.08	2.16	2.95
24.00	0.0007501	0.631	1.229	1.56	1.25	2.22	2.98
24.00	0.0008439	0.561	1.263	1.70	0.90	2.24	2.95
24.00	0.0009846	0.385	1.233	1.32	1.04	2.08	2.67
24.00	0.0009846	0.481	1.197	1.08	0.92	2.21	2.62
32.00	0.0010002	0.505	1.301	1.79	1.08	2.07	2.94
32.00	0.0010002	0.631	1.242	1.75	1.39	2.11	3.08
32.00	0.0011252	0.561	1.259	1.99	1.00	2.15	3.10
32.00	0.0013127	0.385	1.219	1.33	1.03	2.06	2.66
32.00	0.0013127	0.481	1.197	1.12	0.95	2.05	2.53
32.00	0.0015753	0.321	1.152	1.91	0.90	2.49	3.26
32.00	0.0015753	0.401	1.157	1.60	0.70	2.04	2.68
32.00	0.0020326	0.250	1.097	0.79	0.55	2.02	2.24
32.00	0.0028642	0.177	0.999	0.88	0.65	2.10	2.37
32.00	0.0048471	0.105	0.858	0.85	0.51	2.15	2.37
32.00	0.0006564	0.769	1.333	3.72	2.19	2.67	5.07
32.00	0.0007413	0.681	1.302	2.65	1.71	2.28	3.89
32.00	0.0007876	0.641	1.378	3.41	1.90	2.50	4.63
32.00	0.0008402	0.601	1.327	3.14	2.52	2.08	4.53
32.00	0.0008402	0.751	1.206	2.52	1.92	2.50	4.04
32.00	0.0009132	0.553	1.240	2.73	1.40	2.45	3.92
32.00	0.0009132	0.691	1.379	2.81	1.70	2.79	4.31

Table 26: The continuation of Table 23.

Q^2, GeV^2	x	y	σ	δ_{stat}, %	δ_{unc} , %	δ_{corr} , %	δ_{tot} , %
45.00	0.0010425	0.681	1.362	3.54	1.96	2.28	4.64
45.00	0.0011076	0.641	1.367	3.83	2.20	2.79	5.22
45.00	0.0011815	0.601	1.251	3.82	2.68	2.08	5.11
45.00	0.0011815	0.751	1.180	3.77	2.40	2.95	5.36
45.00	0.0012842	0.553	1.289	3.04	1.50	2.22	4.05
45.00	0.0012842	0.691	1.219	3.21	1.90	2.42	4.45
45.00	0.0014065	0.505	1.266	2.05	1.17	2.08	3.15
45.00	0.0014065	0.631	1.261	2.13	1.36	2.14	3.31
45.00	0.0015823	0.561	1.271	2.19	1.20	2.40	3.47
45.00	0.0018460	0.385	1.161	1.44	1.09	2.08	2.75
45.00	0.0018460	0.481	1.145	1.20	1.05	2.02	2.57
45.00	0.0022153	0.321	1.119	1.91	0.90	2.20	3.05
45.00	0.0022153	0.401	1.102	1.70	0.80	2.09	2.81
45.00	0.0028584	0.250	1.081	0.81	0.58	2.00	2.24
45.00	0.0040278	0.177	0.971	0.89	0.65	2.10	2.37
45.00	0.0068162	0.105	0.826	0.80	0.44	2.12	2.31
45.00	0.0009230	0.769	1.380	4.73	2.60	2.67	6.02
60.00	0.0012307	0.769	1.402	5.69	3.10	3.17	7.21
60.00	0.0013900	0.681	1.319	5.16	3.10	2.94	6.70
60.00	0.0014768	0.641	1.451	4.35	2.30	2.30	5.43
60.00	0.0015753	0.601	1.276	8.45	4.22	2.30	9.72
60.00	0.0015753	0.751	1.250	4.15	2.40	2.86	5.59
60.00	0.0017123	0.553	1.269	3.61	1.80	2.35	4.66
60.00	0.0017123	0.691	1.319	3.66	2.20	2.59	4.99
60.00	0.0018754	0.505	1.178	2.61	1.31	2.10	3.60
60.00	0.0018754	0.631	1.249	3.35	1.80	2.63	4.63
60.00	0.0021098	0.561	1.125	2.70	1.30	2.32	3.79
60.00	0.0024614	0.385	1.153	1.64	1.21	1.97	2.83
60.00	0.0024614	0.481	1.159	1.43	1.18	2.03	2.75
60.00	0.0029537	0.321	1.126	2.31	1.10	2.12	3.32
60.00	0.0029537	0.401	1.075	2.09	0.90	2.05	3.06
60.00	0.0038112	0.250	1.021	0.93	0.65	1.99	2.29
60.00	0.0053703	0.177	0.935	0.98	0.72	2.13	2.45
60.00	0.0090883	0.105	0.772	0.88	0.51	2.09	2.32

Table 27: The continuation of Table 23.

Q^2, GeV^2	x	y	σ	δ_{stat}, %	δ_{unc} , %	δ_{corr} , %	δ_{tot} , %
80.00	0.0121177	0.105	0.710	1.27	0.57	2.04	2.47
80.00	0.0016409	0.769	1.390	6.46	3.60	3.08	8.01
80.00	0.0018533	0.681	1.243	6.17	3.70	2.63	7.66
80.00	0.0019691	0.641	1.252	5.49	2.90	2.45	6.68
80.00	0.0021004	0.751	1.269	4.75	2.90	3.50	6.57
80.00	0.0022830	0.553	1.184	4.25	2.20	2.69	5.49
80.00	0.0022830	0.691	1.087	4.77	3.40	3.24	6.69
80.00	0.0025005	0.505	1.162	3.73	1.80	2.45	4.82
80.00	0.0025005	0.631	1.124	3.98	2.00	2.58	5.15
80.00	0.0028130	0.561	1.124	3.07	1.60	2.74	4.41
80.00	0.0032819	0.385	1.079	3.22	1.50	2.28	4.23
80.00	0.0032819	0.481	1.084	2.79	1.40	2.12	3.78
80.00	0.0039382	0.321	1.076	2.70	1.30	2.03	3.62
80.00	0.0039382	0.401	1.017	2.40	1.10	2.28	3.49
80.00	0.0050816	0.250	0.975	1.50	0.70	2.02	2.61
80.00	0.0071604	0.177	0.912	1.67	0.80	2.17	2.85
90.00	0.0136324	0.105	0.740	1.74	1.67	2.05	3.17
90.00	0.0036921	0.385	1.125	2.93	2.17	2.06	4.19
90.00	0.0036921	0.481	1.087	3.37	2.72	2.13	4.82
90.00	0.0057168	0.250	0.945	1.44	1.45	2.01	2.87
90.00	0.0080555	0.177	0.868	1.40	1.45	2.05	2.87
110.00	0.0166618	0.105	0.683	1.43	0.65	2.07	2.60
110.00	0.0022563	0.769	1.397	10.74	6.20	4.22	13.10
110.00	0.0025483	0.681	1.066	8.07	4.10	3.76	9.80
110.00	0.0027075	0.641	1.151	6.54	3.40	2.38	7.74
110.00	0.0028881	0.751	0.912	9.42	5.20	4.38	11.62
110.00	0.0031392	0.553	1.143	5.10	2.70	3.11	6.56
110.00	0.0031392	0.691	1.174	5.32	3.20	2.60	6.74
110.00	0.0034382	0.505	1.074	4.51	2.30	2.56	5.67
110.00	0.0034382	0.631	1.112	4.84	2.80	2.66	6.20
110.00	0.0038679	0.561	1.053	3.75	1.70	2.91	5.05
110.00	0.0045126	0.385	1.059	3.81	1.80	2.48	4.89
110.00	0.0045126	0.481	1.076	3.17	1.50	2.17	4.12
110.00	0.0054151	0.321	0.987	3.19	1.50	2.12	4.11
110.00	0.0054151	0.401	0.976	2.88	1.20	2.29	3.87
110.00	0.0069872	0.250	0.880	1.80	0.84	2.09	2.88
110.00	0.0098456	0.177	0.834	1.98	0.90	2.18	3.08

Table 28: The continuation of Table 23.

9.3 Table of F_L data

Q^2, GeV^2	x	y	F_L	Δ_{stat}	Δ_{unc}	Δ_{corr}	Δ_{tot}
1.50	0.0000279	0.848	0.089	0.114	0.190	0.061	0.229
2.00	0.0000372	0.848	0.110	0.069	0.132	0.065	0.163
2.00	0.0000410	0.761	0.443	0.111	0.185	0.076	0.229
2.00	0.0000463	0.850	0.041	0.052	0.105	0.034	0.122
2.50	0.0000464	0.848	0.018	0.057	0.121	0.047	0.142
2.50	0.0000513	0.760	0.110	0.062	0.130	0.044	0.151
2.50	0.0000579	0.850	0.178	0.047	0.090	0.062	0.119
2.50	0.0000656	0.750	0.174	0.043	0.099	0.067	0.127
2.50	0.0000781	0.650	0.417	0.096	0.157	0.082	0.201
3.50	0.0001094	0.650	0.162	0.049	0.124	0.047	0.141
3.50	0.0001436	0.490	0.727	0.112	0.227	0.145	0.292
3.50	0.0000650	0.848	0.132	0.065	0.136	0.054	0.160
3.50	0.0000718	0.760	0.207	0.061	0.134	0.049	0.155
3.50	0.0000811	0.850	0.255	0.044	0.094	0.044	0.113
3.50	0.0000919	0.750	0.239	0.037	0.099	0.042	0.114
5.00	0.0001026	0.760	0.348	0.065	0.144	0.047	0.165
5.00	0.0001158	0.850	0.265	0.048	0.109	0.051	0.130
5.00	0.0001313	0.750	0.316	0.037	0.110	0.043	0.124
5.00	0.0001563	0.650	0.215	0.044	0.134	0.049	0.150
5.00	0.0002051	0.490	0.554	0.057	0.206	0.087	0.231
5.00	0.0000929	0.848	0.413	0.081	0.164	0.072	0.197
6.50	0.0001207	0.848	0.433	0.097	0.182	0.082	0.222
6.50	0.0001333	0.760	0.204	0.071	0.152	0.045	0.174
6.50	0.0001506	0.850	0.138	0.051	0.114	0.057	0.138
6.50	0.0001707	0.750	0.364	0.040	0.120	0.048	0.135
6.50	0.0002032	0.650	0.310	0.044	0.146	0.062	0.164
6.50	0.0002667	0.490	0.207	0.046	0.208	0.099	0.235
8.50	0.0001579	0.848	0.514	0.109	0.200	0.102	0.249
8.50	0.0001744	0.760	0.490	0.089	0.187	0.058	0.215
8.50	0.0001969	0.850	0.275	0.057	0.124	0.062	0.150
8.50	0.0002232	0.750	0.250	0.045	0.126	0.045	0.141
8.50	0.0002657	0.650	-0.126	0.045	0.140	0.054	0.157
8.50	0.0003487	0.490	0.185	0.045	0.220	0.098	0.245

Table 29: The obtained values of the longitudinal structure function F_L. The absolute statistical, uncorrelated systematic and correlated systematic uncertainties are also given. The total uncertainty squared is the sum of these uncertainties taken in quadrature.

Q^2, GeV^2	x	y	F_L	Δ_{stat}	Δ_{unc}	Δ_{corr}	Δ_{tot}
12.00	0.0002229	0.848	0.107	0.101	0.162	0.089	0.211
12.00	0.0002461	0.760	0.569	0.099	0.158	0.061	0.197
12.00	0.0002780	0.850	0.289	0.059	0.099	0.050	0.125
12.00	0.0003151	0.750	0.260	0.050	0.100	0.039	0.119
12.00	0.0003751	0.650	0.435	0.055	0.121	0.044	0.140
12.00	0.0004923	0.490	0.432	0.049	0.163	0.068	0.184
15.00	0.0002787	0.848	0.532	0.110	0.188	0.091	0.236
15.00	0.0003077	0.760	0.157	0.088	0.152	0.054	0.184
15.00	0.0003475	0.850	0.192	0.061	0.100	0.042	0.124
15.00	0.0003938	0.750	0.425	0.051	0.100	0.038	0.119
15.00	0.0004688	0.650	0.261	0.062	0.118	0.047	0.141
15.00	0.0006154	0.490	0.071	0.054	0.158	0.071	0.181
20.00	0.0003715	0.848	0.234	0.117	0.202	0.069	0.243
20.00	0.0004102	0.760	0.341	0.093	0.161	0.046	0.192
20.00	0.0004633	0.850	0.418	0.070	0.109	0.040	0.136
20.00	0.0005251	0.750	0.372	0.052	0.104	0.039	0.123
20.00	0.0006251	0.650	0.284	0.062	0.119	0.045	0.142
20.00	0.0008205	0.490	0.219	0.060	0.164	0.070	0.188
24.00	0.0004923	0.800	0.290	0.062	0.125	0.065	0.154
24.00	0.0005907	0.800	0.249	0.041	0.085	0.036	0.101
24.00	0.0007501	0.650	0.205	0.053	0.095	0.056	0.122
24.00	0.0009846	0.490	0.045	0.057	0.127	0.077	0.159
32.00	0.0010002	0.650	0.112	0.060	0.104	0.046	0.128
32.00	0.0013127	0.490	0.028	0.059	0.132	0.072	0.161
32.00	0.0006564	0.760	0.175	0.104	0.152	0.071	0.197
32.00	0.0007413	0.690	0.271	0.095	0.145	0.063	0.184
32.00	0.0008402	0.751	0.278	0.062	0.090	0.049	0.120
45.00	0.0010425	0.689	0.030	0.124	0.167	0.054	0.215
45.00	0.0011815	0.752	0.362	0.087	0.110	0.065	0.155
45.00	0.0012842	0.688	0.396	0.119	0.355	0.095	0.386
45.00	0.0014065	0.650	0.170	0.078	0.113	0.055	0.148
45.00	0.0018460	0.490	0.276	0.066	0.141	0.070	0.170
45.00	0.0028584	0.310	-0.380	0.156	0.307	0.129	0.367
45.00	0.0009230	0.750	0.104	0.130	0.190	0.075	0.242

Table 30: The continuation of Table 29.

Q^2, GeV^2	x	y	F_L	Δ_{stat}	Δ_{unc}	Δ_{corr}	Δ_{tot}
60.00	0.0011146	0.530	0.290	0.275	1.008	0.003	1.045
60.00	0.0012307	0.752	0.192	0.162	0.230	0.098	0.298
60.00	0.0013900	0.691	0.210	0.164	0.236	0.097	0.303
60.00	0.0014768	0.631	0.316	0.282	1.034	0.005	1.072
60.00	0.0015753	0.749	0.106	0.107	0.112	0.060	0.167
60.00	0.0017123	0.692	-0.252	0.135	0.367	0.105	0.404
60.00	0.0018754	0.630	0.095	0.117	0.140	0.069	0.195
60.00	0.0021098	0.561	0.240	0.196	1.034	0.004	1.052
60.00	0.0024614	0.490	0.096	0.082	0.151	0.071	0.185
60.00	0.0029537	0.400	0.697	0.284	0.533	0.101	0.613
60.00	0.0038112	0.310	0.270	0.177	0.330	0.127	0.395
60.00	0.0053703	0.220	1.012	0.363	0.498	0.220	0.655
60.00	0.0090883	0.130	1.315	0.685	0.557	0.156	0.896
80.00	0.0121177	0.130	0.141	0.857	0.513	0.002	0.999
80.00	0.0016409	0.752	0.318	0.260	1.085	0.009	1.116
80.00	0.0018533	0.690	0.274	0.258	1.061	0.006	1.092
80.00	0.0019691	0.631	0.273	0.306	1.028	0.005	1.072
80.00	0.0021004	0.752	0.293	0.168	1.103	0.009	1.116
80.00	0.0022830	0.689	0.540	0.146	0.479	0.174	0.530
80.00	0.0025005	0.631	0.190	0.175	0.354	0.083	0.403
80.00	0.0028130	0.560	0.239	0.210	1.031	0.005	1.052
80.00	0.0032819	0.480	0.051	0.232	0.593	0.151	0.655
80.00	0.0039382	0.401	0.684	0.301	0.567	0.140	0.657
80.00	0.0050816	0.310	0.445	0.406	0.560	0.150	0.708
80.00	0.0071604	0.220	0.186	0.658	0.756	0.003	1.003
90.00	0.0136324	0.120	0.313	0.869	0.422	0.053	0.968
90.00	0.0018460	0.475	0.274	0.603	0.839	0.003	1.033
90.00	0.0020849	0.425	0.267	0.486	0.902	0.002	1.025
90.00	0.0023629	0.375	0.246	0.465	0.905	0.002	1.017
90.00	0.0028130	0.325	0.260	0.492	0.883	0.002	1.011
90.00	0.0036921	0.490	0.156	0.168	0.242	0.064	0.301
90.00	0.0057168	0.310	0.480	0.247	0.435	0.121	0.515
90.00	0.0080555	0.200	0.519	0.509	0.634	0.113	0.821

Table 31: The continuation of Table 29.

Q^2, GeV^2	x	y	F_L	Δ_{stat}	Δ_{unc}	Δ_{corr}	Δ_{tot}
110.00	0.0166618	0.131	0.010	0.819	0.417	0.131	0.928
110.00	0.0022563	0.752	0.319	0.405	1.040	0.013	1.116
110.00	0.0025483	0.692	0.236	0.316	1.046	0.008	1.092
110.00	0.0027075	0.631	0.251	0.335	1.018	0.004	1.072
110.00	0.0028881	0.751	0.208	0.251	1.087	0.009	1.115
110.00	0.0031392	0.691	-0.071	0.173	0.466	0.109	0.509
110.00	0.0034382	0.631	0.140	0.183	0.280	0.083	0.344
110.00	0.0038679	0.561	0.227	0.262	1.019	0.006	1.052
110.00	0.0045126	0.480	-0.133	0.209	0.223	0.095	0.320
110.00	0.0054151	0.400	0.254	0.347	0.575	0.139	0.686
110.00	0.0069872	0.310	0.557	0.365	0.359	0.135	0.530
110.00	0.0098456	0.220	0.725	0.579	0.426	0.179	0.741
150.00	0.0147684	0.100	0.149	0.993	0.096	0.002	0.998
150.00	0.0246141	0.060	0.136	0.996	0.042	0.002	0.997
150.00	0.0092303	0.155	0.185	0.989	0.148	0.002	1.000

Table 32: The continuation of Table 29.

References

[1] S.L. Glashow, *Partial-symmetries of weak interactions*. Nucl. Phys. **22**, 579 (1961)
S. Weinberg, *A model of leptons*. Phys. Rev. Lett. **19**, 1264 (1967)
A. Salam, *Weak and electromagnetic interactions*. Proc. 8th Nobel Sympos. Almqvist and Wiksell, Stockholm, p. 367, 1968

[2] J.D. Bjorken and S.D. Drell, *Relativistic Quantum Mechanics*. McGraw-Hill Inc., 300 p., 1964

[3] D.J. Gross and F. Wilczek, *Ultraviolet behavior of non-abelian gauge theories*. Phys. Rev. Lett. **30**, 1343 (1973)
D.J. Gross and F. Wilczek, *Asymptotically free gauge theories*. Phys. Rev. D. **8**, 3633 (1973)
S. Weinberg, *Non-abelian gauge theories of the strong interactions*. Phys. Rev. Lett. **31**, 494 (1973)
H.D. Politzer, *Asymptotic freedom: an approach to strong interactions*. Phys. Rept. **14**, 129 (1974)

[4] F. Englert and R. Brout, *Broken symmetry and the mass of gauge vector mesons*. Phys. Rev. Lett. **13**, 321 (1964)
P.W. Higgs, *Broken symmetries and the mass of gauge bosons*. Phys. Rev. Lett. **13**, 508 (1964)
G.S. Guralnik, C.R. Hagen, and T.W.B. Kibble, *Global conservation laws and massless particles*. Phys. Rev. Lett. **13**, 585 (1964)

[5] G. Aad *et al.* [ATLAS Collaboration], *Observation of a new particle in the search for the Standard Model Higgs boson with the ATLAS detector at the LHC*. Phys. Lett. B. **716**, 1 (2012)
S. Chatrchyan *et al.* [CMS Collaboration], *Observation of a new boson at a mass of 125 GeV with the CMS experiment at the LHC*. Phys. Lett. B. **716**, 30 (2012)

[6] E. Rutherford, *The scattering of alpha and beta particles by matter and the structure of the atom*. Phil. Mag. **21**, 669 (1911)

[7] R. Hofstadter, *The Electron Scattering Method and its Application to the Structure of Nuclei and Nucleons*. Nob. Lect. Phys. 1942-1962. Elsevier Pub. Co., Amsterdam, p. 560, 1961

[8] E.D. Bloom *et al.*, *High-energy inelastic $e-p$ scattering at 6° and 10°*. Phys. Rev. Lett. **23**, 930 (1969)

M. Breidenbach *et al.*, *Observed behavior of highly inelastic electron-proton scattering*. Phys. Rev. Lett. **23**, 935 (1969)

[9] R.P. Feynman, *Very high-energy collisions of hadrons*. Phys. Rev. Lett. **23**, 1415 (1969)

[10] R. Brandelik *et al.* [TASSO Collaboration], *Evidence for planar events in e^+e^- annihilation at high energies*. Phys. Lett. B. **86**, 243 (1979)

[11] A. Bodek *et al.*, *Experimental studies of the neutron and proton electromagnetic structure functions*. Phys. Rev. D. **20**, 1471 (1979)

[12] J. Beringer *et al.*, *Review of Particle Physics*. Phys. Rev. D. **86**, 010001 (2012) (available at [http://pdg.lbl.gov/2012/reviews/rpp2012-rev-qcd.pdf])

[13] J.D. Bjorken and E.A. Paschos, *Inelastic electron-proton and γ-proton scattering and the structure of the nucleon*. Phys. Rev. **185**, 1975 (1969)

[14] R.G. Roberts. *The Structure of The Proton: Deep Inelastic Scattering*, Cambridge University Press, 182 p., 1990

[15] R. Devenish and A. Cooper-Sarkar. *Deep Inelastic Scattering*, Oxford University Press, 403 p., 2004

[16] D.W. Duke, J.P. Kimel, G.A. Sowell, *Fourth-order quantum-chromodynamic correction to the longitudinal coefficient function in deep-inelastic scattering*. Phys. Rev. D. **25**, 71 (1982)

[17] J.D. Bjorken, *Asymptotic sum rules at infinite momentum*. Phys. Rev. **179**, 1547 (1969)

[18] C. Adloff *et al.* [H1 Collaboration], *Measurement and QCD analysis of neutral and charged current cross sections at HERA*. Eur. Phys. J. C. **30**, 1 (2003)

[19] A.C. Benvenuti *et al.* [BCDMS Collaboration], *A high statistics measurement of the proton structure functions $F^2(x, Q^2)$ and R from deep inelastic muon scattering at high Q^2*. Phys. Lett. B. **223**, 485 (1989)

[20] M. Arneodo *et al.* [NMC Collaboration], *Measurement of the proton and the deutron structure functions, F_2^p and F_2^d*. Phys. Lett. B. **364**, 107 (1995)

[21] F. Halzen and A. Martin. *Quarks and leptons*, John Wiley and songs Inc., 396 p., 1984

[22] C.G. Callan and D.J. Gross, *High-energy electroproduction and the constitution of the electric current*. Phys. Rev. Lett. **22**, 156 (1969)

[23] D.J. Gross and C.H. Llewellyn Smith, *High-energy neutrino-nucleon scattering, current algebra and partons*. Nucl. Phys. B. **14**, 337 (1969)

[24] S.L. Adler, *Sum rules giving tests of local current commutation relations in high-energy neutrino reactions*. Phys. Rev. **143**, 1144 (1969)

[25] M. Botje, *A QCD analysis of HERA and fixed target structure function data*. Eur. Phys. J. C. **14**, 285 (2000)

[26] M. Peskin and D. Schroeder. *An Introduction to Quantum Field Theory*, Addison-Wesley Publishing Company, 845 p., 1995

[27] J.C. Collins and D.E. Soper. *The Theorems of Perturbative QCD*, Ann. Rev. Nucl. Part. Sci. **37**, 383 (1987)

[28] R.K. Ellis, W.J. Stirling, B.R. Webber. *QCD and Collider Physics*, Oxford University Press, 435 p., 1996

[29] G. Altarelli, R.K. Ellis, G. Martinelli. *Leptoproduction and Drell-Yang processes beyond the leading approximation in chromodynamics*. Nucl. Phys. B. **143**, 521 (1978)

[30] W.A. Bardeen *et al.*, *Deep-inelastic scattering beyond the leading order in asymptotically free gauge theories*. Phys. Rev. D. **18**, 3998 (1978)

[31] G. Altarelli, G. Parisi, *Asymptotic freedom in parton language*. Nucl. Phys. B. **126**, 298 (1977)
Yu. L. Dokshitzer, *Calculation of the structure function for deep inelastic scattering and e^+e^- annihilation by perturbation theory in quantum chromodynamics*. Sov. Phys. JETP **46**, 641 (1977)
L.N. Lipatov, *The parton model and perturbation theory*. Sov. J. Nucl. Phys. **20**, 94 (1975)
V.N. Gribov, L.N. Lipatov, *Deep inelastic ep scattering in perturbation theory*. Sov. J. Nucl. Phys. **15**, 438 (1972)
V.N. Gribov, L.N. Lipatov, *e^+e^- pair annihilation and deep inelastic ep scattering in perturbation theory* Sov. J. Nucl. Phys. **15**, 675 (1972)

[32] G. Dissertori, I.G. Knowles, M. Schmelling. *Quantum Chromodynamics: High Energy Experiments and Theory*, Oxford University Press, 538 p., 2003

[33] G. Altarelli, G. Martinelli, *Transverse momentum of jets in electroproduction from quantum chromodynamics*. Phys. Lett. B. **76**, 89 (1978)

[34] H.-L. Lai *et al.*, *New parton distributions for collider physics*. Phys. Rev. D. **82**, 074024 (2010)
R.D. Ball *et al.*, *A first unbiased global NLO determination of parton distributions and their uncertainties*. Nucl. Phys. B. **838**, 136 (2010)
S. Forte *et al.*, *Heavy-quarks in deep-inelastic scattering*. Nucl. Phys. B. **834**, 116 (2010)
A.D. Martin *et al.*, *Parton distributions for the LHC*. Eur. Phys. J. C. **63**, 189 (2009)
M. Glück *et al.*, *Dynamical parton distributions of the nucleon and very small-x physics*. Eur. Phys. J. C. **53**, 335 (2008)
P. Jimenez-Delgado *et al.*, *Dynamical next-to-next-to-leading order parton distributions*. Phys. Rev. D. **79**, 074023 (2009)
S. Alekhin *et al.*, *3-,4-, and 5-flavor next-to-next-to-leading order parton distribution functions from deep-inelastic-scattering data and at hadron colliders*. Phys. Rev. D. **81**, 014032 (2010)

[35] L.N. Lipatov, *Reggeization of the vector meson and the vacuum singularity in nonabelian gauge theories*. Sov. J. Nucl. Phys. **23**, 338 (1976)
E.A. Kuraev, L.N. Lipatov, V.S. Fadin, *The pomeranchuk singularity in nonabelian gauge theories*. Sov. Phys. JETP **45**, 199 (1977)
Ya.Ya. Balitsky, L.N. Lipatov, *The pomeranchuk singularity in quantum chromodynamics*. Sov. J. Nucl. Phys. **28**, 822 (1978)

[36] T. Jaroszewicz, *Gluonic regge singularities and anomalous dimensions in QCD*. Phys. Lett. B. **116**, 291 (1982)

[37] S. Catani and F. Hautmann, *Quark anomalous dimensions at small x*. Phys. Lett. B. **315**, 157 (1993)
S. Catani and F. Hautmann, *High-energy factorization and small-x deep inelastic scattering beyond leading order*. Nucl. Phys. B. **427**, 475 (1994)

[38] K. Prytz, *Approximate determination of the gluon density at low-x from F_2 scaling violations*. Phys. Lett. B. **311**, 286 (1993)

[39] L.V. Gribov, E.M. Levin, M.G. Ryskin, *Semihard processes in QCD*. Phys. Rep. **100**, 1 (1983)

[40] K. Golec-Biernat, M. Wüsthoff, *Saturation effects in deep inelastic scattering at low Q^2 and its implications on diffraction*. Phys. Rev. D. **59**, 014017 (1998)

[41] E. Iancu, K. Itakura, S. Munier, *Saturation and BFKL dynamics in the HERA data at small-x*. Phys. Lett. B. **590**, 199 (2004)

[42] E. Iancu, A. Leonidov, L. McLerran, *Nonlinear gluon evolution in the color glass condensate: 1*. Nucl. Phys. A. **692**, 583 (2001)
E. Ferreiro *et al.*, *Nonlinear gluon evolution in the color glass condensate: 2*. Nucl. Phys. A. **703**, 489 (2002)

[43] E. Levin, K. Tuchin, *Solution of the evolution equation for high parton density QCD*. Nucl. Phys. B. **573**, 833 (2000)

[44] J. Bartels, K. Golec-Biernat, H. Kowalski, *Modification of the saturation model: Dokshitzer-Gribov-Lipatov-Altarelli-Parisi evolution*. Phys. Rev. D. **66**, 014001 (2002)

[45] HERAFitter project, (available at [www.herafitter.org])

[46] F. James and M. Roos, *Minuit - a system for function minimization and analysis of the parameter errors and correlations*, Comm. Phys. Comm. **10**, 343 (1975)

[47] F. D. Aaron *et al.* [H1 and ZEUS collaborations], *Combined measurement and QCD analysis of the inclusive $e^{\pm}p$ scattering cross sections at HERA*. JHEP. **1001**, 109 (2010)

[48] H1 and ZEUS Collaborations, H1prelim-10-142, ZEUS-prel-10-018 (available at [www-h1.desy.de/h1/www/publications/htmlsplit/H1prelim-10-142.long.html])
H1 and ZEUS Collaborations, H1prelim-11-143, ZEUS-prel-11-010 (available at [www-h1.desy.de/h1/www/publications/htmlsplit/H1prelim-11-143.long.html])

[49] A.D. Martin *et al.*, *MRST2001: partons and α_s from precise deep inelastic scattering and Tevatron jet data*. Eur. Phys. J. C. **23**, 73 (2002)

[50] G. Curci, W. Furmanski, and R. Petronzio, *Evolution of parton densities beyond leading order: The non-singlet case*. Nucl. Phys. B. **175**, 27 (1980)
W. Furmanski and R. Petronzio, *Singlet parton densities beyond leading order*. Phys. Lett. B. **97**, 437 (1980)

[51] S. Moch, J. Vermaseren, and A. Vogt, *The three-loop splitting functions in QCD: the non-singlet case*. Nucl. Phys. B. **688**, 101 (2004)
A. Vogt, S. Moch, and J. Vermaseren, *The three-loop splitting functions in QCD: the singlet case*. Nucl. Phys. B. **691**, 129 (2004)

[52] M. Kramer, F.I. Olness, and D.E. Soper, *Treatment of heavy quarks in deeply inelastic scattering*. Phys. Rev. D. **62**, 096007 (2000)

[53] R.S. Thorne, R.G. Roberts, *Ordered analysis of heavy flavor production in deep-inelastic scattering*. Phys. Rev. D. **57**, 6871 (1998)
R.S. Thorne, *Variable-flavor number scheme for next-to-next-to-leading order*. Phys. Rev. D. **73**, 054019 (2006)

[54] M. Botje, *QCDNUM: Fast QCD evolution and convolution*. Comm. Phys. Comm. **182**, 490 (2011)

[55] J. Feltesse. *The first physics results of HERA*. Talk at the "20th HERA Symposium", DESY, Hamburg, 19 June 2012

[56] P. Schmüser, *The electron-proton colliding beam facility HERA*. Nucl. Instr. and Meth. A **235**, 201 (1985)

[57] A.W. Chao, M. Tigner. *Handbook of accelerator physics and engineering*, World Scientific Publishing Co. Pte. Ltd., Singapore, 672 p., 1999

[58] D. Trines. *Technological challenges of HERA*. Talk at the "20th HERA Symposium", DESY, Hamburg, 19 June 2012

[59] I. Abt *et al.* [H1 Collaboration], *The H1 detector at HERA*. Nucl. Instr. and Meth. A. **386**, 310 (1997)

[60] I. Abt *et al.* [H1 Collaboration], *The tracking, calorimeter and muon detectors of the H1 experiment at HERA*. Nucl. Instr. and Meth. A. **386**, 348 (1997)

[61] B. Andrieu *et al.* [H1 Calorimeter Group], *The H1 liquid argon calorimeter system*. Nucl. Instrum. and Meth. A. **336**, 460 (1993)

[62] R.D. Appuhn *et al.* [H1 SPACAL Group], *The H1 lead/scintillating-fibre calorimeter*. Nucl. Instr. and Meth. A. **386**, 397 (1997)

[63] H. Barwolff *et al.*, *Performance of prototypes of the H1 outer z-drift chamber*. Nucl. Instr. and Meth. A. **283**, 467 (1989)

[64] J. Becker *et al.*, *A vertex trigger based on cylindrical multiwire proportional chambers*. Nucl. Instr. and Meth. A. **586**, 190 (2008)

[65] D. Pitzl *et al.*, *The H1 silicon vertex detector*. Nucl. Instr. and Meth. A. **454**, 334 (2000)

[66] H. Henschel, R. Lahmann, *The backward silicon tracker of the H1 experiment at HERA*. Nucl. Instr. and Meth. A. **453**, 93 (2000)

[67] W. Eick *et al.*, *Development of the H1 backward silicon strip detector*. Nucl. Instr. and Meth. A. **386**, 81 (1997)

[68] M. Nozicka, *The forward and backward silicon trackers of H1*. Nucl. Instr. and Meth. A. **501**, 54 (2003)

[69] F.D. Aaron *et al.* [H1 Collaboration], *Measurement of the inclusive ep scattering cross section at low Q^2 and x at HERA*. Eur. Phys. J. C. **63**, 625 (2009)

[70] F.D. Aaron *et al.* [H1 Collaboration], *A precision measurement of the inclusive ep scattering cross section at HERA*. Eur. Phys. J. C. **64**, 561 (2009)

[71] B. Andrieu *et al.* [H1 Calorimeter Group], *Results from the pion calibration runs of the H1 liquid argon calorimeter and comparisons with simulations*. Nucl. Instr. and Meth. A. **336**, 499 (1993)

[72] R.D. Appuhn *et al.* [H1 SPACAL Group], *Hadronic response and e/π separation with the H1 lead/fibre calorimeter*. Nucl. Instr. and Meth. A. **382**, 395 (1996)

[73] H. Bethe and W. Heitler, *On the stopping of fast particles and on the creation of positive electrons*. Proc. Roy. Soc. A. **146**, 83 (1934)

[74] T. Ahmed *et al.* [H1 Collaboration], *Experimental study of hard photon radiation processes at HERA*. Z. Phys. C. **66**, 529 (1995)

[75] *The ZEUS detector. Status report*. Ed. by Uwe Holm, 1993 (available at `[http://www-zeus.desy.de/bluebook/bluebook.html]`)

[76] M. Derrick *et al.*, *Design and construction of the ZEUS barrel calorimeter*. Nucl. Instr. and Meth. A. **309**, 77 (1991)
A. Andresen *et al.*, *Construction and beam test of the ZEUS forward and rear calorimeter*. Nucl. Instr. and Meth. A. **309**, 101 (1991)

[77] A. Polini *et al.*, *The design and performance of the ZEUS micro vertex detector*. Nucl. Instr. and Meth. A. **581**, 656 (2007)

[78] B. Foster *et al.*, *The design and construction of the ZEUS central tracking detector*. Nucl. Instr. and Meth. A. **338**, 254 (1994)

[79] M. Helbich *et al.*, *The spectrometer system for measuring ZEUS luminosity at HERA*. Nucl. Instr. and Meth. A. **565**, 572 (2006)

[80] S. Bentvelsen *et al. Reconstruction of (x, Q^2) and extraction of structure functions in neutral current scattering at HERA*, *Proceedings of the Workshop "Physics at HERA"* vol. 1, p. 23. DESY, 1992

[81] A. Blondel and F. Jacquet, *Proceedings of the "Study of ep Facility for Europe"*, p. 391. DESY 78/79, 1979

[82] U. Bassler and G. Bernardi, *On the kinematic reconstruction of deep inelastic scattering at HERA*. Nucl. Instr. and Meth. A. **361**, 197 (1995)

[83] U. Bassler and G. Bernardi, *Structure function measurements and kinematic reconstruction at HERA*. Nucl. Instr. and Meth. A. **426**, 583 (1999)

[84] F.D. Aaron *et al.* [H1 Collaboration], *Measurement of the inclusive $e^{\pm}p$ scattering cross section at high inelasticity y and of the structure function F_L*. Eur. Phys. J. C. **71**, 1579 (2011)

[85] A. Glazov, N. Raicevic, and A. Zhokin, *Fast simulation of showers in the H1 calorimeter*. Comp. Phys. Comm. **181**, 1008 (2010)

[86] S. Piec, *Measurement of the proton structure function $F_L(x, Q^2)$ with the H1 detector at HERA*. Doctoral thesis. Humboldt-Universität zu Berlin, 2009

[87] S. Chekanov *et al.* [ZEUS Collaboration], *Measurement of the longitudinal proton structure function at HERA*. Phys. Lett. B. **682**, 8 (2009)

[88] J. Grebenyuk, *Measurement of the longitudinal proton structure function with the ZEUS detector at HERA*. Doctoral thesis. Universität Hamburg, 2010

[89] H. Spiesberger. *HERACLES and DJANGOH*, DESY, Hamburg, 1998

[90] T. Sjöstrand *et al.*, *High-energy-physics event generation with PYTHIA 6.1*. Comp. Phys. Comm. **135**, 238 (2001)

[91] H.L. Lai *et al.*, *Global QCD analysis of parton structure of the nucleon: CTEQ5 parton distributions*. Eur. Phys. J. C. **12**, 375 (2000)

[92] A. Glazov, *Averaging of DIS cross section data*. AIP Conf. Proc. **792**, 237 (2005)

[93] R. L. Branham. *Scientific Data Analysis: an introduction to overdetermined systems.* Springer-Verlag, New-York, 238 p., 1990

[94] H. Jeffreys. *Theory of probability.* Oxford University Press, London, 447 p., 1961

[95] W. Feller. *An introduction to probability theory and its applications* Wiley, New-York, Vol. 1, 528 p., 1968

[96] A. Luszczak, *Dipole model + valence quarks analysis of data within the HERAFitter framework*. Talk at "Epiphany Conference", Cracow, 7-9 January 2013 (available at [http://epiphany.ifj.edu.pl/current/pres/day2_03dipole.pdf])